
Triangle Singularities through the Unitary Three-Body Formalism

von

Ajay Shanmuga Sakthivasan

Masterarbeit in Physik

angefertigt im

Helmholtz-Institut für Strahlen- und Kernphysik

vorgelegt der

Mathematisch-Naturwissenschaftlichen Fakultät der
Rheinischen Friedrich-Wilhelms-Universität Bonn

März 2024

I hereby declare that the work presented here was formulated by myself and that no sources or tools other than those cited were used.

Bonn,
Ort, Datum
Unterschrift

1. Gutachter:

PD Dr Akaki Rusetsky
Helmholtz-Institut für Strahlen- und Kernphysik
Universität Bonn

2. Gutachter:

Dr Maxim Mai
Helmholtz-Institut für Strahlen- und Kernphysik
Universität Bonn

Abstract

Our current understanding of hadrons is through Quantum Chromodynamics (QCD). Being a non-Abelian gauge theory, QCD exhibits certain interesting properties. One of which is confinement, leading to a rich spectrum of hadrons. Experimentally, hadronic resonances can appear as peaks in the invariant mass distributions. However, universal parameters of hadronic resonances are theoretically encoded in the poles of the S -matrix. Still, not all observed peaks necessarily correspond to hadronic resonances. For example, kinematical singularities, which correspond to intermediate particles going on-shell, and producing a peak in the invariant mass distributions, without any correspondence to a pole in the S -matrix. This was originally identified by Landau, and has been recently suggested to explain the $a_1(1420)$, and many other such peaks in the observed invariant mass distributions.

In this work, we concern ourselves with re-examining the kinematical singularities in a model that innately respects three-body unitarity, specifically for the case of $a_1(1420)$. We first review the analytical aspects pertaining to kinematical singularities. Following that, utilising a recent approach to three-body unitarity, we study the kinematical singularities in the relevant coupled-channel system. We discuss the pattern and mechanism leading to the triangle singularity to all orders in exchange diagrams. It is shown that the triangle singularity persists, even after final-state interactions are taken into account. Further, it is shown that the contribution to the kinematical singularity arises mostly from the triangle (or the 1-loop) diagram. Thus, explaining the adequacy of non-unitary models discussed previously in the literature, which are also reviewed in this work. To this end, this work also discusses various numerical implementations that are relevant to solving the integrals that arise in this model.

Contents

Abstract	v
1 Introduction	1
1.1 The $a_1(1420)$ System	3
1.2 Unitarity, Analyticity & Dispersion Relations	4
1.3 Complex Analytic Methods	7
2 Analytic Study of Triangle Singularities	11
2.1 Review of Singularities of Integrals	11
2.2 Review of the Landau Equations	17
2.2.1 Types of Singularities	19
2.2.2 The Bubble Graph	21
2.2.3 The Triangle Graph	22
2.2.4 The Square Graph	26
2.3 Applications to the $a_1(1420)$ System	28
2.3.1 The 1-loop (Triangle) Level	28
2.3.2 The 1 + 1-loop (Triangle+1) Level	30
2.3.3 Singularities in Multi-loop Diagrams	32
3 Triangle Singularities in Non-Unitary Models	35
3.1 Kinematical Singularities in the Triangle Graph	36
3.2 Kinematical Singularities in the Triangle+1 Graph	42
4 Three-Body Unitary Formalism	47
4.1 The Infinite Volume Three-Body Unitary Formalism	48
4.1.1 The Isobar-Spectator Model & Unitarity	48
4.1.2 The Bethe-Salpeter Ansatz	50
4.1.3 Unitarity Matching and the Scattering Equation	52
4.1.4 Isobar Propagator Parametrisation	55
4.2 Implementation to the $a_1(1420)$ System	56
4.2.1 Coupled Channel Analysis	57
4.2.2 Isobar Propagator Parameters	57
4.2.3 Interaction Kernel Parameters	60
4.2.4 Numerical Implementation (Method0)	62
4.2.5 An Alternate Numerical Implementation (Method1)	74
5 Summary and Outlook	85
Acknowledgements	89

Bibliography	91
A Cutkosky Rules	97
B The Landau Equations: Dual Diagram Solutions	99
C Generalised Feynman Parametrisation	101
D Partial Wave Analysis	103
E Unitarity of the Isobar	106
F Gaussian Quadrature Integration Routine	108
G A Second Alternate Numerical Implementation (Method3)	110
H Additional Figures	112

List of Figures

1.1	The $a_1(1420)$ system	4
1.2	Dispersion relations	6
2.1	Integral with no singularities	12
2.2	Integral with a singularity: contour deformation	12
2.3	Integral with an endpoint singularity	14
2.4	Integral with a pinch singularity	15
2.5	The Landau equations: leading and subleading singularities	20
2.6	The Landau equations: bubble graph	21
2.7	The Landau equations: triangle graph	22
2.8	The Landau equations: singularity surface of the triangle graph	24
2.9	The Landau equations: square graph	26
2.10	The $a_1(1420)$ at the 1-loop (triangle) level	28
2.11	Triangle graphs with different intermediate particles	30
2.12	The $a_1(1420)$ at the 1 + 1-loop (Triangle+1) level	30
2.13	The $a_1(1420)$ at higher levels	32
3.1	The triangle graph in a non-unitary model	36
3.2	The triangle graph amplitudes	38
3.3	The triangle graph amplitudes: Feynman parametrisation	41
3.4	The triangle+1 graph in a non-unitary model	42
3.5	The triangle+1 graph amplitudes: Feynman parametrisation	44
4.1	The isobar-spectator model	49
4.2	The Bethe-Salpeter ansatz for the isobar-spectator amplitude	51
4.3	Unitarity of the isobar-spectator model & the Bethe-Salpeter ansatz .	52
4.4	The Bethe-Salpeter interaction kernel	54
4.5	Isobar propagator parametrisation	55
4.6	Isobar propagator parametrisation: two-body self-energy	56
4.7	$a_1(1420)$: three-body unitarity parameters	57
4.8	Channels considered in the analysis of $a_1(1420)$	58
4.9	Imaginary parts of the inverse isobar propagators	60
4.10	Phase shift plots for the K^* and f_0 propagators	61
4.11	B -term for the $a_1(1420)$ system with coupled channels	62
4.12	Singularities of the B -term for the spectator momentum contour .	65
4.13	Singularities of the isobar self-energy integral	66
4.14	The Bethe-Salpeter ansatz as an iterative solution	68
4.15	The Isobar-Spectator model at the triangle level	68
4.16	The Isobar-Spectator model at the finite house level (1)	70

LIST OF FIGURES

4.17	The Isobar-Spectator model at the full unitary level	72
4.18	The Isobar-Spectator model: effect of the propagator width	73
4.19	The Isobar-Spectator model: contributions from different levels	74
4.20	The Isobar-Spectator model: Argand plots	75
4.21	The Isobar-Spectator model: amplitudes outside the singular region .	75
4.22	Singularities of the B -term for real spectator momenta	79
4.23	Singularities of the B -term for complex spectator momenta	80
4.24	The Isobar-Spectator model: amplitudes (Method1) (1)	81
4.25	The Isobar-Spectator model: singularity contributions (Method1) . .	82
4.26	Comparison of Method0 & Method1	83
A.1	Cutkosky rules & the optical theorem	97
B.1	The triangle graph dual diagram	99
G.1	Singularities of the B term for the spectator momentum contour & singularities of the isobar self-energy integral (Method3)	111
G.2	The isobar-spectator model: amplitudes (Method3)	111
H.1	The triangle singularity in the $2 \rightarrow 2$ channel	112
H.2	The Isobar-Spectator model at the finite house level (2)	113
H.3	The Isobar-Spectator model: amplitudes (Method1) (2)	114

Chapter 1

Introduction

It might not entirely be a coincidence that many of the pioneers of the analytic S -matrix turned to seek higher powers. John Polkinghorne, for one, resigned from his professorship at the University of Cambridge to become an Anglican priest. Henry Strapp, on the other hand, ditched conventional physics to pursue his theory of quantum consciousness and free will. Look, I'm not saying that studying this subject is going to leave you searching for the purpose of life, but at least a certain amount of caution is advised.

S. Mizera, p.4, *Physics of the Analytic S-matrix* [1]

Great strides have been made in the last century to understand the smallest particles that comprise the observable matter. And the Standard Model is the pinnacle in this endeavour. The Standard Model successfully explains the constituent particles and their interactions at the smallest scale. The elementary components, or the particles, in this theory are categorised into fermions and bosons. Fermions are further categorised into quarks and leptons, which make up the matter. Bosons are categorised into the higgs and gauge bosons, which mediate the fundamental forces. These interactions, however, do not include gravity, which is still understood through the classical theory of general relativity. The interaction that is of the most relevance to this work is the strong interaction. *Quantum Chromodynamics* (QCD) is the theory of strong interactions, and is a non-Abelian gauge theory with the symmetry group $SU(3)$. Besides, QCD also exhibits certain interesting features: (1) asymptotic freedom, which means that the strength of the interaction decreases with increasing energy, in contrast to *Quantum Electrodynamics* (QED), which is the theory of electromagnetism with the symmetry group $U(1)$. This property of a quantum field theory allows standard perturbative calculations at high energies, similar to that of QED at currently practical high energies. However, the theory becomes non-perturbative at small energies, when the coupling gets stronger. The coupling grows fast enough with decreasing energy, that the theory exhibits another interesting property — confinement; (2) Confinement means that the quarks form hadrons at small energy scales. This leads to a rich spectrum of hadrons, that has proved hard to explain. Historically, the strong interaction proved to be harder than the electromagnetic interaction to understand.

Before the advent of QCD, a non-perturbative theory was put forward, called the S -matrix theory. The basic idea of this theory is that the transition amplitudes of interactions are ultimately the only quantities that are relevant. In a perturbative theory, one calculates the transition amplitudes as a power series expanded in terms

of the coupling constant. Formally, this is an asymptotic series. However, S -matrix theory argues that this perturbative approach can be sidestepped, and the transition amplitudes, which are the S -matrix elements, can be calculated directly by imposing the minimal conditions. These conditions are fundamental and must be adhered to, regardless of the existence of an underlying Lagrangian. For example, this includes the superposition principle and unitarity from quantum mechanics, Poincaré invariance, causality, etc. Further, in the S -matrix theory, the matrix elements are promoted to analytic functions of complex variables, and the values corresponding to physical observables are postulated to be the boundary values of these analytic functions. This is strongly related to causality, and earlier attempts at causality and analyticity similar to that of the theory of dispersion in optics gave rise to dispersion relations, in this context. However, such direct calculations of the S -matrix elements proved to be notoriously difficult. And with the experimental confirmations of the predictions of QCD, the S -matrix theory faded into the background. Still, this theory proved to be very powerful in the non-perturbative regime. Dispersion relations and unitary models based on the Bethe-Salpeter ansatz are built on these principles.

Experimentally, hadronic resonances present themselves as peaks in the measurable invariant mass distributions. And theoretically, these resonances correspond to poles of the S -matrix. But not all observed peaks correspond to a resonance. For example, there exists a class of singularities called *kinematical singularities*, which give rise to peaks in the invariant mass distributions, without a corresponding pole in the S -matrix. This was originally discovered by Landau. As we will see, these singularities arise when the intermediate particles in a scattering process go on the mass shell. And for particular cases, they give rise to singularities, that mimic a resonance in the experimental data. Recently, a lot of such peaks have been observed in experimental data, which are posited to be kinematical singularities. The system that we investigate in our work is the $a_1(1420)$, which can be explained as a kinematical singularity of the reaction, $a_1(1260) \rightarrow K^*(892)K^- \rightarrow f_0(980)\pi^-$, through a K^+ exchange. In this example, $K^*(892)$, K^+ and K^- going on-shell simultaneously, results in a logarithmic singularity in the incoming invariant mass of the system at around 1.4 GeV. This logarithmic singularity looks not very different from a resonance, which is typically parametrised through a Breit-Wigner curve, in the incoming invariant mass distribution. A perturbative expansion (in the context of an effective field theory) of the transition amplitudes as an asymptotic series is not meaningful when the underlying theory is non-perturbative. However, such a perturbative series can still be used to understand the analytic properties of the transition amplitudes. In this sense, the magnitudes of the individual terms are not meaningful themselves, but rather they reflect the analytic properties of the transition amplitudes. This is the rationale behind explaining such a peak observed in the $a_1(1260)$ decay as a kinematical singularity corresponding to the 1-loop diagram. However, one may still ask the question of how rescattering affects the observed peaks.

The main aim of the present work is to investigate the $a_1(1420)$ using a recent approach to three-body unitarity, which consistently resums the final-state interactions up to all orders, and as the name suggests, is inherently unitary. This is in contrast to the models considered in the literature before. The implementation of this approach to this particular system naturally requires a coupled-channel approach. And this is achieved through two different numerical implementations that

are consistent with each other. Additionally, we also investigate the analytical aspects of kinematical singularities, particularly in the context when one considers final-state rescattering. We mention here that we do not take the pseudovector nature of $a_1(1260)$ into account, and all the other particles that are considered are taken to be scalars. But this is not of relevance to the kinematical singularities, and the possible way to accommodate this, is also discussed. This work is organised as follows: in the remainder of this chapter, we briefly discuss a few tools that are used in this work. It should be noted, however, that our aim is not to be rigorous in this part, but only to introduce the relevant tools. In chapter 2, we review the analytic properties of the kinematical singularities. This amounts to a discussion of the Landau equations, which are then discussed in the context of the $a_1(1420)$ system. In chapter 3, we review the non-unitary approaches discussed in the literature. Chapter 4 contains the crucial parts of this work. We review the relevant three-body approach, and the ingredients that make it up. This is followed by a discussion of different numerical implementations and the corresponding results. In chapter 5, we summarise the work that was carried out, along with possible shortcomings and extensions.

1.1 The $a_1(1420)$ System

A resonance-like structure with quantum numbers $I^G(J^{PC}) = 1^-(1^{++})$ was reported by the COMPASS experiment [2], which was later confirmed by the VES experiment [3]. This narrow structure was observed in the $f_0(980)\pi^-$ P -wave of the $\pi^+\pi^-\pi^-$ final state. This structure was tentatively named $a_1(1420)$, with a mass of $M \approx 1.42$ GeV, and a width of $\Gamma \approx 0.14$ GeV. Curiously, this resonance-like structure had a mass not much larger than the associated ground state — $a_1(1260)$, and also had a narrower width. Further, the radial excited state of $a_1(1260)$ was expected to have a mass of $M \approx 1.65$ GeV [4]. This motivated alternate explanations for the structure, including a tetraquark [5] or a meson-meson bound state [6]. However, Mikhaseko et al. [4] showed that this structure could be something rather less exotic, but still mathematically interesting — a kinematical singularity. The proposed reaction was through a K^*K rescattering, as shown in the last diagram in figure 1.1. This was later extended to the realistic case of pseudovector $a_1(1260)$ by Aceti et al. [7]. And this was fit to COMPASS data [8], which showed a better fit than the resonance hypothesis.

By taking into account the respective quantum numbers, there are two reactions that we are interested in: $a_1(1260) \rightarrow K^*K^- \rightarrow f_0(980)\pi^-$, through a K^+ exchange, and $a_1(1260) \rightarrow K^{*-}K^0 \rightarrow f_0(980)\pi^-$, through a \bar{K}^0 exchange. Due to parity and angular momentum conservation, one can show that the K^* and K must be in a relative S -wave, and the $f_0(980)$ and π^- must be in a relative P -wave. In this work, we carry out our analyses with the first reaction. Kinematical singularities depend only on the relevant kinematic variables, and the small difference in the masses between K^\pm and K^0 do not invalidate the results obtained. Experimentally, the peak in question is observed in $p\pi^-$ scattering through a pomeron exchange. The relevant interaction in our analyses is the $\mathbb{P}\pi^-$ interaction. This interaction proceeds to the $f_0(980)\pi^-$ final state through an $a_1(1260)$. When the combined invariant mass of the $\mathbb{P} + \pi^-$ is about 1.4 GeV, there is a possibility of a kinematical singularity in the final state. Throughout this work, we use the term, “the $a_1(1420)$ system”

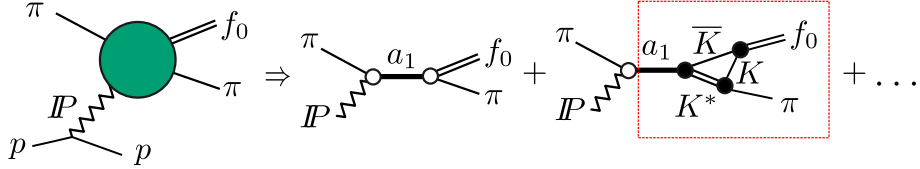


Figure 1.1: The $p\pi^-$ scattering with $f_0(980)\pi^-$ final state in P -wave. This proceeds through an $a_1(1420)$ in the $\mathbb{P}\pi^-$ interaction. \mathbb{P} here denotes a pomeron, f_0 denotes the $f_0(980)$, and a_1 denotes the $a_1(1260)$. The part of the diagram inside the red dashed box is called “the $a_1(1420)$ system” throughout this work. Figure partially attributed to Alexeev et al. [8].

to mean the part of the diagram inside the red dashed box in figure 1.1. The term “incoming invariant energy”, denoted by \sqrt{s} in this work, corresponds to the total invariant mass of $\mathbb{P} + \pi^-$. To avoid ambiguity, $a_1(1260)$ is denoted as a_1 in the rest of this work.

1.2 Unitarity, Analyticity & Dispersion Relations

In the next two sections, we briefly discuss the relevant mathematical tools that underlie this work. Apart from standard materials on this subject, one may also refer to Zwicky’s lectures [9], and Zhiboedov’s lectures [10], on the same. Suppose, we are working with an interaction that has a finite range, or equivalently, we consider an interaction that is “turned on” only during a finite interval in time. Then, in the asymptotic time limit $t \rightarrow \pm\infty$, the states are free. Any arbitrary state, then, can be written as a superposition of momentum eigenstates, labelled by the corresponding momentum eigenvalues. Suppose, we have a state $|m\rangle$. This state evolves according to $S^\dagger|m\rangle$. The matrix element $\langle m|S|n\rangle$ gives the overlap of the evolved state with some initial state $|n\rangle$. Here, all the states are the ones obtained in the limit $t \rightarrow -\infty$. The linear operator S , therefore, tells us the evolution of the states in the asymptotic time limit. For finite times, this reduces to the unitary evolution operator $U(t, t_0)$, as defined in the interaction picture. The most important thing here is that the conservation of probability implies that S must be unitary. That is,

$$S^\dagger S = S S^\dagger = \mathbb{1}. \quad (1.1)$$

Further, Poincaré invariance has the consequence that the S -matrix element can be written entirely in terms of Lorentz invariant quantities. For example, in the case of $2 \rightarrow 2$ scattering, one can make the choice of Mandelstam variables s , t and u as the Lorentz invariant quantities. Note that, only two of the three Mandelstam variables are independent. Still, the S -matrix cannot be analytic in the Lorentz invariant quantities, due to the presence of the 4-momentum conservation δ -function. The S -matrix also includes the trivial case when there is no interaction. Hence, it is customary to split the S -matrix into two parts,

$$S = \mathbb{1} + iT. \quad (1.2)$$

In this form, T includes all the interactions, while the first term is entirely interaction free. The T -matrix is related to the transition amplitude T_{fi} through

$$\langle q_1, \dots, q_n | T | p_1, \dots, p_m \rangle = (2\pi)^4 \delta^{(4)} \left(\sum_i q_i - \sum_j p_j \right) T_{fi}. \quad (1.3)$$

In the above expression, the δ -function has been factored out, and the transition amplitude T_{fi} is a function of Lorentz invariant quantities of the external momenta. T_{fi} can then be used to calculate physically relevant quantities, like the differential cross section of some reaction. Further, the transition amplitude is given by an asymptotic series of Feynman integrals whose analytic properties we are interested in. Taking a step back, we can see that the T -matrix is not unitary. In fact, the unitarity of the S -matrix implies that

$$T - T^\dagger = iT^\dagger T = iTT^\dagger. \quad (1.4)$$

One can sandwich the above equation between the initial and final states, and insert a complete set of states on the right-hand side of the equation, to get

$$T_{fi} - T_{if}^* = i \int \prod_j \left(\frac{d^4 k_j}{(2\pi)^4} (2\pi) \delta^{(+)}(k_j^2 - m_j^2) \right) (2\pi)^4 \delta^{(4)} \left(\sum_i p_i - \sum_j k_j \right) T_{fn} T_{in}^*. \quad (1.5)$$

Here, $\delta^{(+)}$ denotes the δ -function multiplied with a Heaviside- θ . That is, $\delta^{(+)}(k_j^2 - m_j^2) = \delta^{(4)}(k_j^2 - m_j^2)\theta(k^0)$, where the superscript 0 in the Heaviside- θ denotes the 0-th component of the 4-momentum. In the case $2 \rightarrow 2$ scattering, Poincaré invariance implies $T_{fi} = T_{if}$. This can be seen by noticing that for a system with ingoing 4-momenta p_1 and p_2 , and outgoing 4-momenta p_3 and p_4 , a rotation of π about the line bisecting p_1 and p_3 swaps them. But this also swaps p_2 and p_4 . This rotation, which ought to be a symmetry, has resulted in the initial and final states swapping with one another. For other scattering processes, one can use parity-time reversal (PT) invariance to show that $T_{fi} = T_{if}$. Now, we take a leap and assume that the transition amplitude is a well-defined complex analytic function of Lorentz invariant quantities. This relates to the condition for the S -matrix to satisfy that the physical results are boundary values of analytic functions, as mentioned before. We get

$$2i\Im(T_{fi}) = T_{fi} - T_{if}^* \equiv \text{disc}(T_{fi}), \quad (1.6)$$

where, “disc” stands for discontinuity. Equation (1.5) with the left-hand side given by equation by (1.6) is often called the *generalised optical theorem*, originally derived by Heisenberg. Using dispersion relations, one can obtain the full transition amplitude. Further, it can be shown that causality implies that the physical values are given by the limit on to the real axis from the upper half-plane in the respective complex variables. This can also be shown using perturbation theory for specific cases, when one is being pedantic. For example, for a transition amplitude that depends only on one Lorentz invariant quantity s , this implies

$$T(s_{\text{phys}}) = \lim_{\varepsilon \rightarrow 0^+} T(s + i\varepsilon). \quad (1.7)$$

This is equivalent to the $i\varepsilon$ -prescription of canonical quantum field theory, in which a $-i\varepsilon$ is added to the masses of the propagators, in order to obtain physical transition amplitudes.

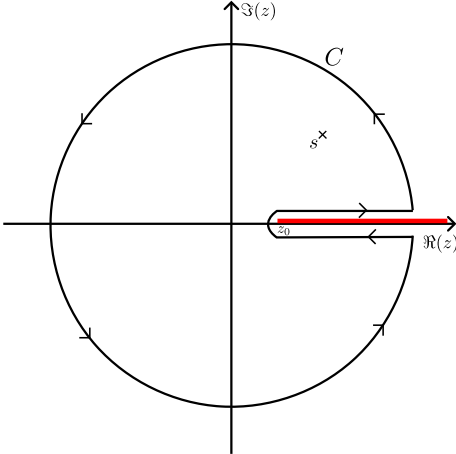


Figure 1.2: A complex function f , that is analytic throughout the complex plane, except for a branch cut along the real axis. The red line denotes the branch cut, starting at the branch point z_0 . C denotes the integration contour, and s denotes an arbitrary point on the complex plane.

As mentioned before, dispersion relations let one construct the transition amplitude using its discontinuity. These go by the name of Hilbert transforms in mathematics. Suppose, we have a complex function f that is analytic throughout the complex z -plane, except for a branch cut along the real axis. This situation is given in figure 1.2. Using Cauchy's integral theorem, one can obtain

$$f(s) = \frac{1}{2\pi i} \oint_C dz \frac{f(z)}{z - s}. \quad (1.8)$$

Here, C is the closed integration contour considered in figure 1.2. This integral can be split into the contributions from the circular part of the contour, and the contributions from the line segments above and below the branch cut. Assuming the contributions from the circular part of the contour vanishes in the limit the radius tends to ∞ , this integral can be written entirely in terms of the contributions from the line segments above and below the contour:

$$f(s) = \frac{1}{2\pi i} \lim_{\varepsilon \rightarrow 0^+} \int_{z_0}^{\infty} dz \frac{f(z + i\varepsilon) - f(z - i\varepsilon)}{z - s}. \quad (1.9)$$

Now, one may make use of Schwarz's reflection principle to write the above equation in terms of the discontinuity in the function f :

$$f(s) = \frac{1}{2\pi i} \int_{z_0}^{\infty} dz \frac{\text{disc}(f(z))}{z - s}. \quad (1.10)$$

This way, we can see that the value of an analytic function at an arbitrary point s is determined by its discontinuity across the branch cut. This is of great relevance to us. For example, consider the case of $2 \rightarrow 2$ scattering. The transition amplitude can be written as a function the Mandelstam variables s , t and u , as mentioned before. Only two of the three Mandelstam variables are independent, since they are related through the equation $s + t + u = \sum_{i=1}^4 m_i^2$, where m_i 's are the masses of the interacting particles. Therefore, one may consider the transition amplitude to be a

function of s and t , only. The principle of maximal analyticity tells that, there can be no non-analyticities on the complex plane, other than the ones arising from unitarity and poles corresponding to bound states. One can show that unitarity leads to a branch cut on the s -plane, for some fixed t corresponding to the physical s -channel process. The branch point corresponding to the branch cut is the respective 2-body threshold. This branch cut is called the *right-hand cut*. This can be taken to be the branch cut considered while discussing dispersion relations above. Further, crossing symmetry leads to another branch cut on the left-hand side, called the *left-hand cut*. One needs to also take bound states into account, while deriving the relevant dispersion relations. Additionally, for the case of poles, Kramers-Kronig relations are relevant. These go by the name of Sokhotski-Plemelj theorem in mathematics. For an integral evaluated along the real line, this reads:

$$\lim_{\varepsilon \rightarrow 0^+} \int_a^b dx \frac{f(x)}{x \pm i\varepsilon} = \mp i\pi f(0) + \mathcal{P} \int_a^b dx \frac{f(x)}{x}, \quad (1.11)$$

where \mathcal{P} denotes to Cauchy principal value of the integral.

1.3 Complex Analytic Methods

In the discussions so far and in the discussions that follow, we extensively make use of the complex nature of the quantities involved. For a rigorous treatment of this subject, one may refer to a standard textbook, like Ahlfors [11]. A complex-valued function of a complex variable is the generalisation of a real-valued function of a real variable. That is, it is a mapping

$$f : \mathbb{C} \supset D \rightarrow \mathbb{C}, \quad (1.12)$$

where D is the domain of the function. In the case of real functions, by definition, every element in the domain gets mapped uniquely to an element in the codomain. When every element in the range of the function has an unique inverse map in the domain, one may define an inverse of the function. There are cases, when one needs to carefully determine the domain and codomain of a function, in order to avoid multi-valuedness. For example, when considering the square root of an $x \in \mathbb{R}^+ \cup \{0\} \equiv D$, i.e., $f(x) = x^{1/2}$, one restricts the codomain to the positive reals, including 0. In the case of complex functions, this is done by introducing branch cuts. For example, when considering the square root of a $z \in \mathbb{C} \equiv D$, i.e., $f(z) = z^{1/2}$, using the polar form of z , one can show that

$$f(z) = \sqrt{r} e^{i\phi/2}. \quad (1.13)$$

Now, we evaluate the value at $\phi = 0$ two ways:

$$\begin{aligned} \lim_{\varepsilon \rightarrow 0^+} f(z + i\varepsilon) &= \sqrt{r}, \\ \lim_{\varepsilon \rightarrow 0^+} f(z - i\varepsilon) &= -\sqrt{r}. \end{aligned} \quad (1.14)$$

We can see that, the function evaluates to two different values, depending on how one approaches the real axis. In fact, one can show that any closed contour which includes 0, evaluates to non-zero values (more on Cauchy's integral theorem below).

The non-analytic points in the square root function, are exactly the root at 0 and the singularity at ∞ . These are the branch points of the function, and a branch cut is constructed by connecting these two branch points. In physics, the choice of the branch cut is usually the positive real axis, i.e., one takes the domain of the function to be $[0, 2\pi)$. This particular choice of the domain is called the principal branch of the function. The difference between the evaluations of the function across the defined branch cut, is the discontinuity in the function. But one may also consider a different viewpoint, as originally studied by Riemann. Suppose, we start at $z + i\varepsilon$, we showed that going around 0 once, results in a different evaluation for $f(z - i\varepsilon)$. However, if we go around once again, one can show that we arrive at the original value. Therefore, one may equivalently take the domain of the function to be $[2\pi, 4\pi)$. In this context, one calls the image of the function obtained using the original domain the *principal sheet*, and the latter the *non-principal sheet*. Gluing these sheets together, one obtains a *Riemann surface*, which is a complex manifold. The relevance of this discussion to us is that, as a consequence of the principle of maximal analyticity which was discussed before, resonances, which appear as poles of the corresponding S -matrix element, are present on the non-principal sheets.

Complex functions are more restrictive, in the sense that, the existence of complex derivative of a function is a stronger requirement. Cauchy-Riemann equations give the necessary and sufficient conditions for a complex function to be complex differentiable. Further, a function being holomorphic, i.e., complex differentiable in a given neighbourhood, implies and is implied by the analyticity of the complex function, i.e., the existence of a convergent power series for the points in the neighbourhood. A function that is analytic for all points in the complex plane, is called *entire*. One result that is extensively used, is the Cauchy's integral theorem. Given a function f that is holomorphic in a simply connected domain Ω , for any closed contour $C \in \Omega$,

$$\int_C f(z) dz = 0. \quad (1.15)$$

A consequence of this theorem is that complex integrals can be evaluated in a similar fashion to that of integrals of real functions — as the difference of some complex anti-derivative, evaluated at the endpoints of the contour. Other more significant consequences are the Residue theorem and the related Cauchy's integral formula. Given a function f that is holomorphic in a simply connected domain Ω , for any closed contour $C \in \Omega$, which is oriented anti-clockwise and contains the point z_0 ,

$$f(z_0) = \frac{1}{2\pi i} \int_C dz \frac{f(z)}{z - z_0}. \quad (1.16)$$

That is, the value of the function at some point z_0 , is determined by the values on some closed contour that includes it. Usually, it is the case that some function is defined in some particular domain. For example, this could be just the real axis. The method by which one extends the natural domain, or promotes the function to a complex function in the case of a real function, is called *analytic continuation*. Very crudely, consider a power series that is convergent in some natural domain D_1 , defined about some z_0 :

$$f_1(z) = \sum_{k=0}^{\infty} a_k (z - z_0)^k. \quad (1.17)$$

By definition, f_1 is analytic. One may extend this to a domain D_2 , which has a non-zero intersection with D_1 , i.e., $D_2 \cap D_1 \neq \emptyset$. And suppose, we have an analytic function f_2 , defined on D_2 , such that $f_1 = f_2$ for all z in the intersection $D_1 \cap D_2$, then f_2 is called the analytic continuation of the function in the new domain. The analytic continuation of a function is unique. This way, one can extend the natural domain of a function to the entire complex plane. The monodromy theorem gives the sufficient conditions for the existence of analytic continuation of a function. Gap theorems impose constraints on the nature of the power series to have an analytic continuation. Complex analytic nature of the quantities involved in our work, has substantial consequences to the way one approaches this subject.

Chapter 2

Analytic Study of Triangle Singularities

The difficulty lies in imagining what happens in the four (or more)-dimensional space of the integration variables. We shall be content with plausibility arguments.

R.J. Eden et al., p.48, *The Analytic S-Matrix* [12]

We begin with an analytic study of triangle singularities, or more generally, kinematical singularities. Given a quantum field theory, the standard approach to calculate meaningful observables, like transition amplitudes, is through a perturbative expansion, with the series not necessarily expected to converge. Every term of such an expansion, corresponds to an integral that should be solved. Any standard textbook on quantum field theory, like Peskin & Schroeder [13] and Das [14], discusses this elaborately. However, explicit evaluation of such integrals to study the analytic structure is exceedingly difficult at higher orders. For example, 't Hooft & Veltman [15] showed that an n -point correlation functions can be expressed in terms of Spence functions¹, whose analytic structure is known. A 4-point correlation function of one-loop scalar propagators requires a combination of 36 or 108 Spence functions depending on the parameters. Since we are more interested in the analytic structure rather than the exact solutions of the integral, we discuss a method of studying the singularities arising in integrals, originally introduced by Eden [16] as a generalisation of Hadamard's results in complex analysis [17]. This chapter is structured as follows: in the first two sections, we review singularities arising in integrals and the Landau equations, extensively. The first two sections closely follow chapter 2 of Eden et al. [12]. In the last section, we present the results relevant to our study.

2.1 Review of Singularities of Integrals

Consider the following complex valued integral:

$$f(z) = \int_C dw g(z, w). \quad (2.1)$$

¹Also known as the dilogarithm, $\text{Sp}(x) = -\int_0^1 dt \frac{\ln(1-xt)}{t}$.

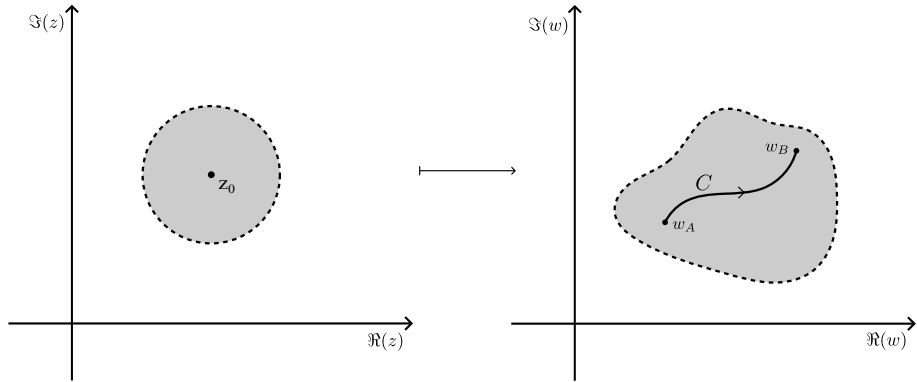


Figure 2.1: An example when, for a given neighbourhood about z_0 , there exists a neighbourhood on the integration plane free of all the singularities. And the integration contour is fully contained in this neighbourhood.

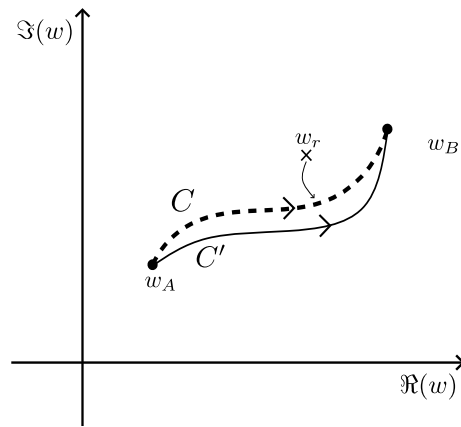


Figure 2.2: An example when a singularity can be avoided by contour deformation. Here, C' is the deformed contour that does not have any singularity hitting it.

Here, the function $g(z, w)$ is a complex-valued function of complex variables and the integral is performed over some contour C defined on the w -plane. In general, the analyticity of the complex valued function f is not apparent, and it depends on the analyticity of g . Given g is an entire function, then f is necessarily entire on the finite complex plane. This can be shown by using Morera's theorem and Cauchy's integral theorem, see Ahlfors [11]. Even if g is not entire, some things can still be said about the analyticity of f . Suppose g is analytic except for a finite number of singularities at w_r , $r = (1, 2, \dots, n)$. These singularities can, but not necessarily, be parametrised in the variable z to give their locations on the w -plane, i.e., $w_r \equiv w_r(z)$. Now for a given neighbourhood of z about z_0 , suppose there exists a neighbourhood on the w -plane that is free of the singularities w_r . If the contour is contained in this w -neighbourhood, then the integral is well-defined for all z in the z_0 -neighbourhood. This might not be the case for a different neighbourhood in z , when any of the singularities necessarily hit the contour for some z . This is still not a problem, since one could use Cauchy's integral theorem and deform the contour before the singularity hits the contour. In other words, Cauchy's theorem says that

$$f(z) = \int_C dw g(z, w) = \int_{C'} dw g(z, w), \quad (2.2)$$

where C' is the deformed contour. The above equation can be seen as an analytic continuation of equation (2.1), which is well-defined before the singularity hits the contour. Alternatively, this can be seen as continuously deforming the integration contour to a new contour, which has a neighbourhood free of the singularities for the corresponding z -neighbourhood. So, in the case of singularities hitting the contour of integration, the procedure is to continuously deform the original contour in the $w \in \mathbb{C} \setminus \{w_r\}$ plane, and evaluate the integral along the deformed contour.

This neat procedure fails when a singularity hitting the contour is inevitable, even through contour deformation. This arises in the following cases:

- (i) *End-point singularities*: In the case when any of the singularities w_r hit either endpoints of the integration contour, a contour deformation is no longer possible. This leads to a singularity in the evaluated integral at z , which satisfies $w_r(z) = w_A$ and $w_r(z) = w_B$, where w_A and w_B are the endpoints of the contour. For example, the following integral:

$$f(z) = \int_1^2 dw \frac{1}{w-z} = \log \left(\frac{2-z}{1-z} \right), \quad (2.3)$$

has endpoint singularities at $z = 1$ and $z = 2$. Note that the singularities of the integrand can be parametrised as $w_1(z) = z$, in this case. And the endpoint singularities satisfy $w_1(z) = z = 1$ and $w_1(z) = z = 2$, respectively (see figure 2.3). One does not need the knowledge of the closed form solution of the integral.

- (ii) *Pinch singularities*: Another case when a contour deformation is not possible is when two or more of the singularities approach the integration contour from the opposite sides and *pinch* the contour. Or, a singularity might approach a fixed singularity from the opposite side of the contour and *pinch* it. These lead to a singularity in the evaluated integral at z which pinches the contour. These obey $w_i(z) = w_j(z)$, for some i, j singularity labels. Although pinch singularity is necessary for this condition, it is not sufficient.

Two singularities approaching the contour from the same side do not pinch the contour. For example, the following integral:

$$f(z) = \int_1^2 dw \frac{1}{(w-z)(w-5/2)} = \frac{1}{z-5/2} \log \left(\frac{3(2-z)}{1-z} \right), \quad (2.4)$$

has endpoint singularities at $z = 1$ and $z = 2$. Note that the singularities of the integrand can be parametrised as $w_1(z) = z$ and $w_2(z) = 5/2$. The endpoint singularites, then, can be seen as arising from w_1 . The singularity w_2 does not depend on z . And since it is different from the endpoints of the contour, it does not give rise to endpoint singularities. However, now there is a possibility of a pinch with w_1 . The pinch singularity at $w_1 = z = 5/2$ is not obvious, though. This singularity is not present on the principal sheet of the function, since the logarithmic zero cancels out the zero from the denominator. This singularity is present on the non-principal sheets. Notice however, had the fixed singularity of the integrand lain between the endpoints of the contour, the pinch singularity would have occurred on the principal sheet too (see figure 2.4). Again, one does not need the knowldege of the closed form solution of the integral.

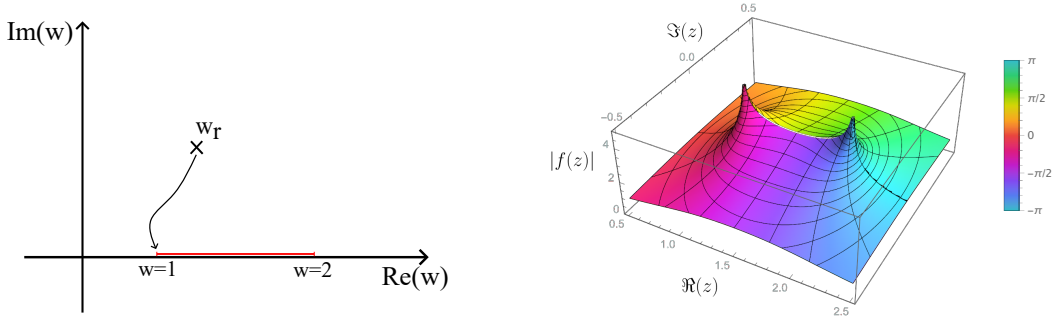


Figure 2.3: Endpoint singularity arising when the integration contour cannot be deformed due to the singularity hitting the endpoint. The red line denotes the integration contour (see equation (2.3)).

- (iii) *Infinite Deformations:* Finally, a singularity hitting the contour cannot be avoided through this procedure, when the contour deformation requires a deformation to infinity. In this case, the integral cannot be evaluated, leading to a singularity at z , which satisfies $w_r(z) \rightarrow \infty$. Alternatively, this can be seen as a pinch of the contour by complex infinity and the singularity from the integrand, if the integral is redefined for the extended complex plane. For example, the following integral:

$$f(z) = \int_1^2 dw \frac{1}{zw+1} = \frac{1}{z} \log \left(\frac{2z+1}{z+1} \right), \quad (2.5)$$

has endpoint singularities at $z = -1$ and $z = -1/2$. Again, the infinite deformation singularity is present on the non-principal sheets at $z = 0$.

We should also note that the singularities arising this way are typically branch points, because the integral involves integrating a function with simple poles, resulting in a logarithm or a square root. Only these kinds of kinematical singularities are relevant for our study, as we will discuss later. Since we have branch points, our integrals will also have a branch cut, which can also be seen in figures 2.3 & 2.4 already. Analysing these branch cuts will be an interesting part of our discussion later.

Now we can generalise the above discussion to: (1) Integrals that are functions of more than one variable; (2) Integrals involving more than one integration variable. (1) When generalising to integrals that are functions of more than one variable, say for example,

$$f(z_1, z_2) = \int_C dw g(z_1, z_2, w). \quad (2.6)$$

The endpoint singularities obey $w_r(z_1, z_2) = w_A$ and $w_r(z_1, z_2) = w_B$, where w_A and w_B are the endpoints of the contour. The pinch singularity obeys $w_i(z_1, z_2) = w_j(z_1, z_2)$, for some i, j singularity labels. These equations have two degrees of freedom. Therefore, they denote a two-dimensional surface in the four-dimensional z_1, z_2 complex space. Similarly, an integral with n complex variables give rise to a $(2n-2)$ -dimensional hypersurface in the $2n$ -dimensional complex space. It should be noted again that pinch singularities are necessary for this condition, but not sufficient. To elaborate on, not all the points on the hypersurface Σ_P that satisfies the

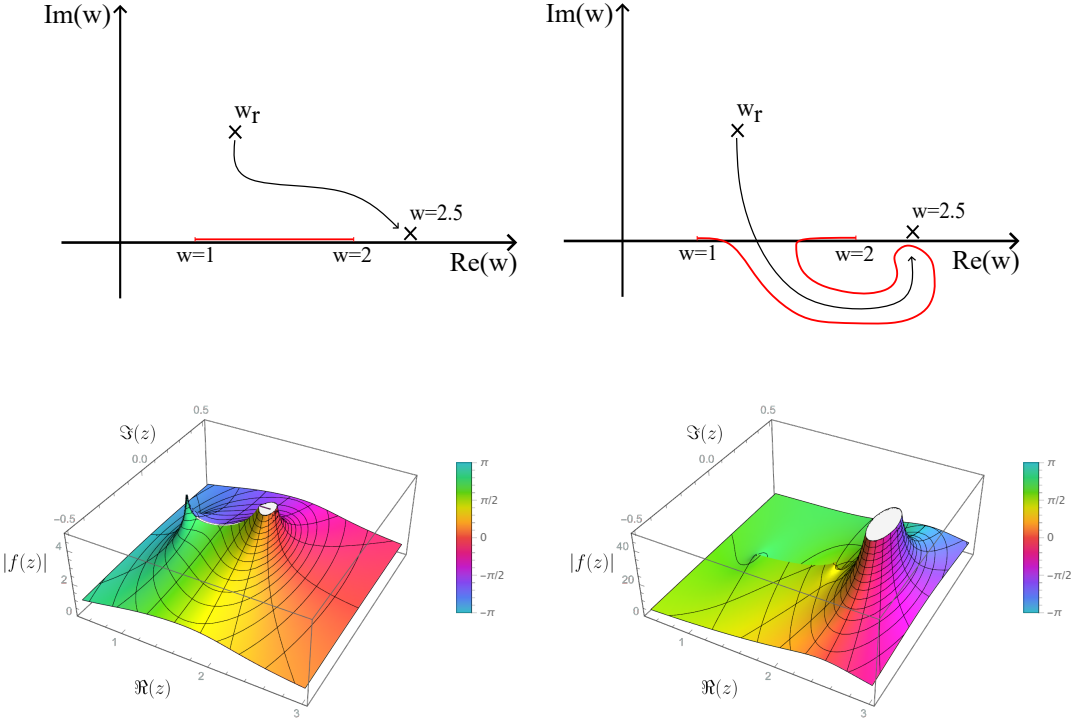


Figure 2.4: Pinch singularity arising when the integration contour gets pinched between two singularities on the opposite sides of the contour. The red line denotes the integration contour. In the first case, evaluating the integral on the principal sheet poses no problem, since the singularity approaches the fixed singularity from the same side of the contour. But in the second case, evaluating the integral on a non-principal sheet forces a contour deformation, which ultimately gets pinched (see equation (2.4)).

pinch singularity condition results in a pinch singularity. Such points may lie far from the contour, posing no problems in evaluating the integral, similar to equation (2.4) and figure 2.4. To make this more formal, we may say that the intersection of this hypersurface Σ_P with the hypersurface corresponding to the endpoint singularities Σ_E , divide Σ_P into singular and non-singular regions. Since this encodes whether overlapping singularities are far from the integration contour, or actually on top of the contour, which causes a pinch as discussed previously. This still has the drawback of which path is chosen for analytic continuation. This, again, was seen in the previous discussion where the principal sheet had no pinch singularity, but the non-principal sheet did. We should conclude that the existence of pinch singularities depend on the choice of analytic continuation, and in effect, the choice of branch cut in our case, since our singularities are branch points. Also, pinch singularities need not occur if the overlapping singularities approach the contour from the same side.

Finally, we would like to foreshadow the Landau equations. Suppose the singularities of the function inside the integral w_r , are the roots of some algebraic equation

$$S(w; z_1, z_2) = 0. \quad (2.7)$$

This can be seen as the surface describing the singularities of the integrand. This,

taken together with the equation

$$\frac{\partial S}{\partial w} = 0, \quad (2.8)$$

gives the condition for overlapping zeros. This can be seen as an implication of Rolle's theorem — for overlapping zeros, the first derivative with respect to w vanishes. In the case of integrals involving multiple integration variables, there is a nicer geometric interpretation involving normality of the singularity surfaces. Further, for n overlapping zeros, we simply impose the condition that the n th partial derivative of the algebraic equation S vanishes. Whether these overlapping zeros actually result in a pinch singularity has to be determined by adding a small imaginary part, say $i\varepsilon$, to the variables, and noticing how the singularities approach the contour.

(2) When generalising to integrals involving multiple integration variables, say for example,

$$f(z) = \int_H \prod_{i=1}^n dw_i g(z, w_i). \quad (2.9)$$

Instead of a contour ' C ' on the two-dimensional complex plane, we now have a hypercontour ' H ' in the $2n$ -dimensional complex space. Now, the singularities are seen as the zeros of the equation

$$S_r(z, w_i) = 0, \quad (r = 1, 2, \dots, R). \quad (2.10)$$

The generalised kinematical singularities arise when these zeros approach the hypercontour. However, it is still not a problem as long as the hypercontour can be continuously deformed to avoid the approaching singularity. We now motivate the conditions for kinematical singularities to occur. Similar to the previous case of integral with multiple variables, the hypercontour may get pinched by two singularity surfaces, S_p, S_q , from the opposite sides, which is given by

$$S_p = S_q = 0, \quad (2.11)$$

$$\alpha_p \frac{\partial S_p}{\partial w_i} + \alpha_q \frac{\partial S_q}{\partial w_i} = 0, \quad (i = 1, 2, \dots, n), \quad (2.12)$$

where, $p, q = (1, 2, \dots, R)$, and α_p, α_q are some real parameters. The first and second equations are the generalisations of equations (2.7) & (2.8), respectively. The second equation now has a geometric interpretation. This is just the condition for the normals of the hypersurface to coincide. Again, in the case of more than two singularities approaching the hypercontour, we need to include further singularity surfaces to this equation. We should also note that the hypercontour may be pinched by the same surface on the opposite sides of the contour. The condition, which is the case when $p = q$ in the previous equations, is given by

$$S_p = 0, \quad (2.13)$$

$$\frac{\partial S_p}{\partial w_i} = 0, \quad (i = 1, 2, \dots, n), \quad (2.14)$$

where, $p = (1, 2, \dots, R)$. We have not included endpoint singularities so far. The restriction on the singularity surface is now, to not hit the boundary surface of the hypercontour. Suppose the boundary obeys the following conditions:

$$\tilde{S}_{\tilde{r}}(z, w_i) = 0. \quad (2.15)$$

We can extend the above discussion for the surfaces S_r , and treat the surfaces \tilde{S}_r on an equal footing and derive similar conditions. We end this section by foreshadowing Landau equations again. We can reduce the kinematical singularity conditions to

$$\alpha_i S_i = 0, \quad (i = 1, 2, \dots, R), \quad (2.16)$$

$$\tilde{\alpha}_j \tilde{S}_j = 0, \quad (j = 1, 2, \dots, R), \quad (2.17)$$

$$\frac{\partial}{\partial w_p} \left(\sum_i \alpha_i S_i + \sum_j \tilde{\alpha}_j \tilde{S}_j \right) = 0, \quad (i, j = 1, 2, \dots, R). \quad (2.18)$$

Finally, we reiterate that kinematical singularities are necessary for these equations, however not sufficient. Analysing the sufficient conditions requires some knowledge of the integral. A more rigorous derivation of the above equations require a proper topological treatment, which can be found in Fotiadi et al. [18].

2.2 Review of the Landau Equations

Following the discussion from the previous section, we now study the singularities of integrals in the context of Feynman integrals. Directly applying the equations (2.16), (2.17) and (2.18) should give us, in principle, the locations of the singularities in terms of the complex external momenta. This was first studied by Landau [19], and hence, named after him. It was also studied by Nakanishi [20], and was derived and used by Bjorken [21] in his doctoral dissertation independently. Landau originally studied the singularities in the Feynman integrals in two different forms. Later, Polkinghorne and Scretton extended this to a third form of the Feynman integral [22, 23]. It can be shown that all three forms of the Landau equations are equivalent [12].

Starting with a Feynman integral corresponding to N internal scalar propagators and l loop momenta:

$$I_1 = \int \prod_{i=1}^l d^4 k_i \frac{1}{\prod_{r=1}^N (q_r(k_i)^2 - m_r^2)}, \quad (2.19)$$

we can parametrise the integral using Feynman parametrisation, which results in

$$I_2 = \Gamma(N) \int \prod_{i=1}^l d^4 k_i \int_0^1 \prod_{j=1}^N d\alpha_j \frac{\delta(\sum_{r=1}^N \alpha_r - 1)}{\left(\sum_{r=1}^N \alpha_r (q_r(k_i)^2 - m_r^2) \right)^N}, \quad (2.20)$$

and further, we can integrate over the loop momenta to obtain

$$I_3 = \Gamma(N) \int_0^1 \prod_{j=1}^N d\alpha_j \frac{\delta(\sum_{r=1}^N \alpha_r - 1) C^{N-2(l+1)}}{\left(\sum_{r=1}^N f_r(\alpha) z_r - C(\alpha) \sum_{i=1}^N \alpha_i m_i^2 \right)^{N-2l}}, \quad (2.21)$$

where C is a combination of products of α 's, $f_r(\alpha)$ and $C(\alpha)$ are functions of α 's, and z_r 's are different scalar invariants of the external momenta. The exact forms are not relevant to us, but can be found in Eden et al. [12]. Also, notice that we have not integrated out the δ -function to preserve the homogeneity of the equation. The three representations of the Landau equations are then obtained by applying the equations from the previous section, equations (2.16), (2.17), (2.18), to the above Feynman integral representations:

- (i) For the first representation due to Landau, consider equation (2.19). These are infinite integrals, and therefore, have no boundary surfaces \tilde{S}_r . The singularity surfaces S_i are just $(q_i^2 - m_i^2)$, with $i = \{1, \dots, N\}$. Using equations (2.16) and (2.18), we therefore get

$$\alpha_i S_i \equiv \alpha_i (q_i^2 - m_i^2) = 0 \implies \alpha_i = 0 \text{ or } q_i^2 = m_i^2, \quad (2.22)$$

$$\frac{\partial}{\partial k_j^\mu} \sum_i (\alpha_i S_i) = \frac{\partial}{\partial k_j^\mu} \sum_i (\alpha_i (q_i^2 - m_i^2)) = \sum_i \alpha_i q_i^\mu(k_j) = 0, \quad (2.23)$$

where $i = (1, 2, \dots, N)$ and $j = (1, 2, \dots, l)$. Note that the sum is carried out over q_i 's that depend on k_j , and we get one equation for each loop momentum, corresponding to the latter equation. Also, the direction of the momenta of the propagator are chosen in such a way that the derivative is always positive. If this is not ensured, there will be an additional negative sign from some of the derivatives. This is noted again later.

- (ii) For the second representation, again due to Landau, consider equation (2.20). The integrals over the loop momenta are infinite integrals, and therefore, they have no boundary surfaces. But the integrals over α 's have endpoint constraints at $\alpha = 0$ and $\alpha = 1$. The endpoint constraint at $\alpha = 1$ is actually not a constraint, due to the δ -function. To see that, notice that after the δ -function is integrated out, the new boundary constraints will be $\alpha_1 = 0, \alpha_2 = 0, \dots, \alpha_{N-1} = 0$ and $\alpha_1 + \dots + \alpha_{N-1} = 1$. The final constraint is just $\alpha_N = 0$ before the δ -function is integrated out. Therefore, the endpoint surfaces \tilde{S}_i are just the N Feynman parameters α_i . If we introduce a real parameter α' , then equation (2.16) leads to

$$\alpha' S \equiv \alpha' \left(\sum_{i=1}^N \alpha_i (q_i^2 - m_i^2) \right) = 0. \quad (2.24)$$

Similarly, introducing real parameters $\tilde{\alpha}_i$'s, equation (2.17) leads to

$$\tilde{\alpha}_i' \tilde{S}_i \equiv \tilde{\alpha}_i' \alpha_i = 0, \quad (i = 1, \dots, N). \quad (2.25)$$

And finally, equation (2.18) leads to

$$\frac{\partial}{\partial k_j} \left(\alpha' S + \sum_{i=1}^N \tilde{\alpha}_i' \tilde{S}_i \right) = \alpha' \frac{\partial S}{\partial k_j} = 0, \quad (j = 1, \dots, l) \quad (2.26)$$

$$\frac{\partial}{\partial \alpha_j} \left(\alpha' S + \sum_{i=1}^N \tilde{\alpha}_i' \tilde{S}_i \right) = \alpha' \frac{\partial S}{\partial \alpha_j} + \tilde{\alpha}_j' = 0, \quad (j = 1, \dots, N). \quad (2.27)$$

If we exclude the trivial solution $\alpha' = 0$, then we see that these are exactly the first representation of the Landau equations.

- (iii) For the third representation due to Polkinghorne and Screamton, consider equation (2.21). We now have integrals over the α_i 's and no infinite loop momentum

integrals. The equations (2.16), (2.17) and (2.18) then lead to

$$\alpha' D = \alpha' \left(\sum_{r=1}^N f_r(\alpha) z_r - C(\alpha) \sum_{i=1}^N \alpha_i m_i^2 \right)^{N-2l} = 0 \quad (2.28)$$

$$\tilde{\alpha}_i' \alpha_i = 0 \quad (i = 1, \dots, N) \quad (2.29)$$

$$\alpha' \frac{\partial D}{\partial \alpha_j} + \tilde{\alpha}_j' = 0 \quad (j = 1, \dots, N). \quad (2.30)$$

Using the explicit forms of $C(\alpha)$ and $f_r(\alpha)$, it can be shown that these set of equations are the same as the first representation, for $C \neq 0$. The special case at $C = 0$ needs to be investigated independently, which we briefly discuss in the next subsection. The first and second representations due to Landau are enough to determine the location of the kinematical singularities, and whether they lie on the physical sheet, for most cases.

2.2.1 Types of Singularities

The first representation of the Landau equations essentially tells us that for the kinematical singularities, either the internal propagators go on-shell, or they don't contribute to the Feynman integral at all. The singularity corresponding to none of the Feynman parameters vanishing is called the *leading Landau singularity*. This is the case when all the internal propagators go on-shell. The singularity corresponding to at least one of the Feynman parameters vanishing is called the *subleading Landau singularity* or the lower-order singularity. Setting one or more Feynman parameters to 0 is equivalent to contracting the propagators corresponding to the vanishing parameters, and we call this a “contraction”. We propose two lemmas here, which are used in our results. We skip rigorous proofs of the lemmas, but motivate them.

Lemma 2.2.1. *Subleading singularities of a given graph are the leading singularities of a different graph with less internal propagators.*

Proof. Suppose we start with a graph with N internal propagators. Setting one of the Feynman parameters to 0 results in no contribution from the corresponding internal propagator towards the Feynman integral. This resulting Feynman integral is same as the one corresponding to $N - 1$ internal propagators. Analysing the Landau singularities for this new integral, we can see that the leading singularity equations are the same as the subleading singularity equations for the original integral. \square

Lemma 2.2.2. *For a graph with N internal propagators, setting $N - 1$ Feynman parameters to 0 results in a graph with trivial analyticity properties for massive internal propagators.*

Proof. Suppose we set all the Feynman parameters except α_1 to 0, then the first representation of the Landau equations reduce to, $\alpha_1(q_1^2 - m_1^2) = 0$ and $\alpha_1 q_1^\mu = 0$. The only valid solution to these equations is $\alpha_1 = 0$, which is the same as setting all the Feynman parameters to 0, i.e., no internal propagators at all. \square

We mentioned earlier that the kinematical singularities are typically branch points. This was showed by Polkinghorne and Screamton [22, 23], using the third representation of Landau equations. Suppose we have a graph with N internal

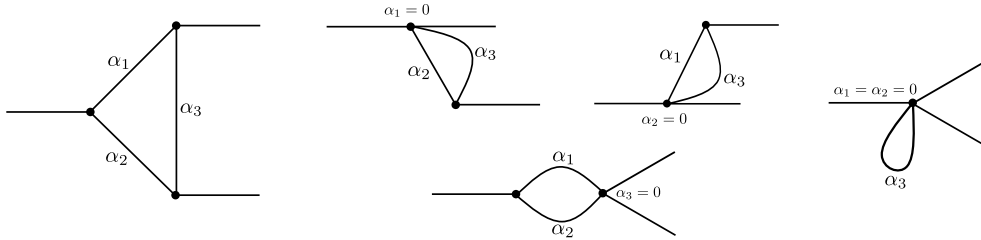


Figure 2.5: Landau singularities in the triangle graph — the leading Landau singularity corresponds to the case where all the internal propagators go on-shell; the subleading Landau singularities correspond to at least one of the internal propagators not contributing to the Feynman integral. Here, we have used the Feynman parameters to label the internal propagators. Also note that the final graph has trivial analyticity properties (see lemma 2.2.2).

propagators, l loop momenta and $\nu = (0, 1, \dots, N - 2)$ contractions. We define, $\gamma = \frac{1}{2}(N - \nu + 1) - 2l$. Then the types of singularities associated with the Landau equations can be understood by expanding the Landau equations in a power series and carrying out the integral. The results are summarised in the table 2.1. For most of the graphs, γ is typically negative, which corresponds to the Landau singularities being either square root or logarithmic branch points. Interestingly, the nature of the leading singularity in a diagram with 5 internal propagators and 1 loop momentum — the pentagon graph, which is not discussed further — is a pole. This can also mimic a resonance in the invariant mass distributions.

Condition	Singularity
$\gamma \in \{1, 2, \dots\}$	Poles
$\gamma \in \{\dots, -3/2, -1/2, 1/2, 3/2, \dots\}$	Algebraic branch point
$\gamma \in \{\dots, -2, -1, 0\} \& (N - \nu) \text{ even}$	Square root branch point
$\gamma \in \{\dots, -2, -1, 0\} \& (N - \nu) \text{ odd}$	Logarithmic branch point

Table 2.1: Types of singularities associated with the Landau equations. Note again that $\gamma = \frac{1}{2}(N - \nu + 1) - 2l$, where N is the number of internal propagators, ν is the number of contractions, including no contractions, and l is the number of loop momenta.

Another thing we would like to briefly mention is the existence of a different class of kinematical singularities, originally identified by Cutkosky [24], who called these non-Landauian singularities. They are also called the second-type singularities in the literature. They correspond to the case when the external momenta are light-like. The existence of these singularities are not apparent in the first representation of the Landau equations. However, these singularities exactly correspond to the $C = 0$ case in the third representation, which was briefly mentioned in the last section. Fairlie et al. [25, 26] extensively studied and generalised these second-type singularities.

Finally, we end this subsection by noticing an interesting correlation originally observed by Mathews [27] and Wu [28]. We can think of the Feynman graphs as electric circuits, with the propagators regarded as wires. Each wire has a current q_i and resistance α_i . Then the Landau equations are identical to Kirchoff's law

with a total potential 0, such that the currents take the value m_i . The subleading singularities correspond to shorting one or more of the wires, while the rest of the currents take the value m_i .

2.2.2 The Bubble Graph

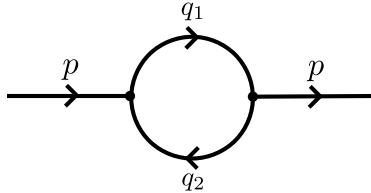


Figure 2.6: The bubble graph.

We now apply the Landau equations to an actual Feynman graph. First, let us consider the implications on the *bubble graph*. This is a one-loop graph of two propagators with $q_1 = k$ and $q_2 = k - p$, where k is the loop momentum. From our previous discussions, we should notice that $\gamma = -1/2$ and hence, we expect a (square root) branch point at the location of the singularity. Using the first representation of the Landau equations, we get

$$q_1^2 = m_1^2 \quad \& \quad q_2^2 = m_2^2, \tag{2.31}$$

$$\alpha_1 q_1^\mu + \alpha_2 q_2^\mu = 0. \tag{2.32}$$

There are no subleading singularities in this case, since a single contraction leads to a graph with trivial analyticity properties. We are interested in the solutions in terms of the invariant masses, than the explicit 4-momenta. Since, one can always make use of Lorentz symmetry to construct the 4-momenta explicitly in this case. Therefore, to solve this system of equations, we first note that we can construct 3 independent scalar invariants of the internal propagator momenta, $q_1 \cdot q_1$, $q_1 \cdot q_2$ and $q_2 \cdot q_2$. The on-shell condition for q_1 and q_2 reduces these degrees of freedom to 1. And finally, the vertex 4-momentum conservation relation removes this internal degree of freedom. Therefore, we should be able to write down the solutions to the Landau equations entirely in terms of p^2 , m_1 and m_2 . Now, we can take a dot product of equation (2.32) with q_1^μ and q_2^μ , and when taken together with equation (2.31) this leads to solving

$$\begin{pmatrix} m_1^2 & q_1 \cdot q_2 \\ q_2 \cdot q_1 & m_2^2 \end{pmatrix} \begin{pmatrix} \alpha_1 \\ \alpha_2 \end{pmatrix} \equiv Q\boldsymbol{\alpha} = \mathbf{0}. \tag{2.33}$$

Here, q_1^2 and q_2^2 have already been replaced with m_1^2 and m_2^2 from equation (2.31). Taking also the conservation of 4-momentum into account, we get $q_1 \cdot q_2 = 1/2(m_1^2 + m_2^2 - p^2)$. The non-trivial solutions to this determinant equation are given by $\det Q = 0$. From which we get the locations of the singularity in terms of the external momentum p : $p_1 = m_1 + m_2$ and $p_2 = |m_1 - m_2|$. The first singularity corresponds exactly to the one obtained through unitarity considerations — it is the normal threshold. However, the second solution cannot be obtained directly through

unitarity considerations — it is the anomalous or pseudo-threshold. The first representation of the Landau equations does not tell us about which Riemann sheet the singularities are located on. To find that, we need to use either the second or the third representation. We find out the value of $\alpha = (\alpha_1, (1 - \alpha))^\top$ corresponding to $q_1 \cdot q_2 = \pm m_1 m_2$, which gives $\alpha_1 = m_2 / (m_1 + m_2)$ and $\alpha_2 = m_2 / (m_2 - m_1)$. We see that α_1 is within the integration range $(0, 1)$, and hence on the physical sheet. But α_2 is outside the integration range $(0, 1)$, and hence, it need not be on the physical sheet. Using dispersion relations, it can be shown that this anomalous threshold does not lie on the physical sheet, see e.g., Itzykson & Zuber [29]. Anomalous thresholds were first studied by Nambu [30] and Karplus et al. [31]. Later, Fowler et al. [32] used Eden's approach to study the anomalous thresholds. Anomalous thresholds have significance in non-relativistic systems, where they are related to composite particles [33, 34]. For our purposes, we consider only the singularities that lie on the physical sheet.

2.2.3 The Triangle Graph

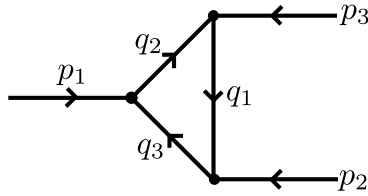


Figure 2.7: The triangle graph.

Now, we consider the implications of the Landau equations on the *triangle graph*. This is a one-loop graph of three propagators with $q_1 = k$, $q_2 = k - p_1$ and $q_3 = k - p_2$. Notice the direction of the internal propagator momenta. This is done purposely, so as to have positive derivatives in the Landau equations. From our previous discussions, we should notice that for the leading singularity, $\gamma = 0$ and $N (= 3)$ is odd, which means we expect a logarithmic branch point at the location of the singularity. The first representation of the Landau equations gives us

$$\begin{aligned} q_1^2 &= m_1^2, \\ q_2^2 &= m_2^2, \\ q_3^2 &= m_3^2. \end{aligned} \tag{2.34}$$

And

$$\alpha_1 q_1^\mu(k) + \alpha_2 q_2^\mu(k) + \alpha_3 q_3^\mu(k) = 0. \tag{2.35}$$

We have added the loop momentum dependence explicitly for clarity. Again, we consider only the invariants. Proceeding similar to the bubble graph solution, we first note that we can construct 6 independent scalar invariants of the internal propagator momenta. 3 of these degrees of freedom can be removed by the on-shell conditions. Finally, we have three vertices giving rise to three 4-momentum conservation relations, which remove the other 3 internal degrees of freedom. Therefore, we can write the solutions to the Landau equations entirely in terms of p_1^2 , p_2^2 , p_3^2 ,

m_1 , m_2 and m_3 . Now, we take a dot product of the equations in (2.35) with q_i^μ . This leads to solving the determinant equation:

$$\det(q_i \cdot q_j) = 0. \quad (2.36)$$

We can make use of the equations in (2.34) together with the 4-momentum conservation relations at the vertices:

$$\begin{aligned} p_1^2 &= (q_2 - q_3)^2, \\ p_2^2 &= (q_3 - q_1)^2, \\ p_3^2 &= (q_1 - q_2)^2, \end{aligned} \quad (2.37)$$

to simplify the determinant equation to

$$\Sigma \equiv \begin{vmatrix} 1 & y_{12} & y_{13} \\ y_{21} & 1 & y_{23} \\ y_{31} & y_{32} & 1 \end{vmatrix} = 0, \quad (2.38)$$

by dividing the determinant equation (2.36) by $m_2^2 m_2^2 m_3^2$, and using

$$y_{ij} \equiv \frac{q_i \cdot q_j}{m_i m_j} = \frac{m_i^2 + m_j^2 - |\sum_k \epsilon_{ijk} p_k|^2}{2 m_i m_j}. \quad (2.39)$$

The solution to the Landau equations given by $\Sigma = 0$, describes a surface in the 6-dimensional complex plane. This, by itself, is too complicated to solve. Instead, we can fix one of the external invariants and solve in terms of the other two external invariants. That is, say we fix $y_{23} = r$, then the determinant equation (2.38) reduces to

$$y_{12}^2 + y_{13}^2 + r^2 - 2r y_{12} y_{13} - 1 = 0. \quad (2.40)$$

Now, this is a surface in the 4-dimensional (complex) $y_{12} - y_{13}$ space, and if we set $\Im(y_{12}) = \Im(y_{13}) = 0$, it describes a conic section in the real $y_{12} - y_{13}$ space, with a discriminant $\Delta = (1 - r^2)$. Now, we have three cases:

- (i) When $\Delta \leq 0$, it describes a hyperbola (or a parabola when the discriminant is exactly equal to 0). This can further be divided into two cases: (1) When $r \leq -1$, the invariant mass corresponding to p_1^2 , say M_1 , obeys $M_1 \geq m_2 + m_3$, which implies M_1 can decay into an m_2 , m_3 pair; (2) when $r \geq 1$, M_1 obeys $M_1 \leq |m_2 - m_3|$, which means it cannot decay into an m_2 , m_3 pair.
- (ii) When $\Delta > 0$, it describes an ellipse (or a circle when $r = 0$). This case corresponds to $r < |1|$, which implies $|m_2 - m_3| < M_1 < m_2 + m_3$. Again, this means M_1 cannot decay into an m_2 , m_3 pair.

This solution is valid only for $\Im(y_{12}) = \Im(y_{13}) = 0$. The full solution requires a 4-dimensional complex space. Tarski [35] introduced a simpler approach to this problem, which gives some insight into the full solution. We consider a line $y_{13} = \lambda y_{12} + \mu$ in the real $y_{12} - y_{13}$ space, where λ and μ are real. Suppose, we fix the value of λ and vary μ . This line can intersect the conic section at two points, one point or no points at all. In the case when there are no intersections, the solutions are no longer real in y_{12} and y_{13} , and are complex conjugate. Or equivalently, outside the region with real solutions, the solution surface never intersects the real $y_{12} - y_{13}$ plane.

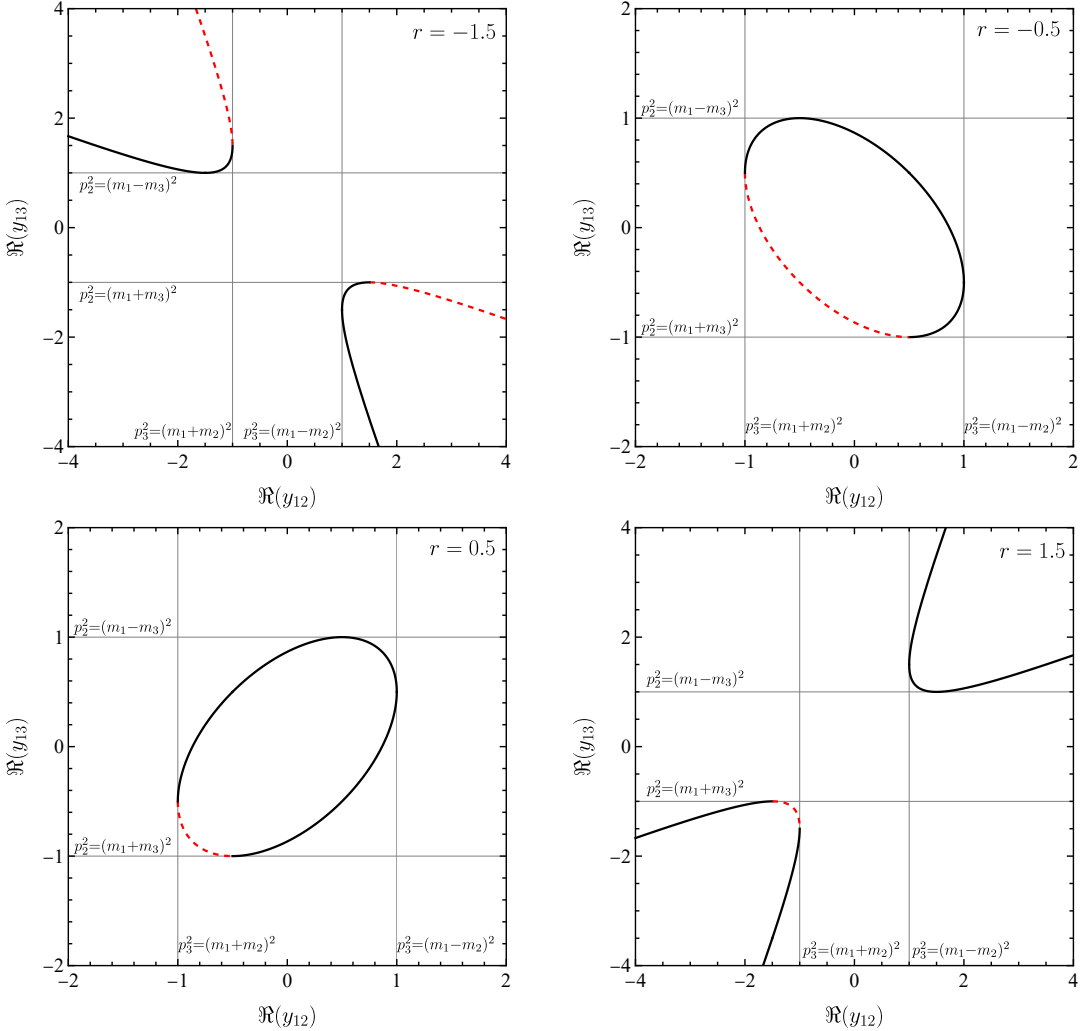


Figure 2.8: The singularity surface of the triangle graph for $\Im(y_{12}) = \Im(y_{13}) = 0$, for some p_1 fixed through r . $r \geq |1|$ corresponds to a hyperbola (or a parabola), see figures at the top left and bottom right. $r < |1|$ corresponds to an ellipse (or a circle), see figures at the top right and bottom left. The horizontal and vertical lines correspond to the two-body thresholds in the p_2 and p_3 channels, respectively. These are exactly the subleading singularities corresponding to q_2 and q_3 contractions. Finally, the dashed red segments correspond to real and positive α 's. M_1 decay to m_2 and m_3 is allowed only for $r \leq -1$, see figure at the top left.

Also, the sign of λ is going to determine the relative sign between the imaginary parts of y_{12} and y_{13} . This implies that outside the region with real solutions, there are two complex surfaces attached, each corresponding to a particular choice of the relative sign between the imaginary parts. This way, one can categorise the regions corresponding to the full solution. However, we still have to solve the entire determinant equation, in order to get the exact solutions.

Now, we recall that the first representation of the Landau equations does not tell us which sheet the singularity is located on. To determine this, we need to use the second or the third representation of the Landau equations. Using the second or third representation also lets us fix the absolute sign of the imaginary parts. In the third representation of the Feynman integral, one can show that the denominator

takes the form:

$$D = \alpha_2\alpha_3 p_1^2 + \alpha_3\alpha_1 p_2^2 + \alpha_1\alpha_2 p_3^2 - (\alpha_1 + \alpha_2 + \alpha_3) \sum_{i=1}^3 \alpha_i m_i^2. \quad (2.41)$$

The corresponding Landau equations are given by

$$\left(\sum_{j,k=1}^3 |\epsilon_{ijk}| \alpha_j p_k^2 \right) - (\alpha_1 + \alpha_2 + \alpha_3) m_i^2 - \sum_{l=1}^3 \alpha_l m_l^2 = 0, \quad (i = 1, 2, 3). \quad (2.42)$$

It can be shown that this equation is equivalent to the first representation of the Landau equations. Using this, one can determine which parts of figure 2.8 — dashed red segments — correspond to the singularities on the physical sheet. We do this explicitly in the next section. But to motivate this result for now, notice that the boundaries of the conic sections are exactly the normal and anomalous two-body thresholds. These points correspond exactly to the case when either $\alpha_3 = 0$, which implies $p_3^2 = (m_1 \pm m_2)^2$, or $\alpha_2 = 0$, which implies $p_2^2 = (m_1 \pm m_3)^2$. We also know that the respective α 's are positive for the normal threshold, and they're of the opposite signs for the anomalous threshold. Now, α_1 never vanishes, since for $r \neq 1$, p_1^2 does not correspond to two-body thresholds. This means that α_1 has to be always positive. These arguments let us pick the consistent region that has all α 's positive — particularly on the ellipse, the region that is between the normal thresholds, and has no α 's vanishing. Similar arguments can be made for other conic sections. These are nothing but the singularities corresponding to the contracted graphs. To make sure that the integration over α 's are meaningful, we can add a $-i\epsilon$ to the masses squared of the internal propagator. This tells us how the singularities approach the real integration contours, and relates neatly to the *S-matrix theory* postulate that all transition amplitudes are obtained as the boundary values of some analytic function [36]. Now, it can be shown that the kinematical singularities lie on the physical sheet for positive real α 's, see Coleman and Norton [37]. When this is not satisfied, the kinematical singularities do not lie on the physical sheet, since a deformation is possible to avoid the singularities. However, these singularities can still be reached by crossing a cut and moving to a different Riemann sheet, from where a deformation is not possible. Though, these Riemann sheets are in the α -space, which have no physical significance. To motivate the above result, recall that the α integrations run from 0 to 1, and the singularities on the physical sheet correspond to the undistorted α hypercontour. We also argued that the other endpoint, $\alpha = 1$, is not an endpoint due to the homogeneity arising from the δ -function. This amounts to the condition that α 's are real and positive. A rigorous proof of this requires topology, see e.g., Fotiadi et al. [18]. Also, using the third representation equations, one can find the solutions that correspond to the singularities in the physical sheet for the case when $\Im(y_{12}) = \Im(y_{13}) = 0$, see figure 2.8.

Finally, we discuss the subleading Landau singularities in the triangle graph. From lemma 2.2.1, we know that the graphs obtained by a single contraction are equivalent to a bubble graph. The value of γ is 1/2, and hence, we expect a (square root) branch point at the location of the singularity. The solutions to the Landau equations are identical to the bubble graph solutions, except that we will have two

singularities corresponding to every contraction. These singularities are the two-body thresholds of the respective channels. From lemma 2.2.2, we know that two contractions are not possible in this case, since it leads to a graph with trivial analyticity properties.

2.2.4 The Square Graph

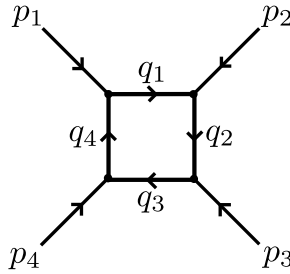


Figure 2.9: The square graph.

We briefly discuss the implications of the Landau equations on the *square graph*. This is a one-loop graph of four propagators, with a loop momentum k . From our previous discussions, we can see that $\gamma = 1/2$, which means that the leading singularity is a (square root) branch point. The first representation of the Landau equations gives us

$$\alpha_i(q_i^2 - m_i^2) = 0, \quad (i = 1, 2, 3, 4). \quad (2.43)$$

And

$$\alpha_1 q_1^\mu(k) + \alpha_2 q_2^\mu(k) + \alpha_3 q_3^\mu(k) + \alpha_4 q_4^\mu(k) = 0. \quad (2.44)$$

Solving the above system of equations in a similar fashion, we notice that we can construct 10 independent scalar invariants with the internal propagator momenta. For the leading singularity, none of the α 's are equal to zero, which means that all the internal propagators go on-shell. This removes 4 internal degrees of freedom. We have four vertices, giving rise to four 4-momentum conservation relations. These remove 4 further internal degrees of freedom. We still have to determine $q_1 \cdot q_3$ and $q_2 \cdot q_4$. This can be done by constructing the Mandelstam invariants $s = (p_1 + p_2)^2$ and $t = (p_2 + p_3)^2$. Therefore, we can write the solutions to the Landau equations entirely in terms of $p_1^2, p_2^2, p_3^2, p_4^2, s, t, m_1^2, m_2^2, m_3^2, m_4^2$. Now taking a dot product of equation (2.43) with q_j^μ , we get a determinant equation similar to that of the triangle graph:

$$\det(q_i \cdot q_j) = 0. \quad (2.45)$$

In this case we have a determinant of a 4×4 matrix, instead of a 3×3 matrix. Now,

if we define

$$\begin{aligned}
 y_{12} &= \frac{m_1^2 + m_2^2 - p_2^2}{2m_1m_2}, \\
 y_{23} &= \frac{m_2^2 + m_3^2 - p_3^2}{2m_2m_3}, \\
 y_{34} &= \frac{m_3^2 + m_4^2 - p_4^2}{2m_3m_4}, \\
 y_{14} &= \frac{m_1^2 + m_4^2 - p_1^2}{2m_1m_4}, \\
 y_{24} &= \frac{m_2^2 + m_4^2 - s}{2m_2m_4}, \\
 y_{13} &= \frac{m_1^2 + m_3^2 - t}{2m_1m_3},
 \end{aligned} \tag{2.46}$$

we can rewrite the determinant in the following form:

$$\Sigma \equiv \begin{vmatrix} 1 & y_{12} & y_{13} & y_{14} \\ y_{12} & 1 & y_{23} & y_{24} \\ y_{13} & y_{23} & 1 & y_{34} \\ y_{14} & y_{24} & y_{34} & 1 \end{vmatrix} = 0. \tag{2.47}$$

The solution to the Landau equations given by $\Sigma = 0$, describes a surface in the 8-dimensional complex space. An analysis similar to that of the triangle graph can be carried out. We do not go further into studying the solutions of the square graph, since it is rather tedious. We note again that in order to study which sheet the singularities lie in, we need to consider the second or the third representation of the Landau equation. The denominator in the third representation of the Feynman integral for the square graphs takes the following form:

$$\begin{aligned}
 D &= \alpha_2\alpha_4s + \alpha_1\alpha_3t + \alpha_4\alpha_1p_1^2 + \alpha_1\alpha_2p_2^2 \\
 &\quad + \alpha_2\alpha_3p_3^2 + \alpha_3\alpha_4p_4^2 - \left(\sum \alpha_i m_i^2 \right) (\alpha_1 + \alpha_2 + \alpha_3 + \alpha_4).
 \end{aligned} \tag{2.48}$$

Applying the rules discussed so far, we can arrive at the third representation of the Landau equations corresponding to the square graph. The subleading Landau singularity can be arrived at by considering valid contractions. With one contraction, we get graphs with $\gamma = 0$ and odd $N (= 3)$, which means we expect the singularity to be a logarithmic branch point. The corresponding Landau equations are identical to the triangle graph equations, which were studied in the previous section. A second contraction takes us to graphs with $\gamma = -1/2$, which means we expect the singularity to be a (square root) branch point. The corresponding Landau equations are identical to the bubble graph equations. Also, these are exactly the two-body thresholds corresponding to the respective external momenta channels.

Before we move on to the next section, we should mention that the Landau equations tell us the location of the singularities. But they do not let us actually calculate the discontinuity of the integral, for example when the non-analyticity is of square root or logarithmic branch point of nature. To calculate the discontinuity of the integral, one needs to make use of Cutkosky rules [24]. Roughly, the Cutkosky rules state that the discontinuity is given by replacing each on-shell propagator with $\delta^{(+)}(p_i^2 - m_i^2)$, where p_i is the corresponding propagator momentum and m_i is the

corresponding on-shell mass. This is briefly discussed in appendix A. Taylor [38] studied geometric solutions corresponding to the Landau equations. In such an analysis, the solutions are arrived at through *dual diagrams*. This is briefly discussed in appendix B.

2.3 Applications to the $a_1(1420)$ System

In this section, we apply the results discussed so far to the system of $a_1(1420)$. In the context of three-body infinite volume unitarity, which is discussed in a later chapter, we are interested in the kinematical singularities not just at the 1-loop level, but also at higher levels. We first apply the Landau equations to the triangle level, followed by the application to the higher levels.

2.3.1 The 1-loop (Triangle) Level

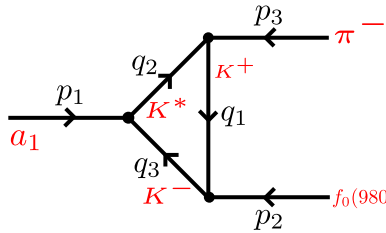


Figure 2.10: The $a_1(1420)$ system at the 1-loop (triangle) level. The intermediate particles are taken as K^* , K^+ and K^- , and one of the outgoing particle is taken as π^- . It can be shown that such a diagram has a triangle singularity in the region of interest, when the other outgoing particle is f_0 .

As discussed when the $a_1(1420)$ system was first introduced, the motivation is to explain the peak structure around 1.4 GeV in the 3π spectrum. To that end, we assume that an incoming particle decays to 3π , through a triangle like diagram, see figure 2.10. The particles that make up the triangle are taken to be K^* , K^+ and K^- . These are taken as stable particles with well defined on-shell masses m_1 , m_2 and m_3 , indexed by their momenta. Recall that we require the intermediate particles to go on-shell to have a kinematical singularity. One of the outgoing particles is taken as π^- . We mention again that the directions of the propagators are chosen so as to avoid an arbitrary minus in front of some terms of the Landau equation. It might look like conservation of electric charge is not respected at a few vertices in this diagram, and in the diagrams in the next couple of subsections. However, this is artificial, and the conservation of electric charge is restored when the directions of the propagators are considered properly. This is not a problem since the form of the propagator remains unaffected by the charge of the scalar. Now, we can apply the results from the previous section to this system. Particularly, the determinant equation (2.38) leads to

$$y_{13}^2 + y_{23}^2 + r^2 - 2r y_{13} y_{23} - 1 = 0. \quad (2.49)$$

Here, $y_{13} = (m_1^2 + m_3^2 - p_2^2)/(2m_1 m_3)$, $y_{23} = (m_2^2 + m_3^2 - s)/(2m_2 m_3)$ and $r = y_{12} = (m_1^2 + m_2^2 - m_\pi^2)/(2m_1 m_2)$. Note that we have taken the incoming invariant mass

as s , and used that the invariant mass of the pion is m_π . We assume the external particles to be observables, therefore their momenta must be real. We can invert the above equations and solve for the external invariants. Since we are looking for real solutions, this reduces to the easier case of vanishing imaginary parts discussed before. Taking the masses from PDG [39] as $m_1 = 0.493$ GeV, $m_2 = 0.892$ GeV, $m_3 = 0.493$ GeV and $m_\pi = 0.139$ GeV, we can see that $r \geq 1$ and the discriminant $\Delta = 1 - r^2 \leq 1$. Following our discussion, we know that this corresponds to a hyperbola in the y_{13} - y_{23} plane. We also argued that the singularities on the physical sheet must have real and positive α 's. And for the triangle singularity, this corresponds to the region with the two-body thresholds as the boundary points — in this case the region between $p_2^2 = (m_1 + m_3)^2$ and $s = (m_2 + m_3)^2$. One can evaluate the value of s corresponding to $p_2^2 = (m_1 + m_3)^2$, and likewise for the other two-body threshold. This lets us determine the region in which the triangle singularity is present. The resulting region is given by

$$\begin{aligned} p_2 &\in \left\{ (m_1 + m_3), \sqrt{(m_1^2 + m_3^2) + \frac{m_3}{m_2}(m_1^2 + m_2^2 - m_\pi^2)} \right\}, \\ \sqrt{s} &\in \left\{ (m_2 + m_3), \sqrt{(m_2^2 + m_3^2) + \frac{m_3}{m_1}(m_1^2 + m_2^2 - m_\pi^2)} \right\}. \end{aligned} \quad (2.50)$$

Now, plugging in the corresponding masses gives us, $p_2/\text{GeV} \in [0.986, 1.024]$ and $\sqrt{s}/\text{GeV} \in [1.385, 1.436]$. We can see that the mass of the $f_0 = 0.99$ GeV, lies in the region which can have a triangle singularity. This can then decay to 2π , resulting in the final 3π spectrum. Alternatively, one may set the other outgoing invariant equal to the mass of f_0 , and solve for the determinant equation, which now is just a quadratic equation. That is, $p_2^2 = m_{f_0}^2$. Then, the two roots are given by

$$y_{23} = y_{13}r \pm \sqrt{(1 - y_{13}^2)(1 - r^2)}. \quad (2.51)$$

Plugging in the masses and solving for \sqrt{s} , we get, $\sqrt{s} = 1.408$ GeV and $\sqrt{s} = 1.472$ GeV. We can see that only the first root corresponds to a singularity in the physical sheet, whereas the second one does not. We can also verify it using the second or the third representation of the Landau equations. For example, the singularity surface in the case of the second representation reads:

$$D = \alpha_1(q_1^2 - m_1^2) + \alpha_2(q_2^2 - m_2^2) + \alpha_3(q_3^2 - m_3^2). \quad (2.52)$$

Note that the α 's here are the Feynman parameters and not the parameters associated with the Landau equations. Following our previous discussions, one can derive an explicit condition for all α 's to be positive reals. This reads:

$$\frac{2m_3^2(m_1^2 + m_2^2 - m_\pi^2) - (m_1^2 + m_3^2 - p_2^2)(m_2^2 + m_3^2 - s)}{\lambda(p_2^2, m_1^2, m_3^2)} \leq 0. \quad (2.53)$$

Here, λ is the Källén triangle function given by

$$\lambda(x, y, z) = x^2 + y^2 + z^2 - 2xy - 2yz - 2zx. \quad (2.54)$$

One can readily verify that this condition is satisfied by the first root, but not satisfied by the second root. Additionally, we also have the subleading singularities

corresponding to the normal thresholds, arising from the contracted graphs. This corresponds to $\sqrt{s} = 1.385$ GeV and $p_2 = 0.986$ GeV respectively, which are also the boundaries of the regions in which a triangle singularity can be observed. The condition for a triangle singularity has a very neat geometric interpretation through dual diagram, which is briefly discussed in appendix B.

Before we move on, we briefly discuss the singularities corresponding to the triangle diagrams given in figure 2.11. These graphs may look irrelevant now, but

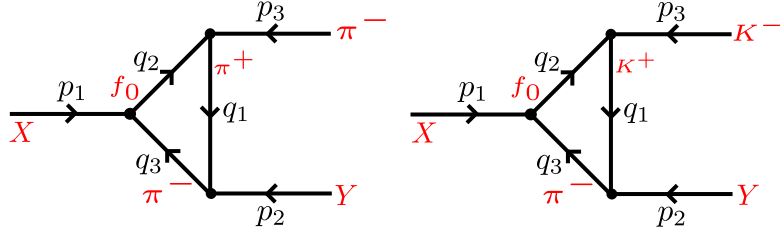


Figure 2.11: Triangle graphs with different intermediate particles. This is relevant to our study of the $a_1(1420)$ in the three-body unitary formalism. Here, X and Y denote the invariant mass ranges obtained as the solutions to the Landau equations.

they become so at a later point, when implementing three-body unitary formalism. This relevance will be discussed later. The physical sheet solutions corresponding to the triangle singularity in the first graph is given by, $p_2/\text{GeV} \in [0.278, 0.420]$ and $\sqrt{s}/\text{GeV} \in [1.129, 1.407]$, and the physical sheet solutions corresponding to the triangle singularity in the second graph is given by, $p_2/\text{GeV} \in [0.632, 0.657]$ and $\sqrt{s}/\text{GeV} \in [1.129, 1.157]$. The region corresponding to the first graph has a triangle singularity very close to the \sqrt{s} region we are after — around 1.4 GeV. But it should be noted that the invariant corresponding to the other outgoing particle is much lower than the mass of f_0 . The region corresponding to the second graph is narrower, since the first outgoing particle is a kaon instead of a pion. Besides, the triangle singularity is not in the \sqrt{s} region we are interested in.

2.3.2 The $1 + 1$ -loop (Triangle+1) Level

Now, we look at the system at the $1 + 1$ -loop level, see figure 2.12. Note again that we have chosen the directions of the momenta, such that the derivatives in the Landau equation are always positive. In this case, we have two independent loop

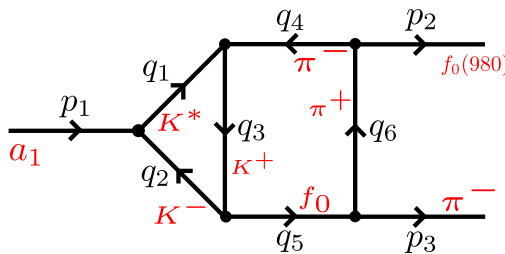


Figure 2.12: The $a_1(1420)$ at the $1 + 1$ -loop (Triangle+1) level. Again, we take the outgoing particles to be π^- and f_0 , and we look for kinematical singularities in the \sqrt{s} region we are interested in.

momenta — one from the triangle, and one from the box. Therefore, we have two

independent sets of Landau equations to solve:

$$\begin{aligned}\alpha_1 q_1^\mu + \alpha_2 q_2^\mu + \alpha_3 q_3^\mu &= 0, \\ \alpha_3 q_3^\mu + \alpha_4 q_4^\mu + \alpha_5 q_5^\mu + \alpha_6 q_6^\mu &= 0.\end{aligned}\quad (2.55)$$

For the leading singularity, none of the α 's are 0. The first equation leads to the determinant equation (2.38), with the definitions:

$$\begin{aligned}y_{12} = y_{21} &= \frac{m_1^2 + m_2^2 - s}{2m_1 m_2}, \\ y_{13} = y_{31} &= \frac{m_1^2 + m_3^2 - m_4^2}{2m_1 m_3}, \\ y_{23} = y_{32} &= \frac{m_2^2 + m_3^2 - m_5^2}{2m_2 m_3}.\end{aligned}\quad (2.56)$$

In this case, $m_1^2 = m_{K^*}^2$, $m_2^2 = m_3^2 = m_K^2$, $m_4^2 = m_\pi^2$ and $m_5^2 = m_{f_0}^2$, and it can be seen that this reduces the exact triangle determinant equation from the previous subsection. Therefore, the range of possible solutions are the same: $m_5/\text{GeV} \in [0.986, 1.024]$ and $\sqrt{s}/\text{GeV} \in [1.385, 1.436]$. In fact, m_5 corresponds to an exact value of m_{f_0} , which leads to $\sqrt{s} = 1.408$ GeV. Now, the second equation leads to the determinant equation (2.47), with the definitions:

$$\begin{aligned}y_{34} = y_{43} &= \frac{m_3^2 + m_4^2 - m_1^2}{2m_3 m_4}, \\ y_{35} = y_{53} &= \frac{m_3^2 + m_5^2 - m_2^2}{2m_3 m_5}, \\ y_{46} = y_{64} &= \frac{m_4^2 + m_6^2 - p_2^2}{2m_4 m_6}, \\ y_{56} = y_{65} &= \frac{m_5^2 + m_6^2 - m_\pi^2}{2m_5 m_6}, \\ y_{45} = y_{54} &= \frac{m_4^2 + m_5^2 - s}{2m_4 m_5}, \\ y_{36} = y_{63} &= \frac{m_3^2 + m_6^2 - t}{2m_3 m_6},\end{aligned}\quad (2.57)$$

with, $m_6^2 = m_\pi^2$. This set of equations has an additional degree of freedom that needs to be fixed: $t = (q_1 - p_2)^2 = (q_2 + p_3)^2$. This is fixed by working in the centre of mass reference frame of the system. But the invariant derived is independent of the frame of reference:

$$\begin{aligned}t = m_1^2 + p_2^2 - \frac{1}{2s}(s + m_1^2 - m_2^2)(s + p_2^2 - m_\pi^2) \\ + \frac{1}{2s}\lambda^{1/2}(s, m_1^2, m_2^2)\lambda^{1/2}(s, p_2^2, m_\pi^2).\end{aligned}\quad (2.58)$$

With this, the determinant equation can be solved numerically for p_2 , given $p_3^2 = m_\pi^2$ and $\sqrt{s} = 1.408$ GeV. We find that the solution to the invariant mass is $p_2 = 0.527$ GeV. This lies quite far from the range in which the triangle singularity was calculated to be in the 1-loop level, and much smaller than the mass of the f_0 . In principle, one also needs to verify that this singularity actually lies on the

physical sheet, by verifying whether all the corresponding α 's are positive reals. We do not verify that here, and we rest further discussion for now, and get back to this in the context of three-body unitary formalism.

Further, we can also calculate the regions corresponding to the subleading singularities. The $1 + 1$ -loop diagram has 6 propagators in total, and hence, we can have graphs with at most 4 contractions, before reaching graphs with trivial analyticity properties, see lemma 2.2.2. Also, the graphs corresponding to 4 contractions result in the respective two-body thresholds. At first sight, it might look like we have $\binom{6}{1} = 6$ single contractions, $\binom{6}{2} = 15$ double contractions, and $\binom{6}{3} = 20$ triple contractions. However, a lot of them result in graphs with trivial analyticity properties through lemma 2.2.2. For example, a double contraction of the propagators corresponding α_1 and α_2 , results in the first determinant equation being trivial. We follow similarly to what was done for the leading singularity, and we find that we do not have subleading singularities for the outgoing invariant mass close to the mass of the f_0 . In principle, one must also verify whether the obtained subleading singularities lie on the physical sheet, as mentioned before.

2.3.3 Singularities in Multi-loop Diagrams

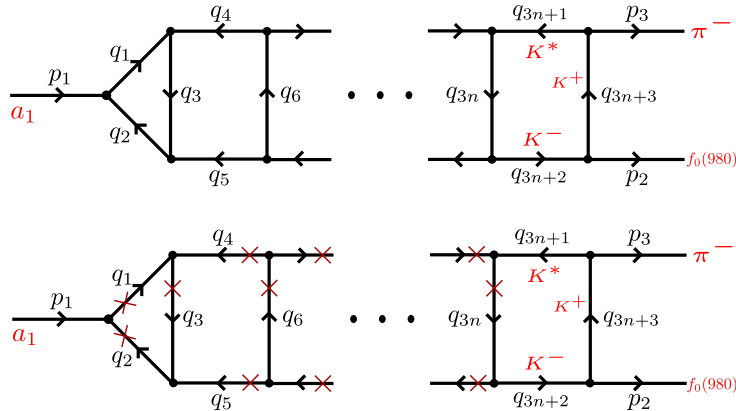


Figure 2.13: The $a_1(1420)$ with $1 + n$ loops and $3n + 3$ internal propagators. Here, n is the number of loops beyond the first triangle. There is no leading singularity in the \sqrt{s} region we are interested in. However, there are subleading singularities corresponding to certain contractions, e.g., the one from the bottom graph, that leads to the same triangle singularity. Note that this is possible only when one has $1 + 2$ loops or more, since we cannot have a $K^*K^+K^-$ triangle at the very first loop beyond the first triangle (see previous subsection).

Next, we briefly consider the possible singularities arising at higher levels. By higher levels, we mean graphs with $1 + n$ loops, where n is the number of additional loops added beyond the first triangle. This graph has $3n + 3$ internal propagators, see the top image in figure 2.13. In the previous case, we saw that for the leading singularity, we have every internal propagator going on-shell. This meant that the incoming energy had an exact solution to the Landau equation, which was then used to determine the outgoing invariant masses corresponding to the singularity. In all the $1 + 1$ -loop diagrams we considered, the outgoing invariant p_2 lied far from the on-shell mass of both K^* and f_0 . This meant that the propagators in the

$1 + 2$ level cannot go on-shell for the considered incoming energy. Alternatively, one may also set all the propagators until $1 + 2$ level on-shell, and solve for the corresponding incoming energy. This amounts to solving the exact equation obtained in the previous case, instead now it is solved for the incoming energy. The numerical solution to this polynomial equation gives negative values for s , which means that \sqrt{s} has to be complex. This, again, is far from the \sqrt{s} region we are interested in, which is about 1.4 GeV. Now, we recall that the Landau equations lead to solving $1 + n$ determinant equations, that are solved simultaneously:

$$\begin{aligned} \sum_{i=1}^3 \alpha_i Q_{ij} &= 0, \quad (j = 1, 2, 3) \\ \sum_{i=3}^6 \alpha_i Q_{ij} &= 0, \quad (j = 3, \dots, 6) \\ &\vdots \\ \sum_{i=3n}^{3n+3} \alpha_i Q_{ij} &= 0, \quad (j = 3n, \dots, 3n+3), \end{aligned} \tag{2.59}$$

where $Q_{ij} = q_i \cdot q_j$, and the matrix Q is symmetric. At this point, we have shown that the first two determinants do not have a solution in the incoming invariant mass region we are interested in. Recall that we are looking for a solution that satisfies all the above equations simultaneously. Non-existence of a simultaneous solution for the first two equations is enough to conclude that we do not have a leading singularity in the region of interest, which is $\sqrt{s} \approx 1.4$ GeV. There are various subleading singularities corresponding to different contractions of the original graph. We do not categorise these singularities. However, there is a very interesting contraction that is of relevance to us. For the $1 + n$ level ($\mathbb{N} \ni n \geq 2$), consider contracting all the propagators, except the last three propagators. That is, contract the propagators with momenta q_1, \dots, q_{3n} , leaving us with only the propagators with momenta q_{3n+1}, q_{3n+2} and q_{3n+3} (see the bottom image in figure 2.13). We can see that this contracted graph is essentially the original triangle system with a logarithmic singularity, due to lemma 2.2.1. And hence, it must have the same regions of singularity in the incoming and the outgoing invariant masses. Therefore, we expect triangle singularities to appear at the same location for graphs with $1 + 2$ or more loops. This is, in principle, not that different from a two-body threshold appearing at higher levels, when the right invariant mass is studied. Also, this subleading triangle singularity is not possible at the $1 + 1$ level (see, previous subsection), because we cannot have a $K^* K^+ K^-$ triangle at the very first loop beyond the first triangle, by the virtue of the way we construct our system. This will be clear when the possible channels are discussed in the context of three-body unitary formalism.

To summarise what we have at this point, we applied the Landau equations to the $a_1(1420)$ system, and we determined the singular regions in terms of the incoming and the outgoing invariant masses at the triangle level. Further, we studied the singular regions in the higher order graphs, since this is of relevance to us in the context of three-body unitary formalism. We expect no triangle singularity at the $1 + 1$ -loop level, but expect this to appear again at higher levels. Finally, we mention that all the internal propagators are taken as stable scalars in our analysis, for now.

In the non-unitary models, which is discussed in the next chapter, one adds an arbitrary imaginary part to the unstable propagators, leading to meaningful results. This arbitrary inclusion is motivated by the finite widths of $K^*(892)$ and $f_0(980)$, but is an approximation. However, it is more enriching to study this within a model which inherently takes care of this, and also includes possible resummation effects. This is discussed in a later chapter, and is the core objective of this study.

Chapter 3

Triangle Singularities in Non-Unitary Models

Sometimes, such effects (*kinematical singularities*) mimic the behaviour of a resonance, and lay traps on the way of establishing an unambiguous hadron spectroscopy. It is thus important to distinguish kinematic singularities from genuine resonances.

F.-K. Guo et al., p.5,
Threshold Cusps and Triangle Singularities in Hadronic Reactions [40]

We now turn to the question of how kinematical singularities manifest in the invariant mass distributions. For example, in the case of the bubble graph, we recall that the singularities arising from the Landau equations correspond to square root branch points. The “normal” threshold corresponds to the two-body threshold, which manifests as a cusp in the evaluated amplitudes, whereas the “anomalous” threshold does not lie on the physical boundary, and its effect is not as obvious. In the case of loosely bound states, and within the context of non-relativistic quantum mechanics, one can relate this to the spatial extension of the wave function, see Martin [41]. In the case of the triangle graph, we recall that the singularities arising from the Landau equations correspond to logarithmic branch points. If we choose the right invariants, we should be able to observe this singularity in the evaluated amplitudes. This chapter is organised as follows: we first briefly discuss the background for kinematical singularities, particularly triangle singularities, in hadronic reactions. Then we evaluate the amplitudes corresponding to a naïve triangle graph consisting of scalar propagators. We then evaluate the amplitudes corresponding to a graph at the triangle+1 loop level. Finally, we compare the obtained results with our expectations from the previous chapter. Parts of the following discussion closely follow the review of triangle singularities by Guo et al. [40].

The nature of triangle singularity makes it possible to have a resonance-like structure without a resonance. In the aftermath of the proposal of the Landau equations, many attempts were made to relate the kinematical singularities to experimental observations. The Peierls mechanism [42] was proposed to explain the second resonance in $\Delta\pi \rightarrow \Delta\pi$ reaction, through an N exchange. However, it was later shown that this triangle singularity does not lie on the physical sheet, see Goebel [43]. Such an analysis was too restrictive, i.e., it did not have enough freedom in the external invariant masses to have a kinematical singularity on the physical sheet. One can,

instead, fix two of the three external invariants, and investigate the singularities that lie on the physical sheet for the other external invariant. But Schmid [44] later argued that in the case of elastic rescattering, there should be no trace of the triangle singularity in the integrated invariant mass distributions. That is, consider $m_0 \rightarrow m_A + (m_B + m_C)$. At the tree level, one does not have any rescattering. But at the 1-loop level m_B and m_C rescatter off each other. Schmid, then, argued that the effect of such a triangle singularity must be nothing but an overall multiplication of the tree level amplitude by a phase factor. The situation is very different when the requirement of elasticity is relaxed, which is what we are after. In this case, there is still another subtle point. Not all of the internal propagators can be totally stable against decay. In the following, we consider a naïve system with scalar propagators. The instability of some of the propagators is taken into account by giving them an arbitrary imaginary component, related to their physical width. For the effect of the propagator width on kinematical singularities, see Du & Zhao [45]. It should also be noted that by “propagator width”, we mean the width of the corresponding state, throughout this work. No confusion should arise in this regard.

3.1 Kinematical Singularities in the Triangle Graph

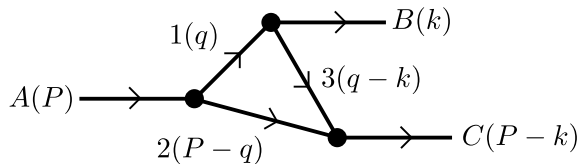


Figure 3.1: We consider a triangle loop consisting of three scalar propagators, labelled as 1, 2 and 3, with the given momenta. The external particles are given by A , B and C .

Now, we will explicitly calculate the amplitudes corresponding to a naïve model, with stable internal propagators. Such an analysis was originally carried out by Bayar et al. [46], and extensively reviewed later by Guo et al. [40]. Consider the graph given in figure 3.1. In this example, all the particles are scalars, and the Feynman integral corresponding to the loop diagram is given by

$$I(k) = i \int \frac{d^4 q}{(2\pi)^4} \frac{1}{(q^2 - m_1^2 + i\varepsilon)((P - q)^2 - m_2^2 + i\varepsilon)((q - k)^2 - m_3^2 + i\varepsilon)}. \quad (3.1)$$

Notice however, that the overall δ -function corresponding to 4-momentum conservation, and the external scalar factors are all ignored, since the singularity structure is a part of the loop integral. Since for the triangle singularity, all the internal propagators need to go on-shell, one may consider only the positive energy part of the

scalar propagators, which leads to

$$I(|\mathbf{k}|) \approx \frac{i}{8m_1 m_2 m_3} \int \frac{d^4 q}{(2\pi^4)} \times \frac{1}{(q^0 - \omega_1(\mathbf{q}) + i\varepsilon)((P^0 - q^0) - \omega_2(\mathbf{q}) + i\varepsilon)((q^0 - k^0) - \omega_3(\mathbf{q} - \mathbf{k}) + i\varepsilon)}. \quad (3.2)$$

Here, the on-shell condition for the internal propagators has been used. The negative energy part of the propagators giving rise to $\omega_1 \omega_2 \omega_3$ is approximated as $8m_1 m_2 m_3$, and $\omega_i(\mathbf{p}) = \sqrt{\mathbf{p}^2 + m_i^2}$ is the on-shell energy of the corresponding particle. Now, one may make use of Cauchy's integral theorem, and carry out the integral over the 0-th component of the 4-momentum integral. This gives

$$I(|\mathbf{k}|) = \frac{-1}{16\pi^2 m_1 m_2 m_3} \int_0^\infty d|\mathbf{q}| \frac{\mathbf{q}^2}{P^0 - \omega_1(\mathbf{q}) - \omega_2(\mathbf{q}) + i\varepsilon} \times \int_{-1}^1 dz \frac{1}{P^0 - \omega_B(\mathbf{k}) - \omega_2(\mathbf{q}) - \sqrt{m_3^2 + \mathbf{q}^2 + \mathbf{k}^2 - 2|\mathbf{q}||\mathbf{k}|z + i\varepsilon}}. \quad (3.3)$$

In the above equation, the last term in the denominator of the second integral $\omega_3(\mathbf{q} - \mathbf{k})$, is expanded out to show the angular dependence explicitly. This angular integral results in a logarithm, which has branch points at $z = \pm 1$. These are also exactly the endpoint singularities associated with this integral. This is discussed in the next chapter. In the centre of mass frame of reference of the incoming particle A , $P^0 - \omega_B(\mathbf{k})$ reduces to $(s - m_B^2 + m_C^2)/(2\sqrt{s})$, where $\sqrt{s} = m_A$ is the incoming invariant mass. Now, in the centre of mass frame, one can also show that

$$|\mathbf{k}| = \frac{\lambda^{1/2}(s, \sigma, m_B^2)}{2\sqrt{s}}, \quad (3.4)$$

where λ is the Källén triangle function defined by equation (2.54), and σ is the outgoing invariant corresponding to C ($= m_C$). Note that the above integral's dependency on the incoming invariant mass is implicit. This lets one write the integral as function of s and σ :

$$I(|\mathbf{k}|) \equiv I(s, \sigma). \quad (3.5)$$

One may now investigate the amplitudes as a function of the incoming and outgoing invariant masses, with the outgoing invariant mass B fixed. In the following, we fix this at the invariant mass of the pion. Also, the internal propagators are taken to be $m_1 = m_{K^*}$ and $m_2 = m_3 = m_K$. Before we discuss the results corresponding to the integral, we briefly mention the numerical implementation of the integral. One replaces the mass m_1 , of the internal propagator corresponding to K^* , with $m_1 - i\Gamma/2$, thus giving the K^* propagator a finite width. Also, the logarithmic singularity in the angular integral is handled by adding a small imaginary part to it. A more rigorous way of dealing with this is discussed in the next chapter. Finally, it should be noted that the integral is linearly divergent. This does not affect the singularity structure, but to make comparisons between different widths of the K^* propagator meaningful, we subtract the large momentum behaviour of the integral up to linear order, from every evaluated point. The integral is solved numerically, with a hard cut-off of 1 GeV. The evaluated amplitudes are given in figure 3.2.

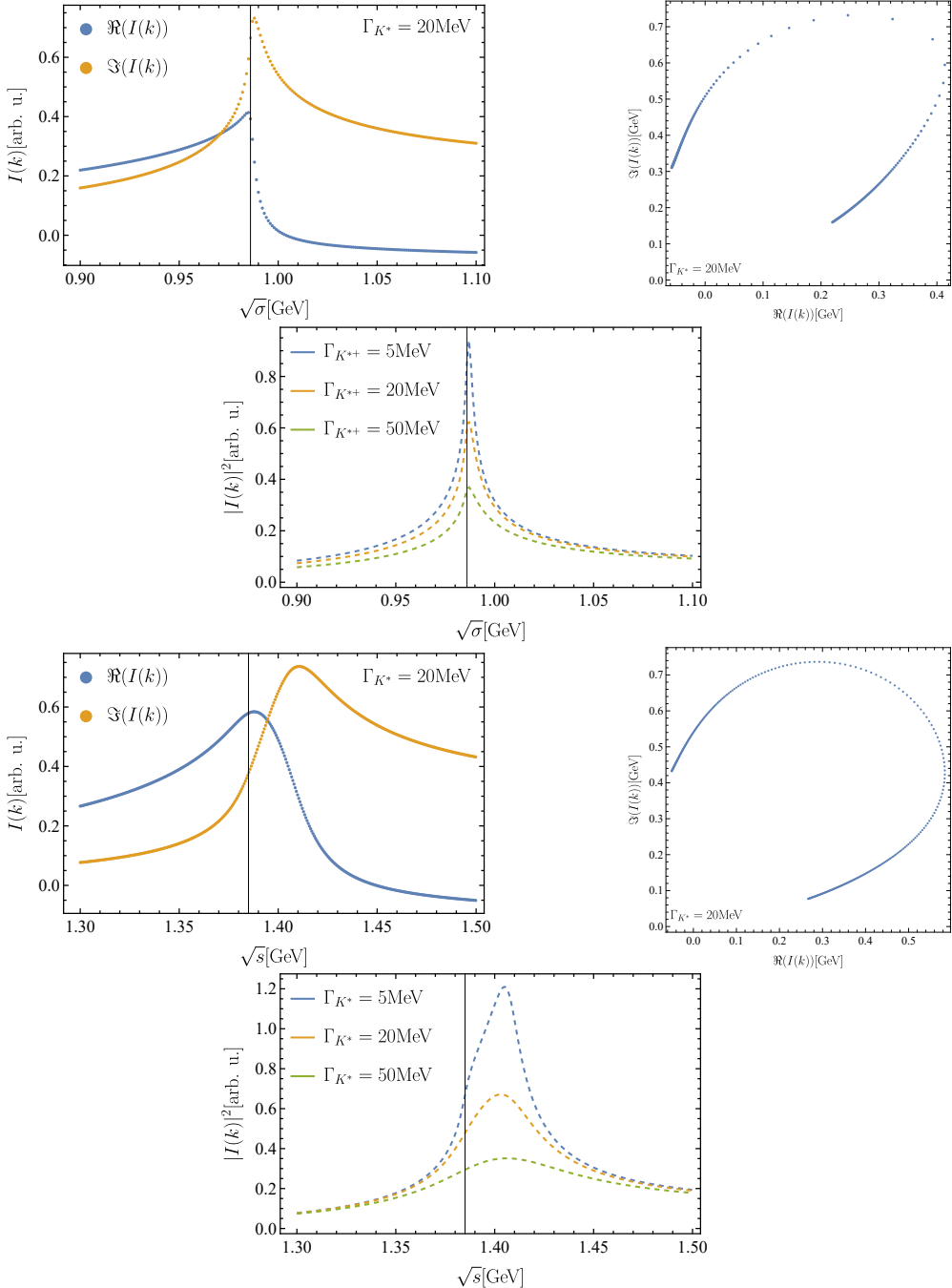


Figure 3.2: The first three plots show the triangle graph loop integral evaluated as a function of $\sqrt{\sigma}$, at fixed $\sqrt{s} = 1.42 \text{ GeV}$. Here, the black line denotes the two-body $m_K + m_K$ threshold. The latter three plots show the triangle graph loop integral evaluated as a function of \sqrt{s} , at fixed $\sqrt{\sigma} = 0.99 \text{ GeV}$. Here, the black line denotes the two-body $m_{K^*} + m_K$ threshold. The first plot in each set shows the real and imaginary parts of the amplitudes for a K^* propagator width of 20 MeV. The second plot in each set shows the corresponding Argand plot. The third plot in each set shows the absolute squared of the amplitudes evaluated for different K^* propagator widths. The amplitudes are given in arbitrary units, since the couplings are set to unity.

One should now relate this to our expectations from the previous chapter. It can be seen from the figures that, when the integral is evaluated at the invariant corresponding to the kinematical singularity, it results in a Breit-Wigner-like peak in the second set of plots. In the first set of plots, the logarithmic singularity lies very close to the two-body threshold cusp, producing a much narrower peak. In fact, The overall peak is located slightly to the right of the corresponding two-body threshold, due to the triangle singularity in $\sqrt{\sigma}$ lying to the right of the two-body threshold. Similarly, the Breit-Wigner-like peak is located to the right of the corresponding two-body threshold, again due to the triangle singularity in \sqrt{s} lying to the right of the two-body threshold. One can move the location of these peaks by varying the value of the invariants. But it should be noted that the invariant ranges that give rise to the triangle singularity are relatively narrow, outside of which, only the two-body thresholds are observed. The difference in the sharpness of the peak comes from the fact that K^* has a finite width in our integral, whereas K^\pm do not. One can observe a broader peak in the invariant $\sqrt{\sigma}$, by giving the K^\pm an artificial finite width. Further, the obtained Argand plot in the second case is circular, which is generally considered a signature of a resonance. And the Argand plot in the former case is deformed, due to the cusp-like behaviour arising from the stability of the kaons.

Feynman Parametrisation of the Triangle Graph

Alternatively, one can also use the textbook method of solving the loop integral through Feynman parametrisation, see Peskin & Schroeder [13]. In this method, instead of numerically integrating over the momentum, one carries out the momentum integral analytically, and reduces the equation to an integral over Feynman parameters. In our case, starting with the original integral, see equation (3.1), one may carry out a Wick's rotation of the loop momentum, giving us

$$\begin{aligned}
 I(k) &= \int \frac{d^4 q_E}{(2\pi)^4} \\
 &\quad \times \frac{1}{(q_E^2 + m_1^2 - i\varepsilon)((P_E - q_E)^2 + m_2^2 - i\varepsilon)((q_E - k_E)^2 + m_3^2 - i\varepsilon)} \quad (3.6) \\
 &= \lim_{\Lambda \rightarrow \infty} \frac{1}{(2\pi)^4} \int d\Omega \int_0^\Lambda q_E^3 dq_E \\
 &\quad \times \frac{1}{(q_E^2 + m_1^2)((P_E - q_E)^2 + m_2^2)((q_E - k_E)^2 + m_3^2)}.
 \end{aligned}$$

Here, P_E , q_E and k_E denote the wick rotated 4-momenta, that is replace q^0 with iq_E^0 , for each momentum. In the last line, we have written the 4-dimensional Euclidean integral in the (hyper-)spherical co-ordinates, with Ω being the (hyper-)solid angle, and introduced a cut-off Λ , which is later taken to ∞ , to regulate the integral. We have also dropped the $i\varepsilon$, since they all have the same sign. We will restore them if we need to determine how the poles approach the integration contour. Now, we

may introduce a Feynman parameter corresponding to each propagator, leading to

$$\begin{aligned}
 I(k) &= \lim_{\Lambda \rightarrow \infty} \frac{1}{(2\pi)^4} \int d\Omega \int_0^\Lambda q_E^3 dq_E \int_0^1 dx_1 \int_0^1 dx_2 \int_0^1 dx_3 \\
 &\quad \times \frac{\Gamma(3)\delta(1-x_1-x_2-x_3)}{[x_1(q_E^2+m_1^2)+x_2((P_E^2-q_E)^2+m_2^2)+x_3((q_E-k_E)^2+m_3^2)]^3} \\
 &= \lim_{\Lambda \rightarrow \infty} \frac{2}{(2\pi)^4} \int d\Omega \int_0^1 dx_2 \int_0^{1-x_2} dx_3 \int_0^\Lambda q_E^3 dq_E \\
 &\quad \times \frac{1}{[(q_E-(x_2 P_E + x_3 k_E))^2 + Q^2]^3}, \tag{3.7}
 \end{aligned}$$

where

$$\begin{aligned}
 Q^2 &= x_2(1-x_2)P_E^2 + x_3(1-x_3)k_E^2 - 2x_2x_3P_E \cdot k_E \\
 &\quad + m_1^2(1-x_2-x_3) + x_2m_2^2 + x_3m_3^2, \tag{3.8}
 \end{aligned}$$

is obtained by carrying out the dx_1 integral over the δ -function, and completing the square in q_E , in the denominator. Now, this is a simple rational integral over dq_E , which can be carried out easily. Making use of $\int d\Omega = 2\pi^2$ also, one gets

$$\begin{aligned}
 I(k) &= \lim_{\Lambda \rightarrow \infty} \frac{4\pi^2}{(2\pi)^4} \int_0^1 dx_2 \int_0^{1-x_2} dx_3 \left[\frac{1}{2} \left(\frac{1}{2Q^2} - \frac{2\Lambda^2 + Q^2}{2(\Lambda^2 + Q^2)^2} \right) \right] \\
 &= \frac{1}{32\pi^2} \int_0^1 dx_2 \int_0^{1-x_2} dx_3 \frac{1}{Q^2}, \tag{3.9}
 \end{aligned}$$

where, in the second line, we have carried out the limit. Also, the momenta in Q must be rotated back to Minkowski space, giving us

$$\begin{aligned}
 Q^2 &= -x_2(1-x_2)P^2 - x_3(1-x_3)k^2 + 2x_2x_3P \cdot k \\
 &\quad + m_1^2(1-x_2-x_3) + x_2m_2^2 + x_3m_3^2. \tag{3.10}
 \end{aligned}$$

We can write the above equations in terms of the invariants we are interested in:

$$\begin{aligned}
 Q^2 &= -x_2(1-x_2)s - x_3(1-x_3)m_B^2 + x_2x_3(s+m_B^2-\sigma) \\
 &\quad + m_1^2(1-x_2-x_3) + x_2m_2^2 + x_3m_3^2. \tag{3.11}
 \end{aligned}$$

Here, \sqrt{s} , $\sqrt{\sigma}$ and m_B are invariants of the particles A , B and C , respectively. Interestingly, the integral is no longer linearly divergent, unlike the result from the previous approach. This is a result of not approximating the negative energy part of the propagator out. It should be noted that the kinematical singularities in the integral, though not as obvious, are still present. These appear as endpoint or pinch singularities corresponding to the vanishing denominator in the integral over the Feynman parameters. This exactly corresponds to the singularities given by the third representation of the Landau equations discussed in the previous chapter. In comparison, the previous approach to solving the integral, corresponds to the singularities given by the first representation of the Landau equations. Since these representations are equivalent, the kinematical singularity has simply become a consequence of the vanishing of the new expression, $1/Q^2$, combined with the inability to deform the contour. Now, the integral over the Feynman parameters can be solved numerically. There is the nuance of handling the singularities in the integral.

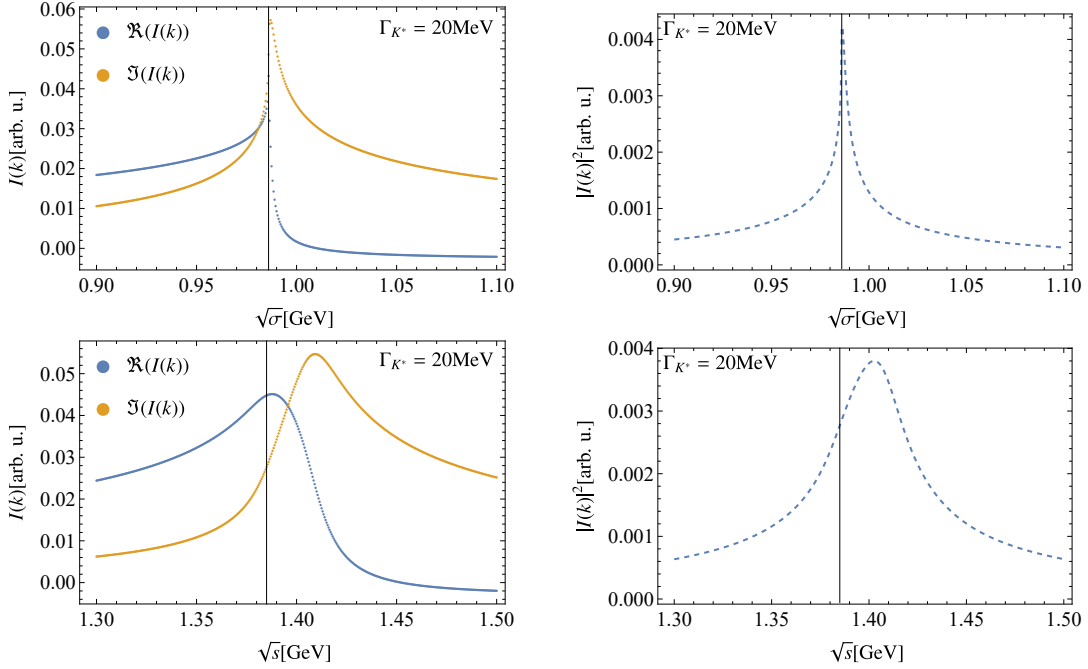


Figure 3.3: The plots on the first row show the Feynman parametrised triangle graph amplitudes evaluated as a function of $\sqrt{\sigma}$, at fixed $\sqrt{s} = 1.42$ GeV. Here, the black line denotes the two-body $m_K + m_K$ threshold. The second row has the plots evaluated as a function of \sqrt{s} , at fixed $\sqrt{\sigma} = 0.99$ GeV. Here, the black line denotes the two-body $m_{K^*} + m_K$ threshold. The first plot in each row shows the real and imaginary parts of the amplitudes. The second plot in each row shows the absolute squared of the amplitudes. All the plots are obtained with a K^* width of 20 MeV. This is in good agreement with the plots obtained through a numerical integration over the momentum, see figure 3.1. Again, the amplitudes are given in arbitrary units, since the couplings are set to unity.

We do not resort to formal integration routines, like contour deformation, which is discussed in the next chapter. For now, we make use of Gauss-Kronrod quadrature, combined with the *GlobalAdaptive* strategy of *Mathematica*, which samples more points from the neighbourhood of the singularity. The integration contour remains unchanged. One may also rewrite the integral such that all the integration measures have the same boundary points. This did not make a significant difference for the given two-dimensional integral. We discuss this in the next section. Again, the mass m_1 , of the K^* , is replaced with $m_1 - i\Gamma/2$, thus giving it a finite width. And the invariant corresponding to the particle B , is taken to be $m_B = m_\pi$. The evaluated amplitudes are given in figure 3.3, which are in good agreement with the plots in figure 3.1. It should be noted, however, that the exact values of the amplitudes do not match. And this is just a result of the two evaluated amplitudes being from two completely different integrals. The first method has the non-covariant forms of the propagators, since the negative energy solutions are approximated out. The second method perpetually accounts for covariance through the use of the covariant form of the propagators.

3.2 Kinematical Singularities in the Triangle+1 Graph

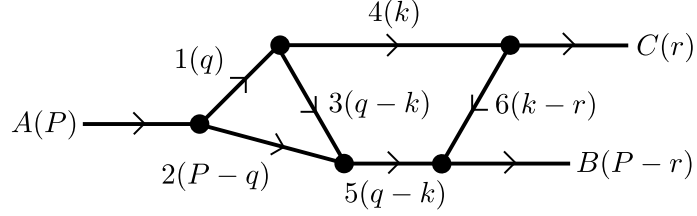


Figure 3.4: We consider a triangle+1 loop consisting of six scalar propagators, labelled as 1, 2, 3, 4, 5 and 6, with the given momenta. The external particles are given by A , B and C .

Now, one may carry out a similar analysis of the $1 + 1$ -loop graph given in figure 3.4. Since all the involved particles are scalars, the loops give rise to the integral

$$\begin{aligned}
 I(r) = & - \int \frac{d^4 q}{(2\pi)^4} \int \frac{d^4 k}{(2\pi)^4} \\
 & \times \frac{1}{(q^2 - m_1^2 + i\varepsilon)((P - q)^2 - m_2^2 + i\varepsilon)((q - k)^2 - m_3^2 + i\varepsilon)} \\
 & \times \frac{1}{(k^2 - m_4^2 + i\varepsilon)((P - k)^2 - m_5^2 + i\varepsilon)((k - r)^2 - m_6^2 + i\varepsilon)} \quad (3.12) \\
 = & - \int \frac{d^4 q}{(2\pi)^4} \frac{1}{(q^2 - m_1^2 + i\varepsilon)((P - q)^2 - m_2^2 + i\varepsilon)} \\
 & \times \int \frac{d^4 k}{(2\pi)^4} \frac{1}{((q - k)^2 - m_3^2 + i\varepsilon)(k^2 - m_4^2 + i\varepsilon)} \\
 & \times \frac{1}{((P - k)^2 - m_5^2 + i\varepsilon)((k - r)^2 - m_6^2 + i\varepsilon)}.
 \end{aligned}$$

Now, one may first solve the integral over k , call it $I_1(r; k)$, using Feynman parametrisation, in a similar fashion to that of the triangle loop integral. This gives us

$$I_1(r; k) = \frac{-i}{16\pi^2} \int_0^1 dx_2 \int_0^{1-x_2} dx_3 \int_0^{1-x_2-x_3} dx_4 \frac{1}{Q^4}, \quad (3.13)$$

where

$$\begin{aligned}
 Q^2 = & x_2(1 - x_2)q_E^2 - 2x_2q_E \cdot (x_3P_E + x_4r_E) \\
 & + x_3(1 - x_3)P_E^2 + x_4(1 - x_4)r_E^2 - 2x_3x_4P_E \cdot r_E \\
 & + m_4^2(1 - x_2 - x_3 - x_4) + x_2m_3^2 + x_3m_5^2 + x_4m_6^2. \quad (3.14)
 \end{aligned}$$

The overall integral, then, is given by

$$\begin{aligned}
 I(r) = & i \int \frac{d^4 q_E}{(2\pi)^4} \frac{1}{(q_E^2 + m_1^2)((P_E - q_E)^2 + m_2^2)} I_1(r; q) \\
 = & \frac{1}{16\pi^2} \int_0^1 dx_2 \int_0^{1-x_2} dx_3 \int_0^{1-x_2-x_3} dx_4 \\
 & \times \int \frac{d^4 q_E}{(2\pi)^4} \frac{1}{(q_E^2 + m_1^2)((P_E - q_E)^2 + m_2^2)Q^4}. \quad (3.15)
 \end{aligned}$$

Now, one may solve the integral over q , call it $I_2(r)$, using Feynman parametrisation. This gives us

$$I_2(r) = \frac{1}{16\pi^2} \int_0^1 dy_2 \int_0^{1-y_2} dy_3 \frac{y_3}{(1 - y_3 + y_3 x_2(1 - x_2))^4} \frac{1}{R^4}. \quad (3.16)$$

With this, the overall integral reduces to

$$\begin{aligned} I(s, \sigma) &= \frac{1}{16\pi^2} \frac{1}{16\pi^2} \int_0^1 dx_2 \int_0^{1-x_2} dx_3 \int_0^{1-x_2-x_3} dx_4 \\ &\times \int_0^1 dy_2 \int_0^{1-y_2} dy_3 \frac{y_3}{(1 - y_3 + y_3 x_2(1 - x_2))^4} \frac{1}{R^4}. \end{aligned} \quad (3.17)$$

R^2 can be rotated back to Minkowski space, and written in terms of the invariants we are interested in. With this, we get

$$\begin{aligned} R^2 &= \frac{1}{(1 - y_3 + y_3 x_2(1 - x_2))^2} [(y_2^2 + y_3^2 x_2^2 (x_3 + x_4)^2 + 2y_2 y_3 x_2 (x_3 + x_4))s \\ &- (y_3^2 x_2^2 (x_3 + x_4)x_4 + y_2 y_3 x_2 x_4)(s + m_B^2 - \sigma) + y_3^2 x_2^2 x_4^2 m_B^2] \\ &+ \frac{1}{(1 - y_3 + y_3 x_2(1 - x_2))} [-y_2 s + y_2 m_2^2 + (1 - y_2 - y_3)m_1^2 + y_3 Q_2^2], \end{aligned} \quad (3.18)$$

with

$$\begin{aligned} Q_2^2 &= (x_3 + x_4)(x_3 + x_4 - 1)s - x_4(1 - x_4)m_B^2 \\ &+ (x_4(1 - x_4) - x_3 x_4)(s + m_B^2 - \sigma) \\ &+ m_4^2(1 - x_2 - x_3 - x_4) + x_2 m_3^2 + x_3 m_5^2 + x_4 m_6^2. \end{aligned} \quad (3.19)$$

One may also consider the following change of variables in the Feynman parameters:

$$\begin{aligned} x'_2 &= x_2, \\ x'_3 &= x_3/(1 - x_2), \\ x'_4 &= x_4/(1 - x_2 - x_3), \\ y'_2 &= y_2, \\ y'_3 &= y_3/(1 - y_2), \end{aligned} \quad (3.20)$$

with a Jacobian of transformation:

$$|J| = (1 - x'_2)^2 (1 - x'_3) (1 - y'_2). \quad (3.21)$$

This lets one write the overall integral as integrals of Feynman parameters over the same range, giving us

$$\begin{aligned} I(s, \sigma) &= \frac{1}{256\pi^4} \int_0^1 dx'_2 \int_0^1 dx'_3 \int_0^1 dx'_4 \int_0^1 dy'_2 \int_0^1 dy'_3 \\ &\times \frac{(1 - x'_2)^2 (1 - x'_3) (1 - y'_2)^2 y'_3}{(1 - y'_3 (1 - y'_2) (1 - x'_2 (1 - x'_3)))^4} \frac{1}{R[x'_2, x'_3, x'_4, y'_2, y'_3]^4}. \end{aligned} \quad (3.22)$$

There are a few subtle manipulations involved in the calculations done above. The generalised Feynman parametrisation is discussed in appendix C. This integral can now be solved numerically. We, again, make use of Gauss-Kronrod quadrature,

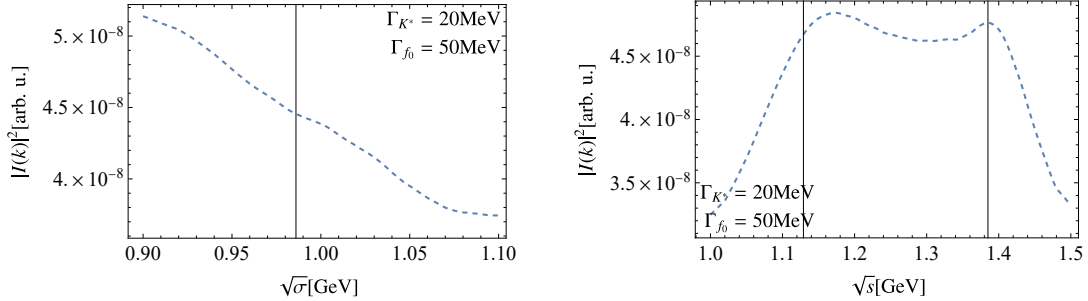


Figure 3.5: The first plot shows the Feynman parametrised triangle+1 graph amplitudes evaluated as a function of $\sqrt{\sigma}$, at fixed $\sqrt{s} = 1.4$ GeV. Here, the black line denotes the two-body $m_K + m_K$ threshold. The second plot shows the amplitudes evaluated as a function of \sqrt{s} , at fixed $\sqrt{\sigma} = 0.99$ GeV. Here, the first black line denotes the two-body $m_{f_0} + m_\pi$ threshold, whereas the second black line denotes the two-body $m_{K^*} + m_K$ threshold. All the plots are obtained with a K^* width of 20 MeV, and an f_0 width of 50 MeV. The triangle singularity is absent in both the plots. The first plot does not have the two-body $m_K + m_K$ singularity, since the two-body threshold is now located at $m_\pi + m_\pi$. However, the second plot still has the two-body $m_{K^*} + m_K$ singularity, which is smoothed due to the finite width of K^* . The second plot also has the two-body $m_{f_0} + m_\pi$ singularity, which is also smoothed due to the finite width of f_0 .

along with the *GlobalAdaptive* strategy. Still, the five-dimensional integral at hand is numerically intensive. And the values evaluated either as a function of $\sqrt{\sigma}$ for a fixed \sqrt{s} , or as a function of \sqrt{s} for a fixed $\sqrt{\sigma}$, contain random noise, which is a result of numerical instability. This is taken care of by crudely averaging the value at every point, over 10 points to the left and right of it. This should eliminate the noise, since the noise from numerical instability is random. However, one should be careful not to destroy any inherent features of the evaluated amplitude. This is taken care of by making the sampling space of $\sqrt{\sigma}$ or \sqrt{s} , as fine as possible. In our case, we considered a sampling width of 2 MeV. Again, the mass m_1 , of the K^* , is replaced with $m_1 - i\Gamma/2$, thus giving it a finite width. Also, the first three internal propagators are the same as the one from the triangle graph. The three internal propagators from the next loop are taken to be $m_4 = m_6 = m_\pi$ and $m_5 = m_{f_0}$. The invariant corresponding to the external particle B is taken as $m_B = m_\pi$, and the other two invariants are denoted by $m_A = \sqrt{s}$ and $m_C = \sqrt{\sigma}$. The evaluated amplitudes are given in figure 3.5.

One should, again, relate this to our expectations from the previous chapter. The triangle singularities are completely absent, as expected. To recall, for the triangle+1 graph with an incoming invariant, $\sqrt{s} = 1.408$ GeV, the triangle singularity was calculated to be at $\sqrt{\sigma} = 0.527$ GeV, which is far from the region of the outgoing invariant we are interested in. The two-body singularity in the outgoing invariant is also absent. It can be inferred directly from the diagram that this singularity must lie at the two-body $m_\pi + m_\pi$ threshold, which is, again, far from the region of the outgoing invariant we are interested in. However, the two-body singularity in the incoming invariant is still present at the two-body $m_{K^*} + m_K$ threshold. It should be noted that although we expect this two-body singularity to be a square root branch point, it is not so in this case. The reason being the finite width of the K^*

propagator, which smoothens out the expected cusp. Additionally, we can also see that another two-body singularity is present at the two-body $m_{f_0} + m_\pi$ threshold. We recall that this is a subleading singularity of the full triangle+1 graph. Again, this is also smoothed due to the finite width of f_0 .

To summarise, we set out to explicitly study how triangle singularities manifest in a given system. To that end, we evaluated the amplitudes corresponding to triangle and triangle+1 graphs, in a model with all scalar propagators. The masses of the propagators correspond to the respective physical masses. However, there are a couple of things to address. In the analyses so far, we considered all scalar particles with relative 0 angular momentum, and set all the couplings to 1. But this is far from the physical system, since the source — the $a_1(1260)$, is a pseudovector. This can be accommodated more easily than it seems, and this is discussed in the context of three-body unitary formalism in appendix D. Further, the dynamics of the kinematical singularities are encoded in the denominator of the integral in question, which is not going to get affected by such modifications. Therefore, the physical implication of the Landau equations should be clear at this point. The (leading) kinematical singularities correspond to all the intermediate particles going on-shell. In the case of the initial state being at rest, this corresponds to the intermediate particles flying back to back, and rescattering off each other after a second decay, whilst moving forward in time. This is the Coleman-Norton theorem [37]. However, one should still consider the question of how multiple rescattering affects this situation. This is the question we are more interested in, which is discussed in the next chapter. This method also parametrises the unstable intermediate propagators in a much more meaningful manner.

Chapter 4

Three-Body Unitary Formalism

A consistent and mathematically rigorous treatment of singularities is a hard problem. Its full solution can be given by means of a Fredholm-type integral equation. However, one can guess the structure of principal singularities with the help of heuristic arguments based on a conjecture describing the character of the point spectrum of energy operator of subsystems.

L.D. Faddeev & S.P. Merkuriev, p.56,
Quantum Scattering Theory for Several Particle Systems [47]

This chapter discusses the crucial part of this thesis, which is studying the triangle singularities through the (infinite volume) three-body unitary formalism. In the previous chapters, the singularities were calculated at tree level, and did not include full-unitarity effects. And not all the intermediate particles are stable, as modelled in the previous works. To account for this, an arbitrary width was given to the masses of the intermediate states. Though tree level calculations are well-motivated due to the reasons discussed in the previous chapter, it still does not give the full picture. We present a different approach, which takes unitarity and the instability of the intermediate particles into account. This also requires us to expand the system to include a different channel, as we will see. It is also manifestly Lorentz covariant. The formalism employed in our study is due to Mai et al. [48], which is a generalisation of Aaron et al. [49] (refer to Aaron [50] for a review). In the original work, the amplitude is constructed by matching Bethe-Salpeter terms to the terms obtained through unitarity. However, it is valid only for the bound-state particle scattering, and fails at energies above threshold. The newer model develops on the same approach, and is valid at all energies. This model has been used extensively in the recent past, for example, studies of the $a_1(1260)$ by Sadasivan et al. [51, 52], and study of the ϕ^4 -theory by Garofalo et al. [53]. We borrow heavily from these works in our study. This chapter is organised as follows. We first review the infinite volume unitarity model, including all the ingredients that go into it. Then we discuss our implementation of this model to the $a_1(1420)$ system.

4.1 The Infinite Volume Three-Body Unitary Formalism

In principle, three-body scattering calculations involve taking into account all possible interactions — when all particles interact; different cases corresponding to when two of the particles interact, while the third one does not interact; and when none of the particles interact. Isobar formulation due to Mai et al. [48], which is at the heart of the model, gives an elegant solution to this problem. An *isobar* is essentially a two-body subsystem, denoted by solid double lines in a Feynman diagram. Mathematically, it represents the on-shell two-body scattering amplitude of the subsystem. The third particle that is not a part of the isobar system, is called the *spectator*. The isobar and spectator systems may interact through one particle exchange. The model also includes a *contact term*, to take into account when all particles interact. The case when no particles interact is implicit. It should also be noted that the isobar system need not be resonant, as the diagram may suggest.

4.1.1 The Isobar-Spectator Model & Unitarity

Consider the scattering of three identical, asymptotically stable, spinless, isoscalar particles with mass m . We should address that in the case of the $a_1(1420)$ system, we do not have identical particles. But this can be accommodated for easily. Suppose this system is in an initial state $|p_1, p_2, p_3\rangle$, and a final state $\langle q_1, q_2, q_3|$, then the isobar-spectator assumption is that the three-body scattering amplitude is populated only through a spectator and an isobar that decays into two particles. The isobar completely encodes the dynamics of the two-body subchannel. With this assumption, one can calculate the three-body amplitude, and it is common to expand this amplitude in partial waves. For low enough energies, contributions from higher order partial waves are negligible, and the amplitude can be written as a sum of finite partial waves. It may also be the case that the three-particle system is generated through a source with definite quantum numbers, in which case the amplitude needs to be expanded in partial waves in a meaningful way.

The full 3-body scattering amplitude in the isobar-spectator model is decomposed into a connected amplitude and disconnected amplitude. This is given in figure 4.1. Here, \hat{T} denotes the full three-body amplitude, whereas T denotes the amputated spectator-isobar amplitude. The isobar propagator is denoted by “+”, and the vertex factor is denoted by g , which includes the coupling constant, form factors, momentum dependence, etc. The first term in the right-hand side is then the connected amplitude, \hat{T}_c , and the second term is the disconnected amplitude, \hat{T}_d . The amputated isobar-spectator amplitude term needs to be determined by matching a Bethe-Salpeter ansatz to the unitarity relation. Mathematically, this decomposition can be written as

$$\langle q_1, q_2, q_3 | \hat{T}(s) | p_1, p_2, p_3 \rangle = \langle q_1, q_2, q_3 | \hat{T}_c(s) | p_1, p_2, p_3 \rangle + \langle q_1, q_2, q_3 | \hat{T}_d(s) | p_1, p_2, p_3 \rangle. \quad (4.1)$$

For the connected amplitude, one may label it using the spectator momentum, i.e., $\langle q_1 | T | p_1 \rangle$, where p_1 and q_1 are the initial and final spectator momenta. For a general vertex factor, it is reasonable to take it as a function of the momenta of the particles making up or breaking up from the isobar, i.e., $g \equiv g(q_2, q_3)$, where q_2 and q_3 are

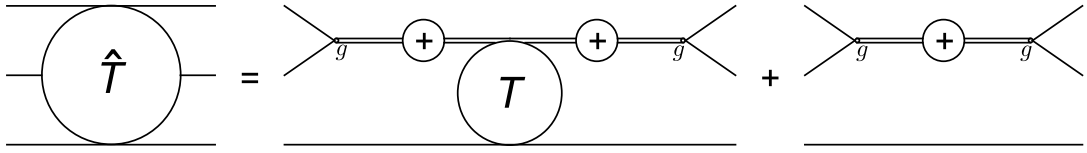


Figure 4.1: Diagrammatic representation of the isobar-spectator formalism. The full three-body scattering amplitude, \hat{T} is decomposed into connected amplitude, T_c and disconnected amplitude, T_d . The connected amplitude contains the amputated spectator-isobar amplitude, T . Also, the isobar is denoted by “+”, and the vertex factor is denoted by g . Figure partially attributed to Mai et al. [48].

the momenta of the particles coupled to the isobar. Further, we may also take the vertex factor to be symmetric under the exchange of these two particles. This amounts to not missing an additional factor of 2 when counting the different possible interactions contributing to the connected amplitude. Therefore, one may write the connected amplitude as

$$\langle q_1, q_2, q_3 | \hat{T}_c(s) | p_1, p_2, p_3 \rangle = \frac{1}{3!} \sum_{n=1}^3 \sum_{m=1}^3 \tilde{g}(q_{\bar{n}}, q_{\bar{n}}) \tau(\sigma(q_n)) \langle q_n | T | p_m \rangle \tau(\sigma(p_m)) \tilde{g}(p_{\bar{m}}, p_{\bar{m}}), \quad (4.2)$$

where \bar{n} and $\bar{\bar{n}}$ are different indices from the set $\{1, 2, 3\}$, which are also different from the value of n in that particular term. And same goes for the non-barred and barred indices m . \tilde{g} is the redefined vertex factor, to account for the symmetry under particle exchange, i.e., $\tilde{g} := 2g$. τ is the isobar propagator, and $\sigma(q_n)$ is the isobar invariant mass given by $(P - q_n)^2$, where P is the overall 4-momentum of the three-body system and q_n is the spectator 4-momentum. It should be noted that we get 9 terms in total from the above equation. Also, in the original work by Mai et al. [48], the isobar propagator is denoted by S and the the redefined vertex factor is defined by v . No confusion should arise in this regard. For the disconnected amplitude, we first assume the normalisation condition:

$$\langle q_n | p_m \rangle = 2E_{\mathbf{q}_n} (2\pi)^3 \delta^{(3)}(\mathbf{q}_n - \mathbf{p}_m), \quad (4.3)$$

where, $E_{\mathbf{q}} = \sqrt{\mathbf{q}^2 + m^2}$. Since the external particles are on-shell, we get

$$\langle q_1, q_2, q_3 | \hat{T}_d(s) | p_1, p_2, p_3 \rangle = \frac{1}{3!} \sum_{n=1}^3 \sum_{m=1}^3 (2\pi)^3 \delta^{(3)}(\mathbf{q}_n - \mathbf{p}_m) \tilde{g}(q_{\bar{n}}, q_{\bar{n}}) \tau(\sigma(q_n)) \tilde{g}(p_{\bar{m}}, p_{\bar{m}}). \quad (4.4)$$

Recalling that the unitarity of the S -matrix demands that $S^\dagger S = \mathbb{1}$, which implies $\hat{T} - \hat{T}^\dagger = i(2\pi)^4 \delta^{(4)}(p_i - p_f) \hat{T}^\dagger \hat{T}$, in operator form. The operator S and T are related through, $S := \mathbb{1} + i(2\pi)^4 \delta^{(4)}(p_i - p_f) \hat{T}$. In the context of the isobar-spectator model, we obtain

$$\begin{aligned} \langle q_1, q_2, q_3 | (\hat{T} - \hat{T}^\dagger) | p_1, p_2, p_3 \rangle &= i \int \prod_{l=1}^3 \left[\frac{d^4 k_l}{(2\pi)^4} (2\pi) \delta^+(k_l^2 - m^2) \right] \\ &\quad (2\pi)^4 \delta^{(4)} \left(P - \sum_{l=1}^3 k_l \right) \langle q_1, q_2, q_3 | \hat{T}^\dagger | k_1, k_2, k_3 \rangle \langle k_1, k_2, k_3 | \hat{T} | p_1, p_2, p_3 \rangle, \end{aligned} \quad (4.5)$$

where a complete set of states has been inserted on the right-hand side of the equation. In the original work by Aaron et al. [49], the unitarity condition was enforced on the isobar-spectator amplitude (T , in our notation). However, in the latter work by Mai et al. [48], which lies at the foundation of this study, the unitarity condition is enforced on the transitions of asymptotically stable particles. Still, the presence of $\delta^+(k_l^2 - m^2) := \delta(k_l^2 - m^2)\theta(k_l^0)$, forces the intermediate states to be on-shell with positive energy. The next step is to utilise the isobar-spectator assumption, see equation (4.1), and rewrite the unitarity condition in terms of the connected and disconnected amplitudes. At first sight, we may think that we will get 4 combinations of the amplitudes on the right-hand side of the unitarity equation — $\hat{T}_c^\dagger \hat{T}_c$, $\hat{T}_c^\dagger \hat{T}_d$, $\hat{T}_d^\dagger \hat{T}_c$ and $\hat{T}_d^\dagger \hat{T}_d$. But we have to realise that the incoming and outgoing spectators might be different. This relates to a particle exchange between the isobar and the spectator in the combinations considered. To make things clear, consider the $\hat{T}_d^\dagger \hat{T}_c$ term:

$$\begin{aligned} \langle q_1, q_2, q_3 | \hat{T}_d^\dagger | k_1, k_2, k_3 \rangle \langle k_1, k_2, k_3 | \hat{T}_c | p_1, p_2, p_3 \rangle = \\ \frac{1}{3!} \sum_{q,k} \tilde{g}(q_2, q_3) \tau^\dagger(\sigma(q_1)) \tilde{g}(k_2, k_3) 2E_{\mathbf{q}_1} (2\pi)^3 \delta^{(3)}(\mathbf{q}_1 - \mathbf{k}_1) \\ \times \frac{1}{3!} \sum_{k',p} \tilde{g}(k'_2, k'_3) \tau(\sigma(k'_1)) \langle k'_1, k'_2, k'_3 | T | p_1, p_2, p_3 \rangle \tau(\sigma(p_1)) \tilde{g}(p_2, p_3) \\ \times [\delta_{k_1, k'_1} + (1 - \delta_{k_1, k'_1})]. \end{aligned} \quad (4.6)$$

The sum here runs over the three possible spectator momenta, with appropriate vertex factors. We have inserted a couple of (discrete) δ -functions, coloured red, to take into account that the internal states can have either the same spectator or different spectators. In figure 4.3, (1a) corresponds to the term with δ_{p_1, q_1} and (3a) corresponds to the term with $(1 - \delta_{p_1, q_1})$. Also, it should be noted that the Hermitian conjugate of the isobar propagator, τ^\dagger , is denoted by a “—” in the figure. Following this, we should get 8 combinations of the amplitudes. However, one of them corresponds to the fully disconnected term, and encodes two-body unitarity. The remaining 7 combinations are given in 4.3, and identified here:

- (i) $\hat{T}_c^\dagger \hat{T}_c$: Diagrams (4a) and (4b).
- (ii) $\hat{T}_c^\dagger \hat{T}_d$: Diagrams (1b) and (3b).
- (iii) $\hat{T}_d^\dagger \hat{T}_c$: Diagrams (1a) and (3a).
- (iv) $\hat{T}_d^\dagger \hat{T}_d$: Diagram (2) (the fully disconnected term is not given).

Finally, it should be noted that only the term $\hat{T}_c^\dagger \hat{T}_c$, which corresponds to diagrams (4a) and (4b), is present in the original work by Aaron et al. [49].

4.1.2 The Bethe-Salpeter Ansatz

To determine the isobar-spectator amplitude T , we need to make an ansatz. To see this clearly, we first note that the isobar-spectator decomposition can be written

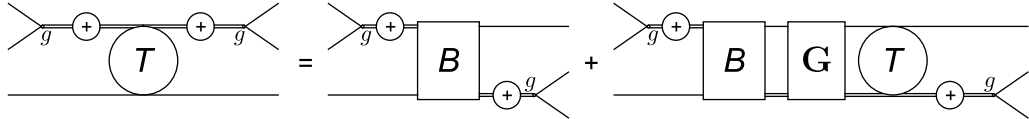


Figure 4.2: Diagrammatic representation of the Bethe-Salpeter ansatz. B denotes the interaction kernel of the Bethe-Salpeter equation, and G denotes the isobar-spectator propagator, both of which need to be determined. Figure partially attributed to Mai et al. [48].

as $\hat{T} = \hat{T}_c + \hat{T}_d = \tilde{g}\tau T\tau\tilde{g} + \tilde{g}\tau\tilde{g}$, in operator form. Then, the discontinuity can be written as

$$\begin{aligned} \hat{T} - \hat{T}^\dagger &= \tilde{g}(\tau - \tau^\dagger)\tilde{g} + \tilde{g}\tau T\tau\tilde{g} - \tilde{g}\tau^\dagger T^\dagger\tau^\dagger\tilde{g} \\ &= \tilde{g}(\tau - \tau^\dagger)\tilde{g} + (\tilde{g}\tau - \tilde{g}\tau^\dagger)T\tau\tilde{g} + \tilde{g}\tau^\dagger T^\dagger(\tau\tilde{g} - T^\dagger\tilde{g}) + \tilde{g}\tau^\dagger(T - T^\dagger)\tau\tilde{g}. \end{aligned} \quad (4.7)$$

In the second equality of equation (4.7), the first term corresponds to the fully disconnected term; the second term corresponds to the diagram (1a) in figure 4.3; the third term corresponds to the diagram (1b) in figure 4.3. To understand the last term, we need to make an ansatz. The relativistic formulation of the Lippmann-Schwinger equation, called the *Bethe-Salpeter* equation, gives a recursive relation for T :

$$\langle q|T(s)|p\rangle = \langle q|B(s)|p\rangle + \int \frac{d^4k}{(2\pi)^4} \langle q|B(s)|k\rangle G(k, \sigma(k)) \langle k|T(s)|p\rangle. \quad (4.8)$$

Here, B is the Bethe-Salpeter interaction kernel, and G is the isobar-spectator propagator, both of which need to be determined. In operator form, the above equation takes a simpler form — $T = B + BGT = B + TGB$, and a diagrammatic representation of this ansatz is given in figure 4.2. With this, one can determine the discontinuity $T - T^\dagger$ in the equation (4.7). We first note that the operator form of the Bethe-Salpeter ansatz can be inverted, which gives

$$B = T(1 + GT)^{-1}. \quad (4.9)$$

This can be used to calculate the discontinuity in B :

$$B - B^\dagger = T(1 + GT)^{-1} - (1 + T^\dagger G^\dagger)^{-1}T^\dagger. \quad (4.10)$$

The above equation can be rewritten in the following form:

$$(1 + T^\dagger G^\dagger)(B - B^\dagger)(1 + GT) = (1 + T^\dagger G^\dagger)T - T^\dagger(1 + GT). \quad (4.11)$$

This equation can be manipulated to give us the discontinuity in T :

$$\begin{aligned} T - T^\dagger &= (B - B^\dagger) + (B - B^\dagger)GT + T^\dagger G^\dagger(B - B^\dagger) \\ &\quad + T^\dagger(G - G^\dagger)T + T^\dagger G^\dagger(B - B^\dagger)GT. \end{aligned} \quad (4.12)$$

Plugging in the discontinuity in T given by equation (4.12), back in the discontinuity in \hat{T} given by equation (4.7), lets us identify the terms as the remaining diagrams

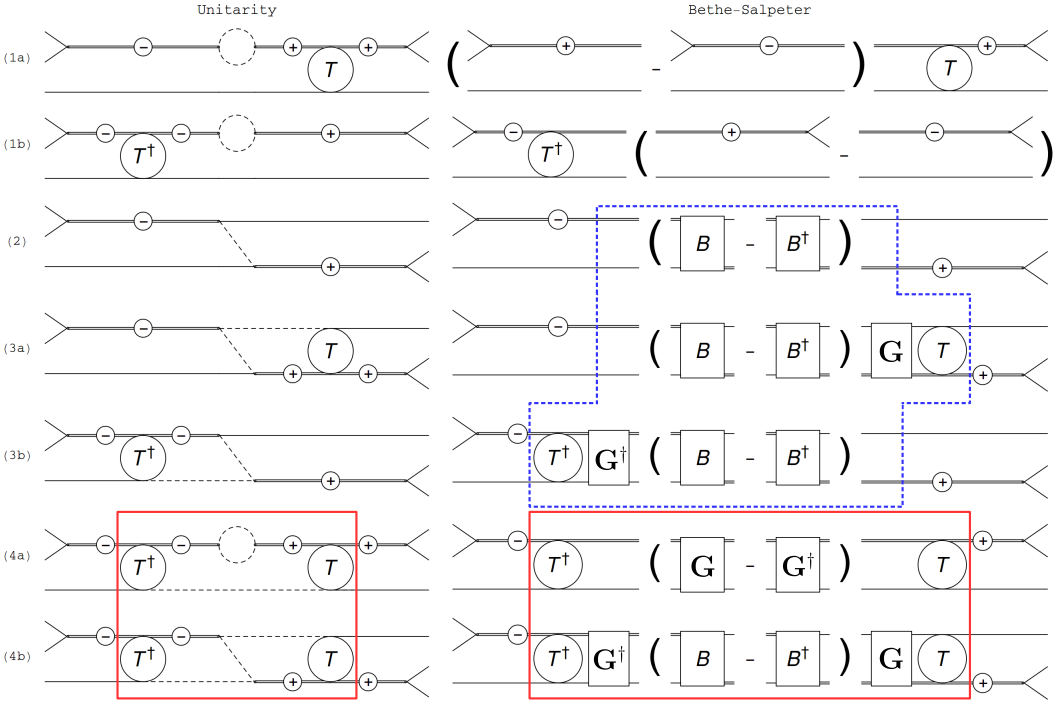


Figure 4.3: Left: Diagrammatic representation of expanding the unitarity relation in the isobar-spectator model; Right: Diagrammatic representation of expanding the unitarity relation with the Bethe-Salpeter Ansatz. Note that the vertex factors are omitted for brevity. The diagrams present in the works by Aaron et al. [49] is given inside the red box. The diagrams that arise inevitably in the isobar-spectator model, and vanish below the three-body threshold is given inside the blue dashed box. Figure partially attributed to Mai et al. [48].

in figure 4.3. In equation (4.12), the first term corresponds to the diagram (2); the second term corresponds to the diagram (1b); the third term corresponds to the diagram (3b); the fourth term corresponds to the diagram (4a); and the last term corresponds to the diagram (4b). We still need to determine explicitly the form of the Bethe-Salpeter interaction kernel B , and the isobar-spectator propagator G . And also the isobar propagator τ , which is a part of the full three-body amplitude.

4.1.3 Unitarity Matching and the Scattering Equation

Now that we have identified the terms arising from our ansatz to the terms arising from the unitarity of the isobar-spectator model, see figure 4.3, we should provide the explicit matching relations. We should also verify that these relations are consistent with all the contributing terms. The matching relations can then be used to determine the forms of B , G and τ . We can derive the discontinuities in terms of these quantities. If we identify $G(k, \sigma(k)) \equiv (2\pi)\delta^+(k^2 - m^2) \tau(\sigma(k))$, which has the effect of enforcing spectator on-shellness, the discontinuity in the isobar propagator

is given by

$$\begin{aligned} \tau(\sigma(k)) - \tau^\dagger(\sigma(k)) &= \frac{i}{2} \tau(\sigma(k)) \tau^\dagger(\sigma(k)) \\ &\times \int \frac{d^4 l}{(2\pi)^4} (2\pi) \delta^+(l_+^2 - m^2) (2\pi) \delta^+(l_-^2 - m^2) \tilde{g}^2(l_+, l_-), \end{aligned} \quad (4.13)$$

where l_\pm is the 4-momentum given by $l_\pm = (P - k)/2 \pm l$. Instead, if we consider the discontinuity in the inverse isobar propagator, which can be obtained from equation (4.13), then

$$\begin{aligned} \text{Disc}(\tau^{-1}(\sigma(k))) &\equiv \tau^{-1}(\sigma(k)) - (\tau^{-1})^\dagger(\sigma(k)) \\ &= \frac{-i}{2} \int \frac{d^4 l}{(2\pi)^4} (2\pi) \delta^+(l_+^2 - m^2) (2\pi) \delta^+(l_-^2 - m^2) \tilde{g}^2(l_+, l_-). \end{aligned} \quad (4.14)$$

This can be evaluated in the centre of mass frame of the isobar, which is discussed in appendix E. For example, in the case of an S -wave isobar, $\tilde{g} = \lambda$, where λ is the coupling constant, and the discontinuity is given by

$$\text{Disc}(\tau^{-1}(\sigma(k))) = \frac{i}{16\pi} \lambda^2 \sqrt{1 - \frac{4m^2}{\sigma(k)}}. \quad (4.15)$$

Then the inverse propagator of the isobar can be reconstructed using a dispersion relation, giving us

$$\tau^{-1}(\sigma(k)) = A + B\sigma(k) + \frac{\sigma(k)^2}{\pi} \int_{4m^2}^\infty d\sigma' \frac{1}{(\sigma')^2} \frac{\Im(\tau^{-1}(\sigma'))}{(\sigma' - \sigma(k) - i\varepsilon)}. \quad (4.16)$$

Note that we have made use of Schwarz's principle [11] to write the discontinuity in terms of the imaginary part. With a suitable choice of the coefficients, this relation can be identified as the dressed inverse propagator of the isobar in the usual sense, i.e.,

$$\tau^{-1}(\sigma(k)) = \sigma(k) - m_{\text{bare}}^2 - \Sigma(\sigma(k)), \quad (4.17)$$

where Σ is the isobar self-energy. This identification is relevant, as discussed in the next subsection.

Similarly, the discontinuity in B is given by

$$\begin{aligned} \text{Disc}(B) &\equiv \langle q | (B - B^\dagger) | p \rangle = i(2\pi) \delta^+(Q^2 - m^2) \tilde{g}(Q, q) \tilde{g}(Q, p) \\ &= 2\pi i \frac{\delta(Q^0 - \sqrt{m^2 + \mathbf{Q}^2})}{2\sqrt{m^2 + \mathbf{Q}^2}} \tilde{g}(Q, q) \tilde{g}(Q, p), \end{aligned} \quad (4.18)$$

where Q is the 4-momentum transfer given by, $Q = (P - p - q)$. Note that we have ignored the negative energy term, which is eliminated when the integral over the zeroth component of the 4-momentum is carried out. We can reconstruct B using a dispersion relation, giving us

$$\langle q | B | p \rangle = -\frac{1}{2\sqrt{m^2 + \mathbf{Q}^2}} \frac{\tilde{g}(Q, q) \tilde{g}(Q, p)}{(Q^0 - \sqrt{m^2 + \mathbf{Q}^2} + i\varepsilon)}. \quad (4.19)$$

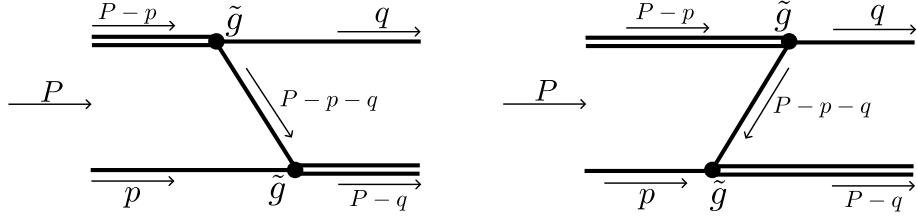


Figure 4.4: Diagrammatic representation of the B -term, see equation (4.19). The imaginary part of the second diagram is zero, and can be added to the first diagram without affecting the discontinuity. This addition makes the overall term in equation (4.19) Lorentz covariant. Note that time runs from left to right.

It should be noted that adding any real analytic function to equation (4.19) is not going to affect the discontinuity in B given by equation (4.18). For example, we can add the negative energy term that was ignored, which gives

$$\begin{aligned} \langle q|B|p\rangle &= -\frac{1}{2\sqrt{m^2 + \mathbf{Q}^2}} \frac{\tilde{g}(Q, q)\tilde{g}(Q, p)}{(Q^0 - \sqrt{m^2 + \mathbf{Q}^2} + i\varepsilon)} \\ &\quad + \frac{1}{2\sqrt{m^2 + \mathbf{Q}^2}} \frac{\tilde{g}(Q, q)\tilde{g}(Q, p)}{(Q^0 + \sqrt{m^2 + \mathbf{Q}^2} - i\varepsilon)} \\ &= \frac{\tilde{g}(Q, q)\tilde{g}(Q, p)}{m^2 - Q^2 - i\varepsilon}. \end{aligned} \quad (4.20)$$

This form has the advantage that it is Lorentz covariant. We call this term the exchange term in our analysis, for obvious reasons. With this, the Bethe-Salpeter ansatz reduces to

$$\begin{aligned} \langle q|T(s)|p\rangle &= \frac{\tilde{g}(Q, p)\tilde{g}(Q, q)}{m^2 - Q^2 - i\varepsilon} \\ &\quad - \int \frac{d^3\mathbf{l}}{(2\pi)^3} \frac{1}{2\sqrt{m^2 + \mathbf{l}^2}} \frac{\tilde{g}(P - q - l, q)\tilde{g}(P - q - l, l)}{m^2 - (P - q - l)^2 - i\varepsilon} \tau(\sigma(l)) \langle l|T(s)|p\rangle. \end{aligned} \quad (4.21)$$

Note that the 4-momentum transfer in the term inside the integral is different from the first term. We have also integrated over the zeroth component of the 4-momentum, which eliminates the negative energy term due to the presence of a Heaviside θ -function. This also reduces the 4-dimensional integral to a 3-dimensional integral. We may also write the above equation in terms of the on-shell 2 \rightarrow 2 scattering amplitude T_{22} . For example, in the case of an s -wave isobar, $\tilde{g} = \lambda$, we have $T_{22} = \lambda^2\tau(\sigma)$. And if we rescale $T \rightarrow T/\lambda^2$, the Bethe-Salpeter ansatz reduces to,

$$\begin{aligned} \langle q|T(s)|p\rangle &= \left(\langle q|C(s)|p\rangle + \frac{1}{m^2 - (P - p - q)^2 - i\varepsilon} \right) \\ &\quad - \int \frac{d^3\mathbf{l}}{2\pi^3} \frac{1}{2E_l} T_{22}(\sigma(l)) \left(\langle l|C(s)|p\rangle + \frac{1}{m^2 - (P - p - l)^2 - i\varepsilon} \right) \langle l|T(s)|p\rangle, \end{aligned} \quad (4.22)$$

where, $E_l = \sqrt{\mathbf{l}^2 + m^2}$. Here, we have replaced the B -term with $C + B$. C is an unknown function that can be added to B without affecting its discontinuity. And

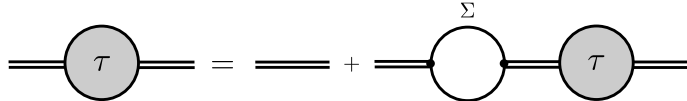


Figure 4.5: The form of the isobar considered in the present study.

the connected part of the $3 \rightarrow 3$ amplitude becomes,

$$\langle q_1, q_2, q_3 | \hat{T}_c(s) | p_1, p_2, p_3 \rangle = \frac{1}{3!} \sum_{n=1}^3 \sum_{m=1}^3 T_{22}(\sigma(q_n)) \langle q_n | T(s) | p_m \rangle T_{22}(\sigma(p_m)). \quad (4.23)$$

Studying the amputated isobar-spectator amplitude will be a crucial part of our study, since the kinematical singularity would have to occur in this component of the full three-body amplitude.

4.1.4 Isobar Propagator Parametrisation

Unitarity in the two-body subsystem is automatically ensured through three-body unitarity. This imposes a constraint on the imaginary part of the inverse of τ . In principle, we are allowed to parametrise it in such a way that is suited for the system. We mentioned in the previous subsection that τ can be expressed as the dressed isobar propagator. We, therefore, consider the following simple form for τ :

$$\tau(\sigma(p)) = \frac{1}{\sigma(p) - m_{\text{bare}}^2 - \Sigma(\sigma(p))}. \quad (4.24)$$

Here, $\sigma(p)$ is the 4-momentum invariant corresponding to the isobar, m_{bare} is the bare mass of the isobar and $\Sigma(\sigma(p))$ is the two-body self-energy. We use the term isobar propagator to mean the dressed propagator from now on. Also, we drop the \sim in the vertex factor, and express it simply as g . There should be no confusion in this regard. The bare mass can be determined through fitting the isobar propagator with the corresponding experimental phase shift data. However, one might also consider the following form of the isobar propagator:

$$\begin{aligned} \tau(\sigma(p)) &= \frac{1}{\sigma(p) - m_{\text{bare}}^2 - \Re(\Sigma(\sigma(p))) - i\Im(\Sigma(\sigma(p)))} \\ &\equiv \frac{1}{\sigma(p) - m_{\text{phys}}^2 + i\Gamma/2}. \end{aligned} \quad (4.25)$$

Here,

$$m_{\text{bare}}^2 + \Re(\Sigma(\sigma(p))) = m_{\text{phys}}^2 \quad (4.26)$$

is the physical mass of the isobar, and

$$-\Im(\Sigma(\sigma(p))) = \Gamma/2 \quad (4.27)$$

is the width of the isobar. This is not as versatile, since two experimental measurement values completely determine the isobar. However, this is very useful when experimental data is lacking. We discuss this again, later. Now, to fix the parameters, namely m_{bare} and g , we can evaluate the two-body self-energy in the rest frame of the isobar, with the two-body momentum $P = (\sqrt{\sigma}, \mathbf{0})$, and loop momentum k :

$$\Sigma(P) = -g^2 \int \frac{d^4 k}{(2\pi)^4} \frac{1}{[(P/2 + k)^2 - m_1^2 + i\varepsilon][(P/2 - k)^2 - m_2^2 + i\varepsilon]}. \quad (4.28)$$

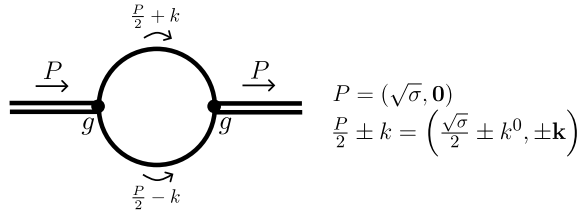


Figure 4.6: The two-body self-energy term, Σ , evaluated in the centre of mass frame of the isobar. The vertex factor, g , does not have any momentum dependence, or contain a form factor, but includes only the coupling constant. This, along with the bare mass of the isobar, is fixed using the physical mass and width of the isobar.

The isobar momentum P used in the diagram 4.6 should not be confused with the spectator momentum p . While fixing the parameters, σ is merely a variable, i.e., we do not consider the term from the spectator yet. The integration over the zeroth component of the 4-momentum can be carried out using Cauchy's integral theorem, which gives

$$\Sigma(\sigma) = g^2 \int \frac{\mathbf{k}^2 d|\mathbf{k}|}{2\pi^2} \frac{1}{2E_1 E_2} \frac{E_1 + E_2}{\sigma - (E_1 + E_2)^2 + i\varepsilon}. \quad (4.29)$$

Here, g is the vertex factor, which does not include any momentum dependence or a form factor, but consists only of the coupling constant, and $E_i = \sqrt{|\mathbf{k}|^2 + m_i^2}$. Equation (4.25) along with the integral given in equation (4.29) determines the isobar propagator τ , and is a part of the scattering amplitude equation.

4.2 Implementation to the $a_1(1420)$ System

As discussed before, the $a_1(1420)$, just like the $a_1(1260)$, is a pseudovector with quantum numbers $I^G(J^{PC}) = 1^-(1^{++})$. However, in the following analysis we consider a more rudimentary scalar system. One reason is that we are more interested in the analytic properties of the overall integral. Considering a pseudovector system would give rise to an integral, which still has logarithmic cuts in the exchange term B , but also with increased numerical complexity. Such an analysis is not novel, and has been carried out in the works mentioned before, e.g., Sadasivan et al. [51, 52]. We table such a study for the future. For now, we limit ourselves to scalar vertices. This also means that the dissociation vertex for the $a_1(1260)$ is scalar. We set the contact term C , to zero, whose form is typically determined through a fit with the phase-shift data, and the line shape data. This has the effect that it prohibits free propagation of the $a_1(1260)$ in the analysis. This is not a problem, since the observed peak is argued to be a kinematical singularity, see e.g., Mikhasenko et al. [4], which is re-examined here in parts. In principle, we do not need the dynamics of the $a_1(1260)$ to observe a kinematical singularity. The contact term also regulates the ultraviolet divergences of the integral by the means of a smooth cutoff, and setting it to zero might seem problematic. Instead, we opt for a subtracted form of the isobar propagator with a hard cutoff. We also lack the experimental phase-shift data analysis for $K^*(892)$. Therefore, instead of a fit to determine the isobar parameters, we consider fixing the parameters through the physical mass of the isobar and its width. To summarise, we have the scalar dissociation vertex for the $a_1(1260)$, D , and we have the scalar vertex factor for the isobar, g , which is fixed along with its

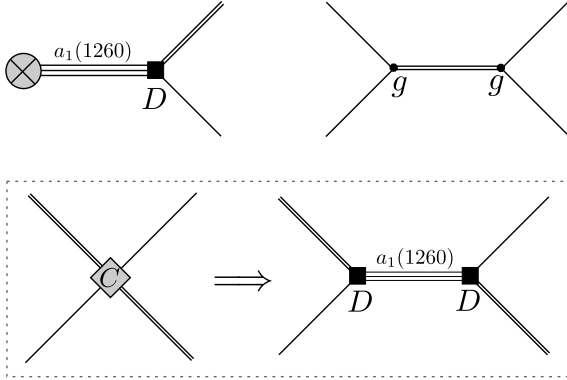


Figure 4.7: We consider a scalar source that produces the $a_1(1260)$ like resonance. This lets us construct our system using a scalar dissociation vertex D . Further, the scalar coupling constant of the isobar, g , along with its bare mass, is also determined. We set the contact term C , to zero. This means that the second term inside the dashed box is not present in our analysis. Here, three solid lines correspond to $a_1(1260)$, two solid lines correspond to an isobar and a single solid line corresponds to a spectator.

bare mass. In our case, we consider different couplings associated with the different isobars, as shown in figure 4.8. For a meaningful analysis, we need to introduce two channels, which is discussed in the next subsection. Finally, the contact term C , is set to zero.

4.2.1 Coupled Channel Analysis

Before we construct the isboars of the system, we first have to determine what possible isobars should be considered in our analysis. At the one-loop triangle level, we have $a_1(1260) \rightarrow K^*K^+K^- \rightarrow f_0\pi^-$. The kaons and the pions correspond to asymptotically stable fields, and are the spectators in our analysis. Then we have K^* and f_0 as the isobars. This already lets us consider two channels that are relevant to us — K^*K^- channel (numbered 1) and $f_0\pi^-$ channel (numbered 2). The relevant channels are given in the diagram 4.8. We note that a transition between K^*K^- channel and K^*K^- channel ($1 \rightarrow 1$ transition) is not possible, since this would violate conservation of strangeness or conservation of electric charge, depending on which propagator acts as the exchange particle. But it is possible to construct a transition between $f_0\pi$ channel and $f_0\pi$ channel ($2 \rightarrow 2$ transition). To allow cross channel transitions, i.e., transition between K^*K^- channel and $f_0\pi$ channel ($1 \rightarrow 2$ and $2 \rightarrow 1$ transition), we parametrise the f_0 propagator using a K^+K^- loop as well. This is reasonable, since the branching ratios corresponding to the kaon and pion channels are roughly equal, see Ablikim et al. [54] and Aubert et al. [55]. We discuss the construction of actual transitions in a later subsection.

4.2.2 Isobar Propagator Parameters

As discussed before, we use equations (4.25) and (4.29) to determine the isobar propagator τ . For our study, we need to construct an isobar propagator corresponding to K^* and another isobar corresponding to f_0 . To do this, we need the physical masses of the isobars and their widths. We take these values from PDG [39], as

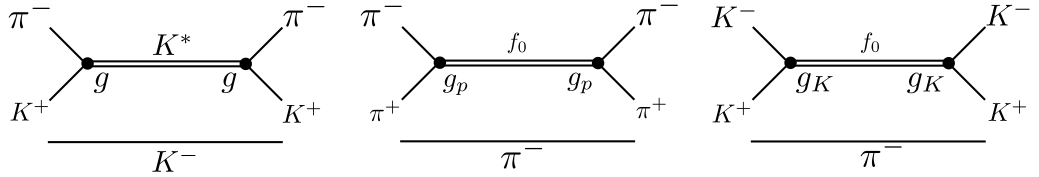


Figure 4.8: We consider two channels in our model — K^*K^- channel (numbered 1) and $f_0\pi$ channel (numbered 2). In a model with these two channels, a transition between channel 1 and channel 1 is not possible, however, a transition between channel 2 and channel 2 is possible. To allow cross channel transitions, we also parametrise the isobar using a K^+K^- loop. All vertex factors are scalar.

$m_{\text{phys}} = 0.892$ GeV for K^* , and $m_{\text{phys}} = 0.990$ GeV for f_0 . As for the width, we consider 5, 20 and 50 MeV widths for K^* , and 10, 50 and 100 MeV widths for f_0 . The different widths are considered to study the effect of the width of the isobar propagator on the amplitudes. The physical masses and the widths lets us determine the bare masses and the coupling constants of the isobar propagators. Note that the f_0 isobar is parametrised through two different couplings, hence, we need another equation to remove this degree of freedom, which is discussed shortly. We also use the twice subtracted self-energy integral to improve convergence. For the self-energy K^* , this reads:

$$\begin{aligned} \Sigma(\sigma) = & g^2 \int \frac{\mathbf{k}^2 d|\mathbf{k}|}{2\pi^2} \frac{1}{2\sqrt{\mathbf{k}^2 + m_K^2}\sqrt{\mathbf{k}^2 + m_\pi^2}} \frac{\sigma}{\left(\sqrt{\mathbf{k}^2 + m_K^2} + \sqrt{\mathbf{k}^2 + m_\pi^2}\right)^2} \\ & \times \frac{\left(\sqrt{\mathbf{k}^2 + m_K^2} + \sqrt{\mathbf{k}^2 + m_\pi^2}\right)}{\sigma - \left(\sqrt{\mathbf{k}^2 + m_K^2} + \sqrt{\mathbf{k}^2 + m_\pi^2}\right)^2}. \end{aligned} \quad (4.30)$$

Note that we have ignored the $i\varepsilon$ for reasons discussed later. For the self-energy of f_0 , we get two integrals, each corresponding to the loop in consideration:

$$\begin{aligned} \Sigma_K(\sigma) = & \frac{g_K^2}{2} \int \frac{\mathbf{k}^2 d|\mathbf{k}|}{2\pi^2} \frac{1}{2\sqrt{\mathbf{k}^2 + m_K^2}\sqrt{\mathbf{k}^2 + m_K^2}} \frac{\sigma}{\left(\sqrt{\mathbf{k}^2 + m_K^2} + \sqrt{\mathbf{k}^2 + m_K^2}\right)^2} \\ & \times \frac{\left(\sqrt{\mathbf{k}^2 + m_K^2} + \sqrt{\mathbf{k}^2 + m_K^2}\right)}{\sigma - \left(\sqrt{\mathbf{k}^2 + m_K^2} + \sqrt{\mathbf{k}^2 + m_K^2}\right)^2}, \end{aligned} \quad (4.31)$$

$$\begin{aligned} \Sigma_p(\sigma) = & \frac{g_p^2}{2} \int \frac{\mathbf{k}^2 d|\mathbf{k}|}{2\pi^2} \frac{1}{2\sqrt{\mathbf{k}^2 + m_\pi^2}\sqrt{\mathbf{k}^2 + m_\pi^2}} \frac{\sigma}{\left(\sqrt{\mathbf{k}^2 + m_\pi^2} + \sqrt{\mathbf{k}^2 + m_\pi^2}\right)^2} \\ & \times \frac{\left(\sqrt{\mathbf{k}^2 + m_\pi^2} + \sqrt{\mathbf{k}^2 + m_\pi^2}\right)}{\sigma - \left(\sqrt{\mathbf{k}^2 + m_\pi^2} + \sqrt{\mathbf{k}^2 + m_\pi^2}\right)^2}. \end{aligned} \quad (4.32)$$

Note that the self-energy term is labelled according to the coupling constant from the respective loop vertices. There is also an extra factor of $1/2$, which is just the symmetry factor associated with the loops involving identical particles. With these

self-energy integrals, the isobar propagator, τ , is given by equation (4.24). For the K^* propagator, this reads:

$$\tau_{K^*}(\sigma(p)) = \frac{1}{\sigma(p) - m_{\text{bare}}^2 - \Sigma(\sigma(p))}. \quad (4.33)$$

And for the f_0 propagator, this reads:

$$\tau_{f_0}(\sigma(p)) = \frac{1}{\sigma(p) - m_{\text{bare}}^2 - \Sigma_K(\sigma(p)) - \Sigma_p(\sigma(p))}. \quad (4.34)$$

Before we fix the parameters, we could perform a sanity check by comparing whether this form of the propagator respects unitarity. One can derive the imaginary part of the inverse isobar propagator through unitarity requirements, see appendix E. For the K^* isobar, this reads:

$$\Im(\tau_{K^*}^{-1}(\sigma)) = \frac{-g^2}{16\pi\sigma} \lambda^{1/2}(\sigma, m_K^2, m_\pi^2), \quad \sqrt{\sigma} \geq (m_K + m_\pi). \quad (4.35)$$

Similarly, for the f_0 isobar, the analytic result reads:

$$\begin{aligned} \Im(\tau_{f_0}^{-1}(\sigma)) &= \frac{-g_p^2}{32\pi\sigma} \lambda^{1/2}(\sigma, m_\pi^2, m_\pi^2) \\ &= \frac{-g_p^2}{32\pi} \sqrt{1 - \frac{4m_\pi^2}{\sigma}}, \quad 2m_\pi \leq \sqrt{\sigma} \leq 2m_K, \end{aligned} \quad (4.36)$$

$$\begin{aligned} \Im(\tau_{f_0}^{-1}(\sigma)) &= \frac{-g_p^2}{32\pi\sigma} \lambda^{1/2}(\sigma, m_\pi^2, m_\pi^2) + \frac{-g_K^2}{32\pi\sigma} \lambda^{1/2}(\sigma, m_K^2, m_K^2) \\ &= \frac{-g_p^2}{32\pi} \sqrt{1 - \frac{4m_\pi^2}{\sigma}} + \frac{-g_K^2}{32\pi} \sqrt{1 - \frac{4m_K^2}{\sigma}}, \quad \sqrt{\sigma} \geq 2m_K. \end{aligned} \quad (4.37)$$

Here, λ is the Källén triangle function defined by equation (2.54). We can now carry out the sanity check with arbitrary bare masses and coupling constants for the isobar propagators. The results are given in figure 4.9 and are in perfect agreement.

With everything in place, we determine the bare masses and the coupling constants by evaluating the self-energy integral in the centre of mass frame of the isobar. It should be noted that we have two different coupling constants in the case of the f_0 propagator. Since we have only two equations to fix the bare masses and the coupling constants, we need an additional equation. We use the ratio between g_K and g_p couplings from BES [54] and BaBar [55] collaborations, $g_K/g_p = 4.21$. The phase space available for the kaon channel is smaller than the phase space available for the pion channel. Still, the branching ratios are roughly the same, which is explained by the relatively larger coupling. Since a lack of experimental data is not a problem in the case of the f_0 propagator, in principle, the parameters can be obtained through a fit with this data. However, we do not take this route to be consistent, and take the same approach as towards the K^* propagator. The obtained isobar parameters are given in table 4.1. With this, we have completely determined the form of the isobar propagator $\tau(\sigma(p))$, defined by equation (4.24). Finally, we obtain the phase-shift plots for the determined isobar propagators. These are given in figures 4.10a and 4.10b.

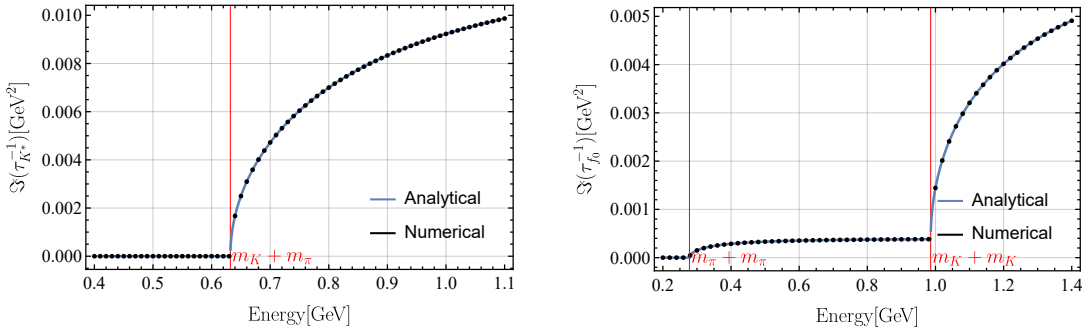


Figure 4.9: The chosen form of the isobar propagator respects unitarity. This is verified by matching the numerical and analytical values of the imaginary part of the inverse isobar propagators, which is constrained by unitarity, for arbitrary bare masses and coupling constants. The first plot shows this matching for the K^* isobar, with the red line denoting the two-body threshold, whereas the second plot shows this for the f_0 isobar, with the two red lines denoting the two different two-body thresholds.

K^* width[MeV]	5	20	50
$m_{\text{bare}}(K^*)[\text{GeV}]$	0.892558	0.894230	0.897565
$g[\text{GeV}]$	0.440459	0.880917	1.39285
f_0 width[MeV]	10	50	100
$m_{\text{bare}}(f_0)[\text{GeV}]$	1.00048	1.04133	1.09025
$g_p[\text{GeV}]$	0.443857	0.992494	1.4036
$g_K[\text{GeV}]$	1.86864	4.1784	5.90915

Table 4.1: Isobar parameters corresponding to the K^* and the f_0 isobars.

4.2.3 Interaction Kernel Parameters

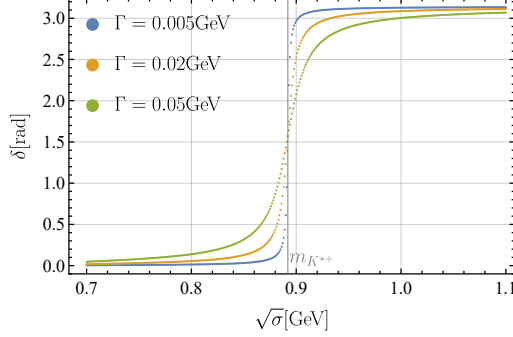
We now discuss the Bethe-Salpeter interaction kernel, or simply, the exchange terms considered in our study. We recall that the interaction kernel is given by (see equation (4.19))

$$\langle q|B|p\rangle = -\frac{1}{2\sqrt{m^2 + \mathbf{Q}^2}} \frac{g(Q, q)g(Q, p)}{(Q^0 - \sqrt{m^2 + \mathbf{Q}^2} + i\varepsilon)}, \quad (4.38)$$

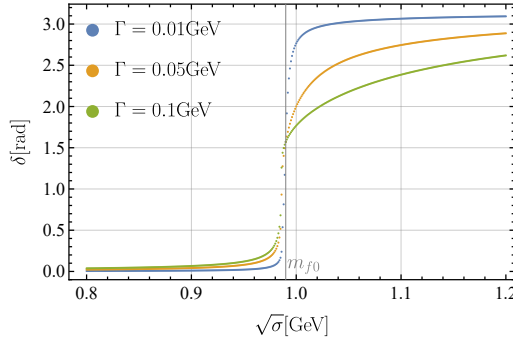
where $Q = (P - p - q)$. In our study, $g(Q, q) = g(Q, p) = g$, and writing the exchange term in terms of different masses of the participating particles, we get

$$B(\mathbf{p}, \mathbf{q}) = -\frac{1}{2\sqrt{m_{ex}^2 + \mathbf{p}^2 + \mathbf{q}^2 + 2|\mathbf{p}||\mathbf{q}|\cos\theta}} \times \frac{g^2}{\sqrt{s} - \sqrt{\mathbf{p}^2 + m_1^2} - \sqrt{\mathbf{q}^2 + m_2^2} - \sqrt{m_{ex}^2 + \mathbf{p}^2 + \mathbf{q}^2 + 2|\mathbf{p}||\mathbf{q}|\cos\theta}}. \quad (4.39)$$

In the above equation, we have used — m_{ex} for the mass of the exchanged particle; m_1 for the mass for the mass of incoming spectator; m_2 for the mass of the outgoing spectator. This generalisation is necessary, since we do not have identical interacting particles. However, this generalisation poses no problem for the assumed ansatz for the isobar-spectator amplitude. We also assumed that we are working in the centre



(a) Phase shift plot for the K^* propagator with the obtained isobar parameters. The plot is obtained for three different widths. The physical mass of K^* is set at 0.892 GeV



(b) Phase shift plots for the f_0 propagator with the obtained isobar parameters. The plot is obtained for three different widths. The physical mass of f_0 is set at 0.99 GeV.

Figure 4.10: Phase shift plots for the propagators.

of mass frame of the initial state, which gives $Q = (\sqrt{s} - E_p - E_q, \mathbf{p} + \mathbf{q})$, and since the spectators go on-shell, we can use the relevant on-shell relations for E_p and E_q . And \sqrt{s} is the three-body total energy. Lastly, $\cos \theta$, which will sometimes be denoted by z , is the planar angle between the incoming and the outgoing spectator momentum. A rather implicit thing that is overlooked here is the angular momentum projection of the exchange term. We recall that we are working in a system with s -wave isobars and relative s -wave between the spectator and the isobar, also leading to a scalar vertex. In this case, the projection coefficients are scalar too. However, when this is not the case, we need to be careful, and either absorb the projection coefficients in the vertex factors, or explicitly include them in the definition of the exchange term. We discuss more on this in a later subsection, and mostly in appendix D. With this, we get three possible exchange terms in our model, corresponding to transitions within and between the defined channels. A $1 \rightarrow 1$ channel transition is not present. The other transitions are given by

$$B_{12} = \frac{-1}{2E_{m_K}(\mathbf{p} + \mathbf{q})} \frac{g g_K}{(\sqrt{s} - E_{m_K}(\mathbf{p}) - E_{m_\pi}(\mathbf{q}) - E_{m_K}(\mathbf{p} + \mathbf{q}))}, \quad (4.40)$$

$$B_{21} = \frac{-1}{2E_{m_K}(\mathbf{p} + \mathbf{q})} \frac{g_K g}{(\sqrt{s} - E_{m_\pi}(\mathbf{p}) - E_{m_K}(\mathbf{q}) - E_{m_K}(\mathbf{p} + \mathbf{q}))}, \quad (4.41)$$

$$B_{22} = \frac{-1}{2E_{m_\pi}(\mathbf{p} + \mathbf{q})} \frac{g_p g_p}{(\sqrt{s} - E_{m_\pi}(\mathbf{p}) - E_{m_\pi}(\mathbf{q}) - E_{m_\pi}(\mathbf{p} + \mathbf{q}))}, \quad (4.42)$$

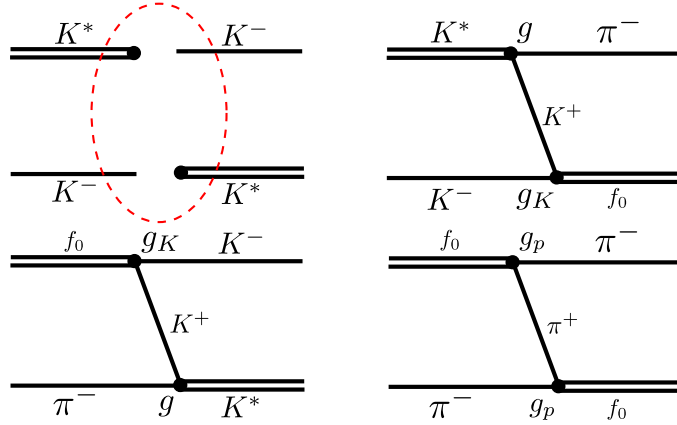


Figure 4.11: Possible exchanges in the coupled channel analysis considered in the study, with their corresponding couplings. There is no $1 \rightarrow 1$ transition in the model, but all the other transitions are present.

where, $E_m(p) = \sqrt{m^2 + \mathbf{p}^2}$, taken with the relevant masses. The diagrammatic representations of the exchange terms are given in figure 4.11. With everything in hand, the next step is to solve for the isobar-spectator amplitude, using the Bethe-Salpeter ansatz. The exact details are discussed in the next subsection.

4.2.4 Numerical Implementation (Method0)

The crucial part of this study is to solve the equation for the non-trivial isobar-spectator amplitude, T , which for our system is given by

$$T(\sqrt{s}, \mathbf{q}; \mathbf{p}) = B(\sqrt{s}, \mathbf{q}; \mathbf{p}) + \int \frac{d^3 l}{(2\pi)^3} \frac{1}{2E_l} B(\sqrt{s}, \mathbf{q}; \mathbf{p}) \tau(\sigma(l)) T(\sqrt{s}, \mathbf{q}; \mathbf{p}). \quad (4.43)$$

Here, \sqrt{s} is the total incoming energy of the system in the centre of mass frame, \mathbf{q} is the outgoing spectator momentum, \mathbf{p} is the momentum of the first spectator, that is integrated over. We have a three-dimensional integral in the second term, and an angular-dependent term in the exchange term B . This integral is too complicated to solve directly, particularly for the general case when the vertex factors are momentum-dependent too. But this is not the case in our model. The standard solution strategy is to expand the amplitude in partial waves, and solve for each partial wave individually. The amplitudes are first projected on to the helicity basis, from which the relevant partial wave can be extracted using Wigner- d functions [56]. This is then transformed to the JLS basis, in which the partial wave amplitudes with the relative angular momenta can be calculated. Here, J stands for the total angular momentum of the system, e.g., the isobar-spectator system; L stands for the relative angular momentum, and S stands for the total intrinsic angular momentum of the constituent particles, e.g., the isobar and the spectator. This is then transformed back to the helicity basis, using Wigner- D functions [56]. Since we assume that our source has zero total angular momentum, and the particles that make up the isobar-spectator system also have 0 total angular momentum, and the vertex factors are spherically symmetric (scalars), we need to consider only the S -wave partial amplitude. This reduces the problem at hand significantly, in terms of computational

complexity. This amounts to introducing an overall normalisation factor of $1/4\pi$ to the exchange terms, which disappears when the angular integral is carried out. However, a more general analysis has been carried out before, e.g., Sadasivan et al. [51, 52]. We discuss this approach in appendix G. Therefore, the isobar-spectator amplitude for our purposes reads:

$$\begin{aligned} T_{00}(\sqrt{s}, \mathbf{q}; \mathbf{p}) = & B_{00}(\sqrt{s}, \mathbf{q}; \mathbf{p}) \\ & + \int \frac{\mathbf{l}^2 d\mathbf{l}}{2\pi^2} \frac{1}{2E_l} B_{00}(\sqrt{s}, \mathbf{q}; \mathbf{p}) \tau(\sigma(l)) T_{00}(\sqrt{s}, \mathbf{q}; \mathbf{p}), \end{aligned} \quad (4.44)$$

where 00 labels the helicities. We will drop the helicity indices, since it can take only one set of values, and it is apparent. The angular integration can be carried out either analytically, or numerically with an integration routine such as Gaussian quadrature, which is discussed later. In the following analysis, we analytically integrate this term first, and then use it in our spectator-isobar amplitude equation. There is not much difference between using the analytical form the angular integral of the B -term and using a numerical integration routine, aside the obvious computational advantage. However, for higher partial wave-projections and vertex factors with momentum dependencies, numerical integration becomes a necessity. The form of B after carrying out the angular integral is given by

$$B(\sqrt{s}, \mathbf{q}; \mathbf{p}) = \frac{1}{4|\mathbf{p}||\mathbf{q}|} \log \left(\frac{\sqrt{s} - \sqrt{\mathbf{p}^2 + m_1^2} - \sqrt{\mathbf{q}^2 + m_2^2} - \sqrt{(|\mathbf{p}| + |\mathbf{q}|)^2 + m_{ex}^2}}{\sqrt{s} - \sqrt{\mathbf{p}^2 + m_1^2} - \sqrt{\mathbf{q}^2 + m_2^2} - \sqrt{(|\mathbf{p}| - |\mathbf{q}|)^2 + m_{ex}^2}} \right). \quad (4.45)$$

The overall integral is still not straightforward, since the exchange term can have poles on the integration contour, which is just the positive real axis. In fact, the singularity structure of the projected B -term is non-trivial — depending on the value of the outgoing momentum q , we may either have a logarithmic cut that is not too complicated to accommodate, or we may have a logarithmic cut that is non-trivial and requires evaluating the integral cleverly. The exact singularity structure of the exchange term is discussed in the next section. For now, we use the method of contour deformation here, as originally implemented by Hetherington & Schick [57]. We retrospectively call this method the “Method0” or “M0”, in the context of discussing other possible numerical implementations of this integral.

First, since we are solving this integral numerically, we first discretise this equation, giving us

$$T_{pq} = B_{pq} + \sum_l B_{pl} \tilde{\tau}_l T_{lq}. \quad (4.46)$$

Here, the indices p , q and l label the discrete momenta. Also, $\tilde{\tau}$ denotes that we include the additional factors of $\mathbf{l}^2/(2\pi^2)$ and $1/(2E_l)$ in τ . It can be seen straight away that this can be formulated as a matrix equation, with matrices whose dimensions equal the number of discrete momentum points. We sample all three discrete momenta from the same space. Hence, we get a square matrix. But we also have to include both channels. This results in solving a matrix equation, with matrices whose dimensions are twice the number of discrete momentum points. That is, the relevant terms are constructed as block matrices:

$$\left(\begin{array}{c|c} 0 & B_{12} \\ \hline B_{21} & B_{22} \end{array} \right), \quad \left(\begin{array}{c|c} \tilde{\tau}_{K^*} & 0 \\ \hline 0 & \tilde{\tau}_{f_0} \end{array} \right), \quad (4.47)$$

which were defined previously, see equations (4.40), (4.41), (4.42), and equations (4.33), (4.35). From here on, we use B and $\tilde{\tau}$ to mean the block matrices. The next obvious step is to invert the matrix equation to solve for T :

$$T_{pq} = \sum_l ([\mathbb{1} - B\tilde{\tau}]_{pl}^{-1} B_{lq}). \quad (4.48)$$

We now just have to evaluate the values of the terms on the right-hand side of the above equation, at the discrete momentum points. However, this is not trivial, since the terms might be singular for some momentum points. As suggested by the name of this approach, we *deform* the integration contour to avoid the singularities. In other words, we let the loop spectator momentum take complex values. This automatically forces the outgoing spectator momentum and/or the incoming three-body energy to take complex values, as well. If we explicitly set the incoming three-body energy to take only real values, then only the loop spectator momentum, and the outgoing spectator momentum are complex. Equivalently, one picks an integration contour for which the singularities in the integration variable do not hit the contour, for all outgoing momenta sampled from the same contour. The choice of the contour is a matter of taste. We choose the following parametrisation of the contour:

$$f_{SMC}(t) = t + ia(1 - e^{-t/b})(1 - e^{(t-\Lambda)/b}), \quad t \in [0, \Lambda]. \quad (4.49)$$

This contour is called the *spectator momentum contour* or the *SMC*. Here, a and b are some chosen real numbers, and t is the contour parameter. This contour enforces a hard cut-off, Λ , similar to Garofalo et al. [53], unlike Sadasivan et al., [51, 52]. We encounter singularities, when either E_{l+q} vanishes, or $(\sqrt{s} - E_l - E_q - E_{l+q})$ vanishes, see equation (4.39). The singularities in the integration momentum for outgoing momenta evaluated for points in the SMC are given in figure 4.12. We should also note that there is another integral, which is not apparent so far. This is the self-energy integral present in the definition of the propagator, τ . We evaluate this integral along a different contour, the *Spectator Energy Contour* or the *SEC*:

$$f_{SEC}(t) = t + ia \tan^{-1}(bt), \quad t \in [0, \pi/2]. \quad (4.50)$$

Here, a and b are some chosen real numbers, not necessarily the same as the ones chosen for SMC, and t is the contour parameter. This contour does not enforce any cut-off, but rather is limited by the number of sampling points. We should be careful not to have any singularities here, as well. We encounter problems only when $\sigma(p)$ equals $\sqrt{\mathbf{k}^2 + m_1^2} + \sqrt{\mathbf{k}^2 + m_2^2}$, see equations (4.30), (4.31) and (4.32). The singularities of the self-energy integral are given in figure 4.13.

Now, the relevant terms can be evaluated at the points on the deformed contour and solved for T . We carry out the discrete integration using Gaussian quadrature. This numerical integration method is discussed in appendix F. But briefly, in Gaussian quadrature, the integral is reduced to a sum, with the integrand being evaluated at discrete points within the integration range, with each evaluation point multiplied by an appropriate Gaussian quadrature weight. These weights are absorbed into our definition of $\tilde{\tau}$. As for the specifics of the integration routine, we discretise the SMC and the SEC into 75 roughly equally placed points. To note, Gaussian quadrature sampling points are not equally spaced, and we achieve this by a transformation. The SMC parameters are $\{a, b\} = \{-0.1 \text{ GeV}, 0.1 \text{ GeV}\}$, and the

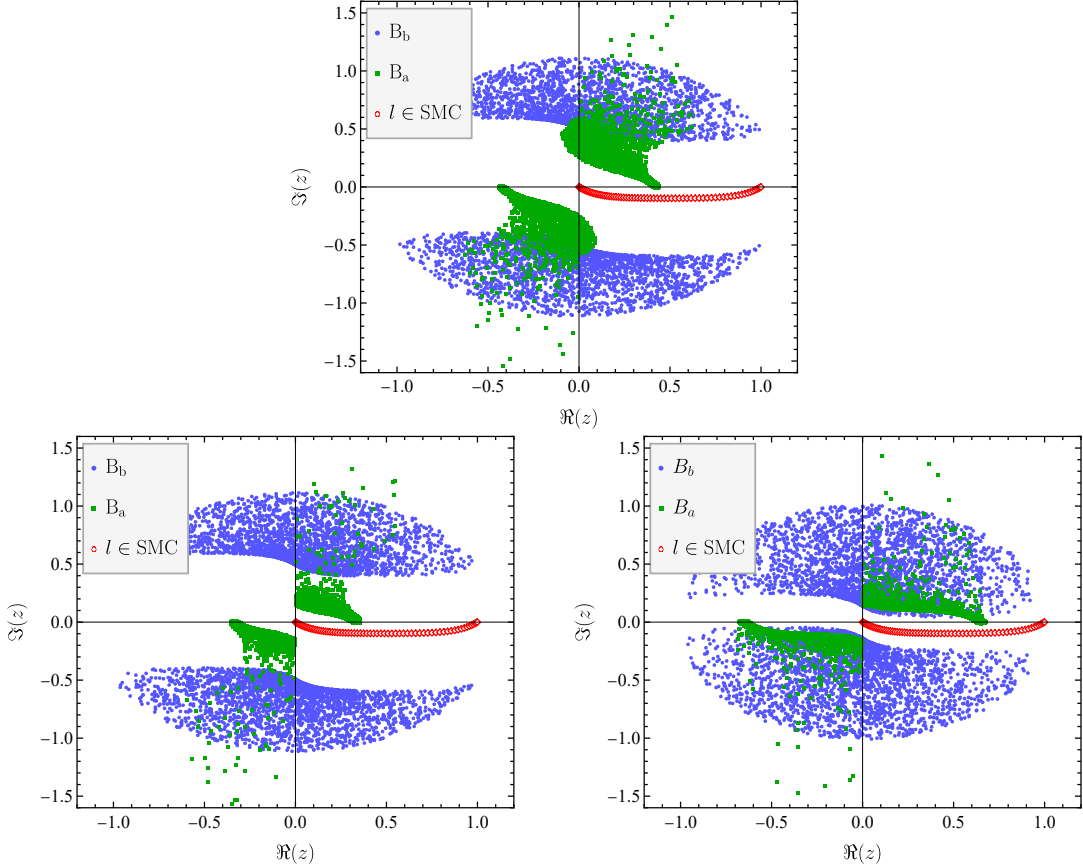


Figure 4.12: The singularities in the integration variable of the B -term, for outgoing spectator momentum points evaluated along SMC. The first plot is for the $1 \rightarrow 2$ channel, the second plot is for the $2 \rightarrow 1$ channel, and the third plot is for the $2 \rightarrow 2$ channel. It should be noted that the B -term, see equation (4.39), is a product of two terms in the denominator. B_a (green) are the points for which E_{l+q} vanishes, whereas B_b (blue) are the points for which $(\sqrt{s} - E_l - E_q - E_{l+q})$ vanishes. Lastly, red points denote the integration contour. The plots are evaluated for $\sqrt{s} = 1.42$ GeV, and the shape parameters are $\{a, b\} = \{-0.1 \text{ GeV}, 0.1 \text{ GeV}\}$ (see equation (4.49)).

SEC parameters are $\{a, b\} = \{-1 \text{ GeV}, 1.2 \text{ GeV}^{-1}\}$. The cut-off is set at 1 GeV. The connected spectator-isobar amplitude, T is then obtained, which is a function $T \equiv T(\sqrt{s}, \mathbf{q}; \mathbf{p})$. Now, in our system, the first spectator is not external, so it must be integrated over appropriately. This amounts to multiplying T with $D\tilde{\tau}(\sigma(p))$ from the left, for p evaluated at the points in SMC. Recall that D is the $a_1(1260)$ scalar dissociation vertex, and we set it to 1, for our present purposes. The integral is just a sum over p , since all the relevant weights are already in $\tilde{\tau}$. With this we get a semi-connected three-body amplitude, \hat{T}_c^1 . We call this the semi-connected three-body amplitude, since to obtain the full amplitude, we need to multiply this with $g\tau(\sigma(q))$ on the right, for q evaluated at the points in SMC, along with other additional factors, and g is the relevant isobar vertex factor. We discuss this later, along with calculating the disconnected three-body amplitude, \hat{T}_d . For now, we concentrate on the semi-connected three-body amplitude, \hat{T}_c^1 .

The job is only half done so far, since we have calculated, $\hat{T}_c^1(\sqrt{s}, \mathbf{q})$ for real \sqrt{s} and complex $|\mathbf{q}|$. The momenta $|\mathbf{q}|$ are observables, and they have to be real. To find the values for real $|\mathbf{q}|$, one may construct a Padé approximant in $|\mathbf{q}|$, fit it for the

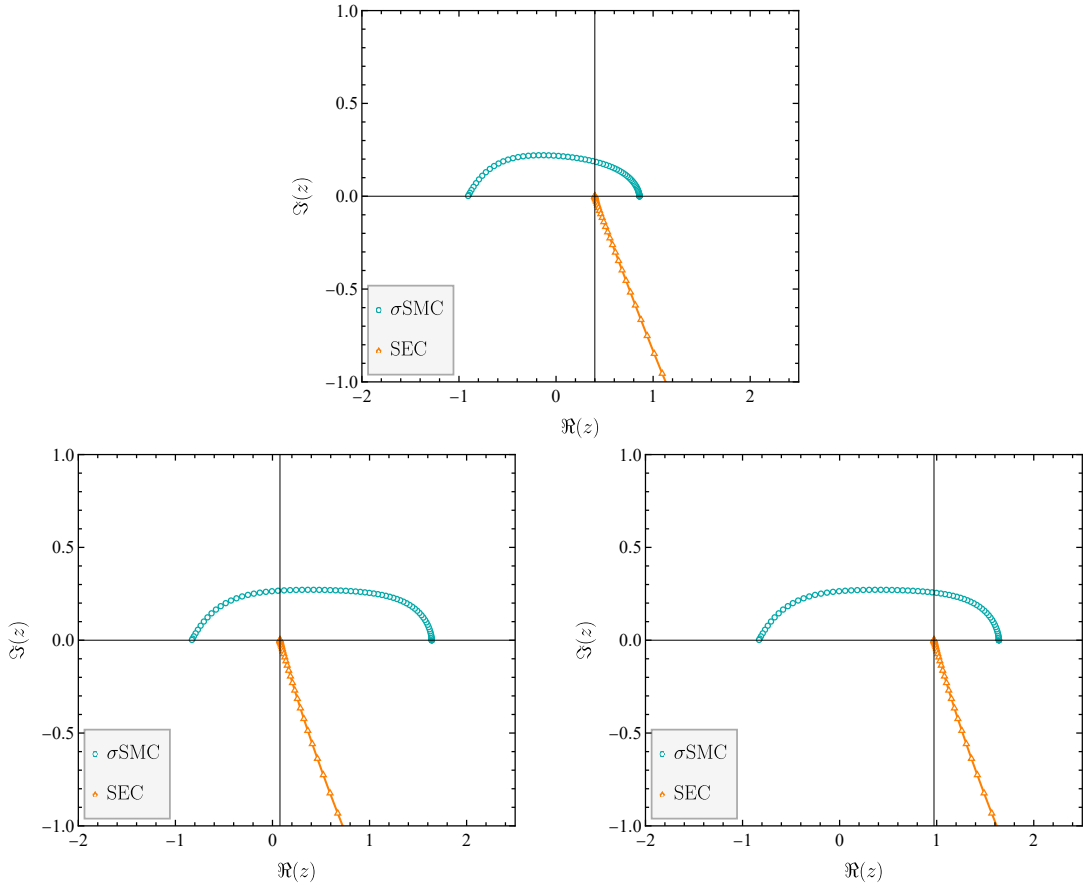


Figure 4.13: The singularities of the self-energy integral. The aqua points denote $\sigma(l)$ evaluated for points in the SMC. And the orange points denote $(\sqrt{\mathbf{k}^2 + m_1^2} + \sqrt{\mathbf{k}^2 + m_2^2})^2$, evaluated for the self-energy loop momentum k . We encounter singularities in the self-energy integral, when these terms are equal, see equations (4.30), (4.31) and (4.32). The plots are evaluated for $\sqrt{s} = 1.42$ GeV, and the shape parameters are $\{a, b\} = \{-1 \text{ GeV}, 1.2 \text{ GeV}^{-1}\}$ (see equation (4.50)).

obtained complex values, and extrapolate it to values on the real axis. This is the widely preferred method to extrapolate values to the real axis. However, it should be noted that we expect a two-body cusp in the variable $|\mathbf{q}|$ for some fixed \sqrt{s} , since we have an amputated isobar to the right. In our analysis, Padé approximants that we used were unable to reproduce cusps, or any sharp feature for that matter. When calculating the final three-body amplitude, multiplying with $\tau(\sigma(q))$ to the right smoothens this cusp, posing no further issues at the full three-body amplitude level. But we would like to determine the existence of the features related to the triangle singularity. Therefore, we used generalised continued fractions to interpolate the values evaluated for complex $|\mathbf{q}|$'s and extrapolate it to real $|\mathbf{q}|$'s. Generalised continued fraction interpolation was carried out by Binosi et al. [58], in their study of the J/ψ meson recently. Generalised continued fractions are complex-valued generalisations of the real-valued continued fractions — continued fractions with complex coefficients. From now on, we use “continued fraction” to mean “generalised continued fraction”. This method can reproduce cusps, and other sharp structures. However, one must be cautious when interpolating using continued fractions, since it might give rise to a lot more spurious poles, compared to Padé approximants.

It should also be noted that continued fraction and Padé approximants are closely related, see Jones and Thron [59]. Setting aside further discussions on continued fractions and Padé approximants, we interpolate now using continued fractions, with a hint of caution.

We make use of Thiele's interpolation formula, which can be generalised to complex-valued points (refer to Abramowitz and Stegun [60]):

$$f(z) = f(z_1) + \frac{z - z_1}{\rho(z_1, z_2) + \frac{z - z_2}{\rho_2(z_1, z_2, z_3) - f(z_1) + \frac{z - z_3}{\rho_3(z_1, z_2, z_3, z_4) - \rho(z_1, z_2) + \frac{z - z_4}{\ddots + \frac{z - z_{n-1}}{\rho_{n-1}(z_1, \dots, z_n) - \rho_{n-3}(z_1, \dots, z_{n-2}) + z - z_n}}}}}. \quad (4.51)$$

Or in a more compact notation due to Pringsheim [61]:

$$f(z) = f(z_1) + \left[\frac{z - z_1}{\rho(z_1, z_2)} \right] + \left[\frac{z - z_2}{\rho_2(z_1, z_2, z_3) - f(z_1)} \right] + \left[\frac{z - z_3}{\rho_3(z_1, z_2, z_3, z_4) - \rho(z_1, z_2)} \right] + \cdots + \left[\frac{z - z_{n-1}}{\rho_{n-1}(z_1, \dots, z_n) - \rho_{n-3}(z_1, \dots, z_{n-2}) + z - z_n} \right]. \quad (4.52)$$

Here, ρ 's are the reciprocal differences, defined by

$$\begin{aligned} \rho(z_1, z_2) &= \frac{z_1 - z_2}{f(z_1) - f(z_2)} \equiv \rho_1(z_1, z_2) \\ \rho_2(z_1, z_2, z_3) &= \frac{z_1 - z_3}{\rho_1(z_1, z_2) - \rho_1(z_2, z_3)} \\ \rho_3(z_1, z_2, z_3, z_4) &= \frac{z_1 - z_4}{\rho_2(z_1, z_2, z_3) - \rho_2(z_2, z_3, z_4)} \\ \rho_{n-1}(z_1, \dots, z_n) &= \frac{z_1 - z_n}{\rho_{n-2}(z_1, \dots, z_{n-1}) - \rho_{n-2}(z_2, \dots, z_n)}. \end{aligned} \quad (4.53)$$

And the continued fraction coefficient at the m -th level is given by

$$\rho_m(z_1, \dots, z_{m+1}) - \rho_{m-2}(z_1, \dots, z_{m-1}), \quad m \in \{1, \dots, n-1\}, \quad (4.54)$$

with $\rho_{-1} = 0$, $\rho_0 = f(z_1)$, and n is the number interpolation points, which in our case is the size of the discrete momentum space. Therefore, the continued fraction used for interpolating the obtained $\hat{T}_c^1(\sqrt{s}, q \in \text{SMC})$ points has 74 levels. Once an interpolating polynomial is obtained, we can investigate the amplitude for real momenta q . At this point, we should mention what this quantity depends on. It obviously depends on the centre of mass frame energy of the incoming particle, which we call \sqrt{s} . It also depends on the magnitude of the spectator momentum, $|\mathbf{q}|$, which goes on-shell. It should be noted that we also have an (amputated) isobar, which we assign an invariant mass σ . If we take the incoming 4-momentum as $(\sqrt{s}, 0, 0, 0)$, and the outgoing 4-momenta as $(\sqrt{m_\pi^2 + \mathbf{q}^2}, 0, 0, \pm |\mathbf{q}|)$, we should be able to solve for q in terms of the other quantities using 4-momentum conservation. Then, the amplitude can be investigated by scanning this invariant mass, σ , while keeping \sqrt{s} fixed. Further, the amplitude can be investigated by scanning \sqrt{s} , while keeping σ fixed. This was what was exactly carried out in the previous chapter for non-unitary models, as well. We perform a similar analysis here to ensure consistency.

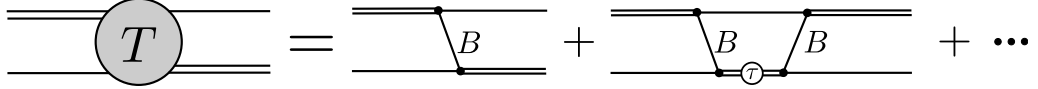


Figure 4.14: The Bethe-Salpeter ansatz to the amputated isobar-spectator amplitude represented as an iterative solution. Here, B denotes an exchange and τ denotes the isobar propagator, both of which are determined in our analysis.

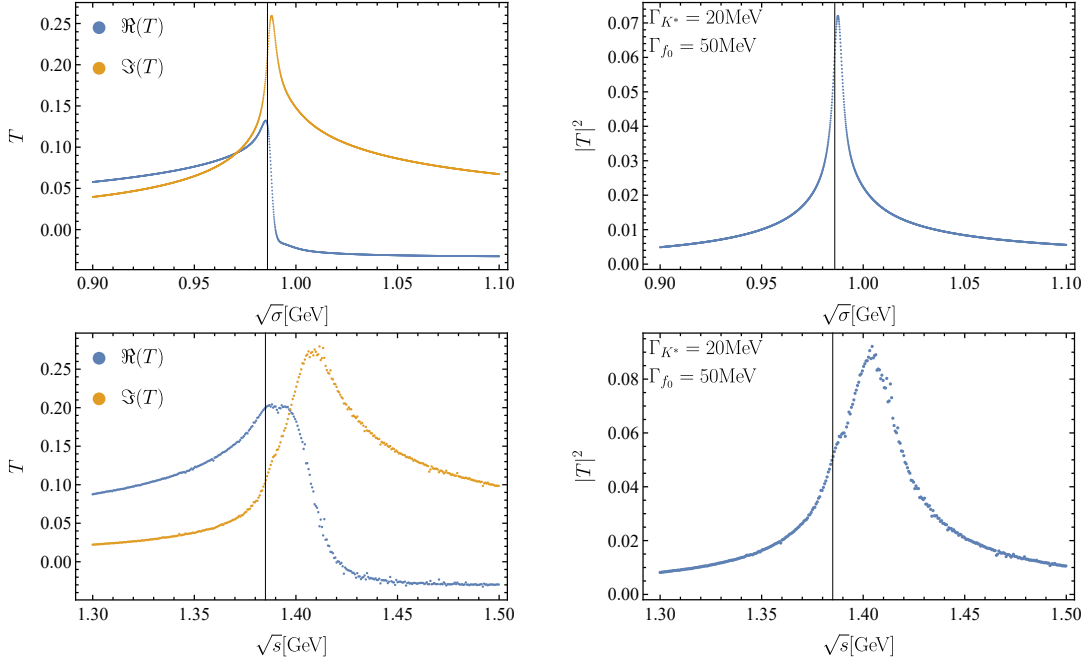


Figure 4.15: The amplitudes (channel 1 → 2) evaluated at the triangle level. The top two images show the isobar-spectator amplitudes obtained as a function of $\sqrt{\sigma}$, for fixed $\sqrt{s} = 1.42$ GeV. The bottom two images show the amplitudes obtained as a function of \sqrt{s} , for fixed $\sqrt{\sigma} = 0.99$ GeV. The first plot of each row shows the real and imaginary parts of the amplitudes, and the second plot shows the absolute squared value of the amplitudes. The black line denotes the two-body threshold — $m_K + m_K$ for the plots on the top, and $m_{K^*} + m_K$ for the plots on the bottom. The K^* width is set at 20 MeV, and the f_0 width is set at 50 MeV.

Results for the Triangle (1-loop Level)

We interpret the Bethe-Salpeter ansatz, $T = B + B\tau T$, as an iterative solution to the isobar-spectator amplitude. This means that we can diagrammatically represent the ansatz as an expansion given in figure 4.14. The amplitude at subsequent terms need not necessarily be smaller than the amplitudes at previous orders. The series need not necessarily converge, either. We re-emphasize that a careful study of divergences and renormalisation is not what we are after. Therefore, at the triangle level (or, the 1-loop level), we just have an exchange corresponding to the isobar-spectator amplitude, and the incoming isobar is integrated over, with the incoming spectator going on-shell. Hence, this amounts to integrating τB with the proper integration measure and integration factors. This integral is not as unsophisticated as it looks, due to the presence of logarithmic branch cuts. We solve by implementing the method of contour deformation. We see in figure 4.15 that the triangle singularity persists at the one-loop level in the isobar-spectator models, in good agreement

with the non-unitary model. We have evaluated the amplitudes for the K^* widths of 20 MeV, and an f_0 width of 50 MeV. This width of the K^* is relatively larger than the experimental width, and this is done on purpose to have the peaks more pronounced. Also, note that the amplitudes in the figure are only the channel 1 to channel 2 transition amplitudes. For the channel 2 to channel 2 transition, it was discussed in a previous chapter that the second channel has a triangle singularity in the \sqrt{s} region we are interested in. But it was shown that the corresponding value of σ was much smaller than the mass of the isobar. This is verified within the isobar-spectator model, and the results are given in figure H.1, in appendix H. This might look like it could affect the overall structure of the kinematical singularity in our system. But it should be noted that the quantity we have considered so far is the semi-connected amplitude. This needs to be multiplied by the proper isobar propagator on the right, when the fully connected isobar-spectator amplitude is studied. In our case, the isobar corresponds to f_0 , whose mass is taken as 0.99 GeV, with a width not greater than 50 MeV. Therefore, contributions from energies much farther from this mass are going to be suppressed, when an integration over the Lorentz invariant phase space of the outgoing momenta is carried out. This is another reason why we did not verify whether the kinematical singularities from other diagrams actually lie on the physical sheet in chapter 2, since the corresponding σ region was much farther from the mass f_0 .

Results for the House (1 + 1-loop Level)

At the 1 + 1-loop level, we have two exchanges, and diagrammatically this looks like a “box” attached to the triangle. When we studied the infinite volume unitarity of this particular three-body system, we called this the “house”, since it looks like a house from the side. By a similar logic, 1 + 2-loop level looks like a house with 2 stories, and so on. And at full unitarity level, we have infinite stories, and we called this the “Hilbert’s house”, since this resembles the hotel with infinite rooms from the Hilbert’s paradox [62]. It should be noted that the present problem is not related to the original paradox, but just a naming scheme. Mathematically, at this level, we have to integrate twice, $\tau B \tau B$, with the proper integration measure and integration factors. The first integral corresponds to the loop-momentum from the box, and the second integral corresponds to the loop-momentum from the triangle. Again, we carry this out using the method of contour deformation. We expect no kinematical singularity, neither leading nor subleading, apart from the two-body threshold, for this integral. And the obtained plots are as expected. In the first plot on the first row in figure 4.16, we see no two-body threshold cusp — we should recall that the corresponding integral can only have a $\pi\pi$ two-body threshold, which is far away from the region we are interested in. In the next plot, we see two different two-body threshold cusps, one corresponding to the $m_{f_0} + m_\pi$ threshold, and the other corresponding to the $m_{K^*} + m_K$ threshold, but no kinematical singularity. Again, this is expected from our system, since we cannot have a kinematical singularity in this energy region.

Results for the Finite Houses (1 + 2 & 1 + 3-loop Levels)

For every subsequent addition of a box (or, a storey), we introduce a new τB term which is integrated over its loop momentum. Mathematically, every subsequent

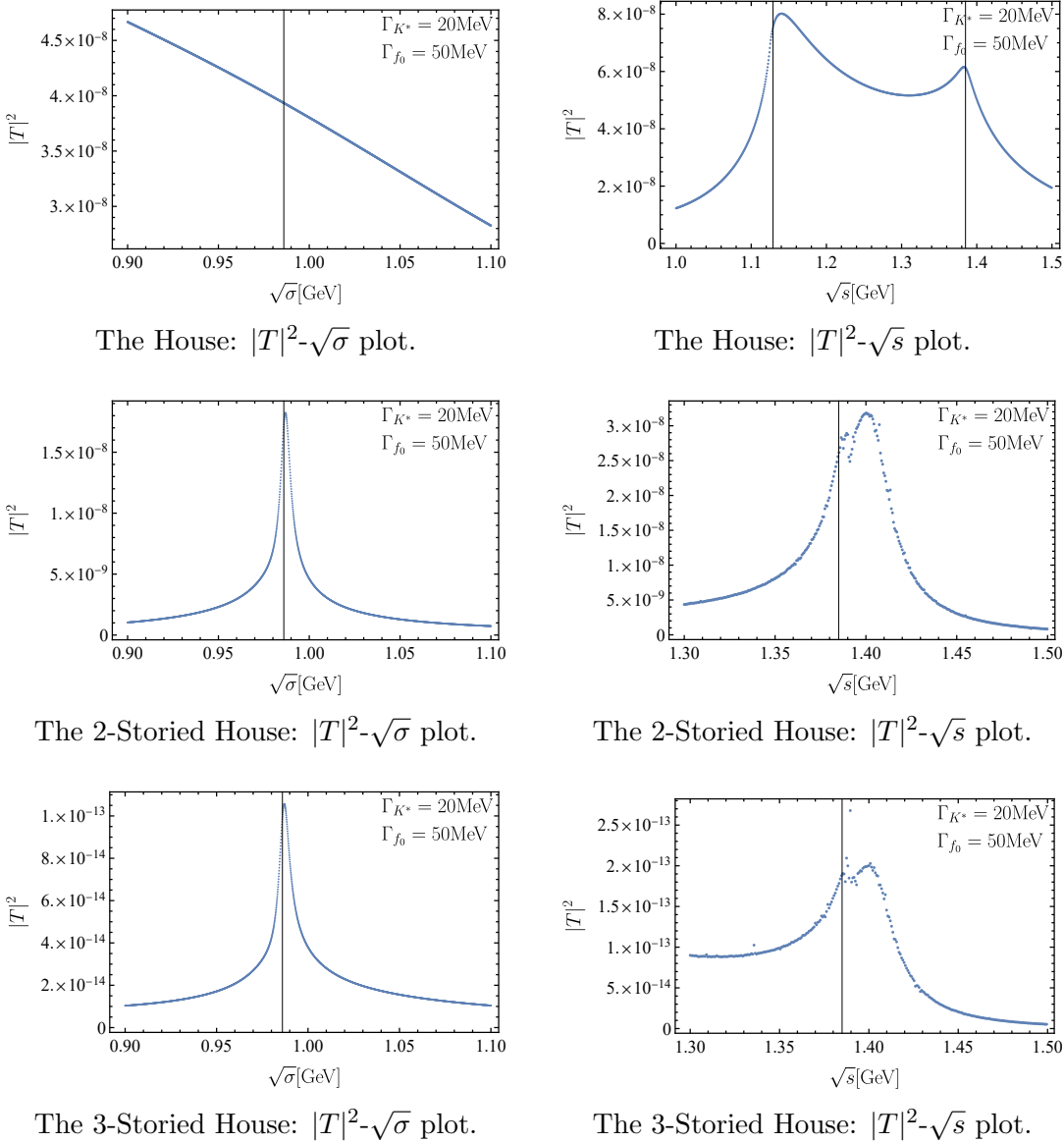


Figure 4.16: The amplitudes (channel 1 \rightarrow 2) evaluated at different levels — the triangle singularity does not exist at the 1 + 1-loop level, but exists at higher levels. The plots on the left are evaluated at fixed $\sqrt{s} = 1.42$ GeV, and the plots on the right are evaluated at fixed $\sqrt{\sigma} = 0.99$ GeV. The black line denotes the two-body threshold — $m_K + m_K$ for the plots on the left, and $m_{K^*} + m_K$ for the plot on the right. The K^* width is set at 20 MeV, and the f_0 width is set at 50 MeV. The plots with real-imaginary parts of the amplitudes can be found in appendix H.

house corresponds to solving integrals of $\tau B \tau B \dots$, with as many integrals as there are intermediate spectators. At 1 + 2-loops and beyond, we expect a $m_K + m_K$ two-body cusp, since it is possible for us to have a transition from channel 1 to channel 2 with a final exchange K^+ , interacting with a K^- spectator. This is not possible for the $1 \rightarrow 2$ transition, only at the 1-loop level. And we can see in the first plots of the second and third rows of figure 4.16, that the two-body threshold cusp is present at both two-storey and three-storey levels. Even though there is no leading kinematical singularity in the region of interest, we should recall that we expect a subleading triangle singularity at two-storeys and beyond. And again,

we can see that in the second plots of the second and third row (note the scale of the amplitudes in these figures, compared to the triangle). Also, the amplitudes in the figure are only the channel 1 to channel 2 transition amplitudes, similar to the triangle case.

We should address the irregularities in the evaluated amplitudes for the $|T|^2-\sqrt{s}$ plots, particularly for the amplitudes at higher levels. This is a numerical instability, and it is arising from the contour being very close to the poles. This is particularly visible on the $|T|^2-\sqrt{s}$ plots for two reasons: (1) The way the algorithm is implemented: we should recall that we evaluated the final amplitude as a function of the incoming three-body energy, \sqrt{s} , and the magnitude of the outgoing spectator, $|\mathbf{q}|$. We then reformulated this amplitude in terms of \sqrt{s} and $\sqrt{\sigma}$. σ is related to q through a Källén triangle function, $|\mathbf{q}| = \lambda^{1/2}(s, \sigma, m_\pi^2)/(2\sqrt{s})$. For the $|T|^2-\sqrt{\sigma}$ plots, when we fix \sqrt{s} , we obtain a set of complex valued points, that then are interpolated using a continued fraction. In other words, we obtain only one analytic function in this case. But for the $|T|^2-\sqrt{s}$ plots, when we vary \sqrt{s} , this changes the value of $|\mathbf{q}|$, as well, since we fix $\sqrt{\sigma}$. So, we obtain a different set of complex points for each value of \sqrt{s} , which are then individually interpolated using a different continued fraction. In other words, we obtain n analytic functions, where n is the number of \sqrt{s} points, in this case. This should not be a problem when every analytic function behaves nicely and forms a “family” of analytic functions that can be obtained by uniformly varying a parameter (\sqrt{s} , here); (2) There are two different closely lying non-analyticities in the interested region: a two-body threshold, which is a square root branch point, and a kinematical singularity, which here is a logarithmic singularity. Our family of analytic functions have to reproduce the behaviour of a square root branch point, like a phase shift in the imaginary component, as well as the behaviour of a logarithmic singularity. When only one of them is present, like in the case of (1 + 1)-level, our implementation does not have any issues producing the amplitudes. But things become unstable, when our family of analytic functions have to reproduce two different closely lying non-analyticities. In our case, a combination of the above-mentioned points result in irregularities. A way out of this is to make sure that we choose somewhat a different contour, whose points lie far from the poles. One may also consider an isobar propagator with a larger width, which masks these irregularities. We verified this by using the K^* propagator with a width of 50 MeV, and the irregularities reduced significantly. But also, the kinematical singularity became less pronounced, as expected. Therefore, we include the plots evaluated using the K^* propagator with a width of 20 MeV. We did not pursue investigating a different contour mainly because we can already see that the contribution from every subsequent term from the ansatz is lesser than the previous term. As we will see, the primary contribution to the triangle singularity is from the triangle (or 1-loop) level.

Results for the Hilbert’s House

We now discuss the solutions at the full-unitarity level. It should be noted that, so far, we explicitly carried out the loop-momentum integrals at different levels of the finite houses. However, at full-unitarity level, one needs to solve it through a matrix inversion, and then integrate over the incoming spectator momentum, with the appropriate integration measure and integration factors. In figure 4.17, we can see the persistence of the triangle singularity at the full unitarity level. Here, the

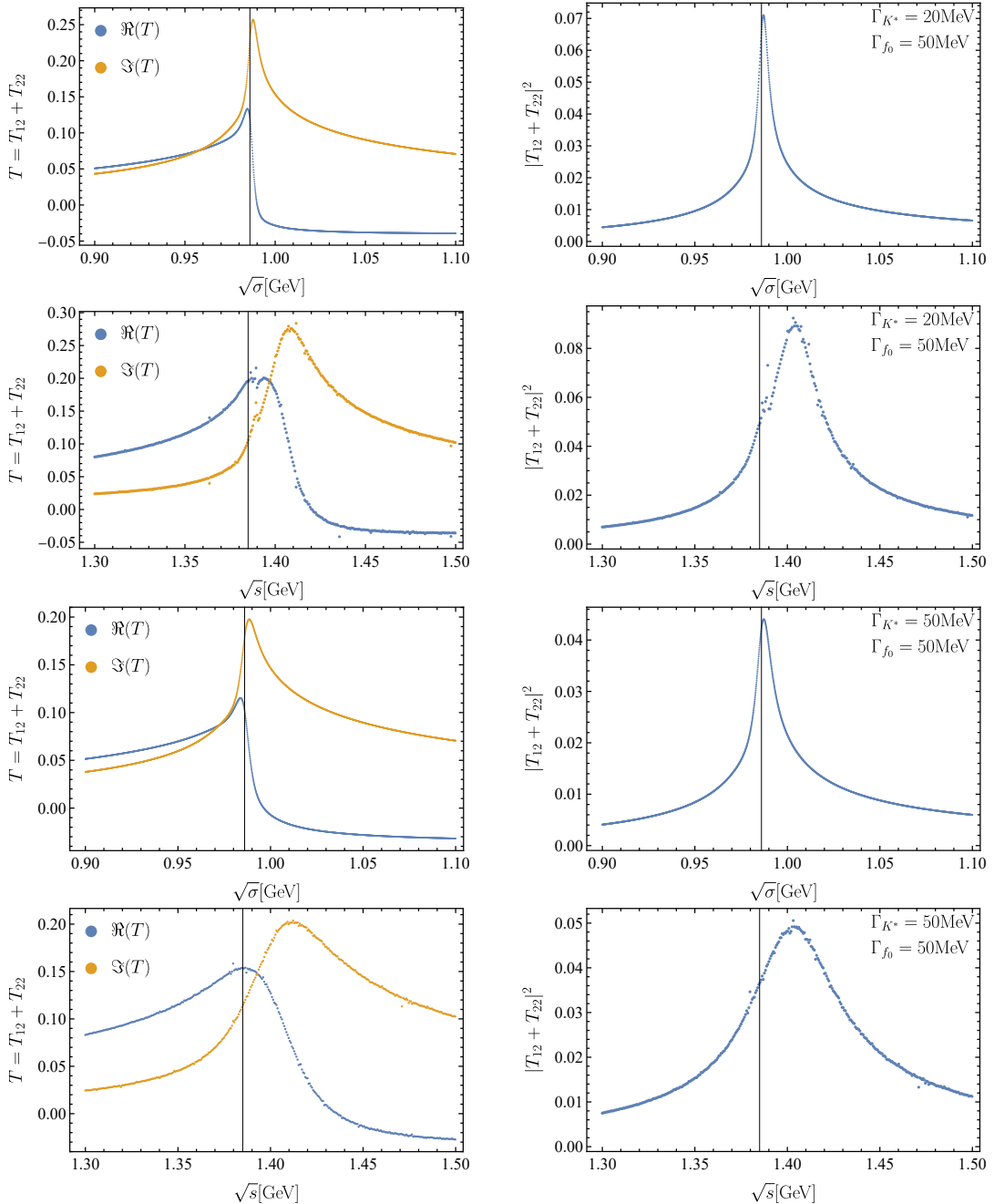


Figure 4.17: The amplitudes evaluated at the full-unitary level. The amplitudes here are the full amplitude (channel $1 \rightarrow 2 + \text{channel } 2 \rightarrow 2$). All the T - $\sqrt{\sigma}$ plots are evaluated for $\sqrt{s} = 1.42 \text{ GeV}$, with the black line denoting the $m_K + m_K$ threshold. All the T - \sqrt{s} plots are evaluated for $\sqrt{\sigma} = 0.99 \text{ GeV}$, with the black line denoting the $m_{K^*} + m_K$ threshold. The top two rows are evaluated for a K^* propagator with a width of 20 MeV, and the bottom two for a width of 50 MeV — this shows the smoothening of the peaks with increasing widths.

amplitudes evaluated are the channel 2 amplitudes, which include both $1 \rightarrow 2$ and $2 \rightarrow 2$ amplitudes. But it should be noted that the $2 \rightarrow 2$ amplitude doesn't have singularities or sharp features, therefore acts only as a background. We also see in the figure the effect of the width of the propagator — a larger width results in a less pronounced kinematical singularity. This is more apparent in figure 4.18.

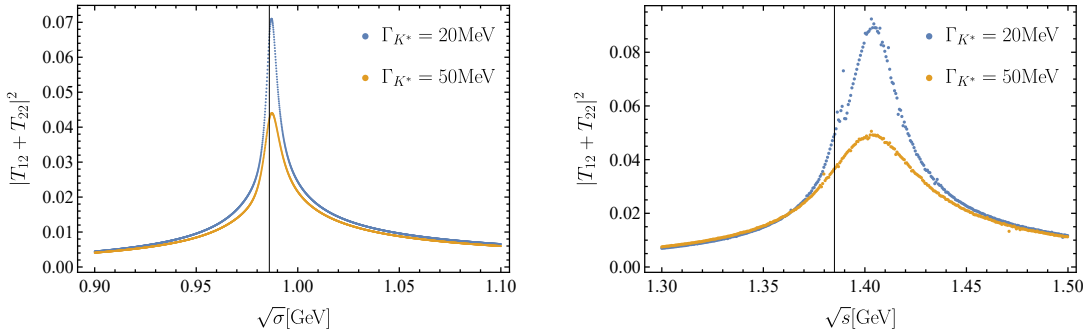


Figure 4.18: Amplitudes for K^* propagators of different widths. Larger width results in a less pronounced peak. The evaluated amplitude is the full channel 2 amplitude. The first plot is evaluated at fixed $\sqrt{s} = 1.42$ GeV, with the black line denoting the $m_K + m_K$ threshold. The second plot is evaluated at fixed $\sqrt{\sigma} = 0.99$ GeV, with the black line denoting the $m_{K^*} + m_K$ threshold.

Additionally, the primary contribution to the triangle singularity, fittingly, is from the triangle level. This is apparent in figure 4.19. Note that we compare only the $1 \rightarrow 2$ amplitudes in the latter plots. The Argand plots given in figure 4.20, demonstrate something significant. The first Argand plot for a fixed \sqrt{s} is deformed due to the stability of the participating kaons. But the second Argand plot for a fixed $\sqrt{\sigma}$ is rather circular. This is typically considered a signature of resonances. This shows how kinematical singularities mimic resonances, which are more fundamental. We should also recall from our previous discussions that the triangle singularity is sensitive to the incoming and outgoing invariants. That is, the energy regions in which a kinematical singularity is observed are very specific. In figure 4.21, we have evaluated the amplitudes outside the region in which the triangle singularity is expected. We do not see the kinematical singularity, but only the two-body cusp corresponding to either $m_K - m_K$ or $m_{K^*} - m_K$, at their respective two-body normal thresholds.

We recap briefly what we have done until this point. We have calculated the semi-connected isobar-spectator amplitude, \hat{T}_c^1 . This when multiplied by $\tau(\sigma(q))g_p$ from the right gives us the fully connected isobar-spectator amplitude, \hat{T}_c . Moreover, we need to calculate the disconnected isobar-spectator amplitude, \hat{T}_d , which is just $\tau(\sigma(q))g_p$ for us. Therefore, the full three-body amplitude for the process, $a_1(1420) \rightarrow \pi^+\pi^-\pi^+$, is given by

$$\hat{T} = \left(1 + \hat{T}_c^1(\sqrt{s}, q)\right) \tau(\sigma(q)) g_p. \quad (4.55)$$

In order to obtain a meaningful result out of the full three-body amplitude, one needs to integrate over the Lorentz-invariant phase space of the outgoing momenta. However, we do not take this route, since our study has been on a somewhat unphysical scalar system. A proper study would consist of considering the right partial wave projections. But this will not affect the presence of the triangle singularity, but only affect its feature. Since, the angular projected integral of the B -term still has similar logarithmic singularities. The couplings and dissociation vertex need to be properly parametrised, too. This is discussed in the next chapter.

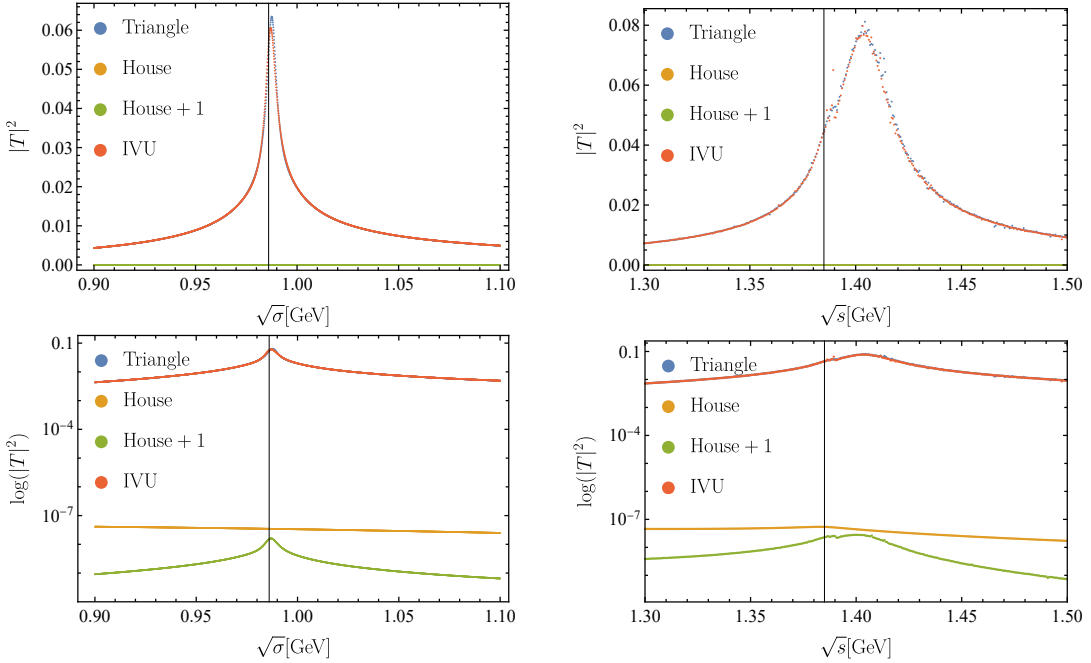


Figure 4.19: Contributions from the triangle, house, two-storied house and IVU to the triangle singularity (note that this is only the $1 \rightarrow 2$ contribution). We can see that most of the contribution is from the triangle level. In the first row, the first plot is evaluated at fixed $\sqrt{s} = 1.42$ GeV, with the black line denoting the $m_K + m_K$ threshold. And the second plot is evaluated at fixed $\sqrt{\sigma} = 0.99$ GeV, with the black line denoting the $m_{K^*} + m_K$ threshold. The second row contains the plots evaluated in logarithmic scale. This shows the missing contribution from the house level clearly.

4.2.5 An Alternate Numerical Implementation (Method1)

Now, we take a step back in our quest for an alternate numerical implementation of our solution to the Bethe-Salpeter ansatz. We recall that the Bethe-Salpeter ansatz, when formalised in a meaningful way, is the relativistic version of the Lippmann-Schwinger equation. The solutions to the Lippmann-Schwinger equation in the case of two interacting particles is determinable. But the situation at hand is the Lippmann-Schwinger equation of more than two-particles. Foldy and Tobocman [63] showed that in the case of more than three interacting particles, one cannot uniquely determine the solution. Faddeev [64] studied an operator equation of the form

$$\hat{T} = \hat{V} + \hat{T}\hat{G}\hat{V}, \quad (4.56)$$

which looks similar to the two particle case. Faddeev, then, derived a set of equations which determine the dynamics of a three particle system, that can be solved iteratively. For more, see also Faddeev's treatise on the subject [65]. Now, this is relevant to us, since the isobar-spectator model taken together with the Bethe-Salpeter ansatz, can be shown to be equivalent to the Faddeev equations. We do not get into the pedantics involved with the Faddeev equations, and concern ourselves with the numerical implementation of such an equation. In general, an integral in the momentum space given by

$$T = B + TK, \quad (4.57)$$

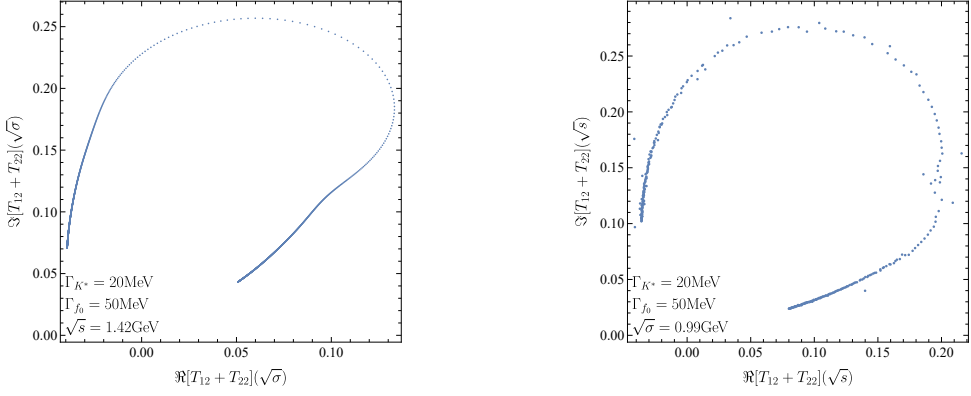


Figure 4.20: The Argand plots of the full semi-connected three-body amplitudes. The first plot shows the Argand plot corresponding to a fixed $\sqrt{s} = 1.42$ GeV. This is deformed due to the stability of the participating kaons. Whereas the Argand plot corresponds to a fixed $\sqrt{\sigma} = 0.99$ GeV, which is rather circular.

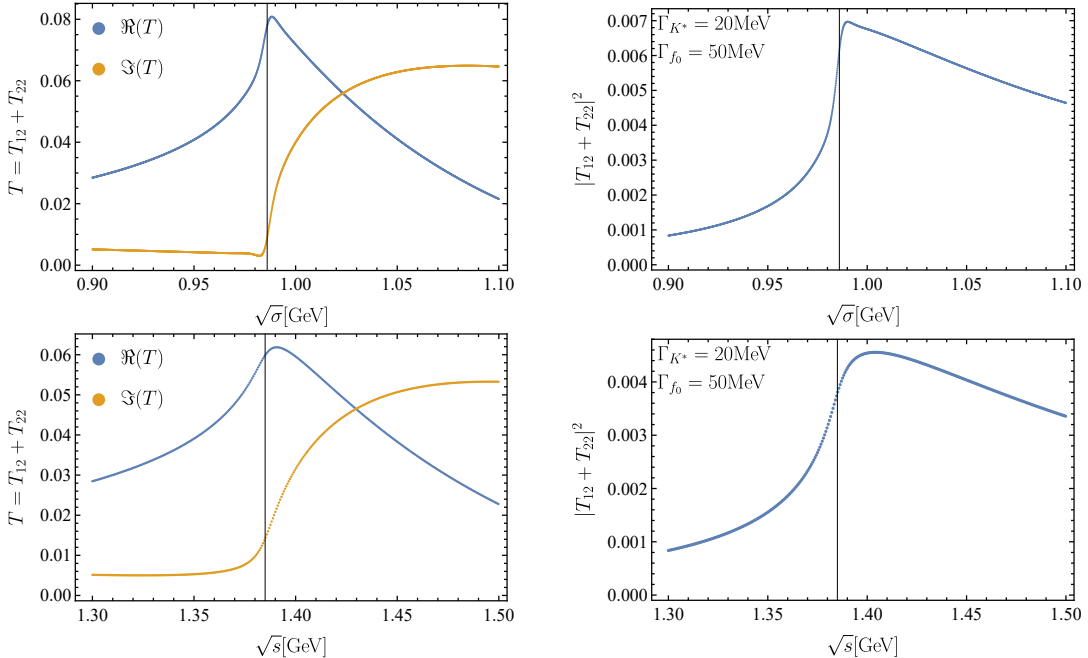


Figure 4.21: The amplitudes evaluated outside the singular region. The kinematical singularities have very specific energy regions in which they can be observed. In the first row, we have the amplitudes evaluated as a function of $\sqrt{\sigma}$, for a fixed $\sqrt{s} = 1.3$ GeV, which is outside the singular region. Similarly, in the second row, we have the amplitudes evaluated as a function of \sqrt{s} , for a fixed $\sqrt{\sigma} = 0.9$ GeV, which is also outside the singular region. The two-body cusps are exactly located at the two-body thresholds denoted by the black line — $m_K + m_K$ in the first row and $m_{K^*} + m_K$ in the second row. The cusp in the latter case is smoothed due to the finite width of K^* .

is the Fredholm integral of the second kind. Here, T , B and K are some operators. This can, formally, be solved by introducing the resolvent, $R = (\mathbb{1} - K)^{-1}$. The solution then is given by

$$T = B(\mathbb{1} - K)^{-1}. \quad (4.58)$$

In position representation, this becomes an integral, with K as the integration kernel. In our case, the integration kernel is just, $\tilde{\tau}B$. For more on integrals, one may refer to any standard textbook, like Kanwal [66]. This was, exactly, the approach taken to solve the integral in the previous section, without being alluded to. But there is still one point of subtlety — we need a formal way to handle the singularities. This was done previously by considering a complex integration contour, which has no singularities in its vicinity. And then, we used continued fractions to extrapolate the results on the real axis. Following Schmid & Ziegelmann [67], we propose an alternate numerical implementation. This method was originally introduced by Hetherington & Schick [57], and also used by Aaron & Amado [68], and later by Cahill & Sloan [69]. This method does not differ in the first half of the implementation. That is, a complex contour free of singularities is chosen, and the integral is then solved for that contour. This method differs at how the values on the real axis are then evaluated. To elaborate, in our attempt to solve the integral (4.44), whose discretised form is given by equation (4.46), we first choose a contour which is free of singularities. Notice that the order of the integration kernel and the semi-connected amplitude is different from the equations referred. However, both forms are equivalent, and the following discussion is not affected by which one we choose. We parametrise the contour as

$$f_{\text{sz}}(t) = te^{-ia}, \quad t \in [0, \Lambda]. \quad (4.59)$$

Here, a is some chosen real number, t is the contour parameter, and Λ is the cut-off value. This contour is just a ray starting from the complex origin. As long as a is not chosen to be too large, this method works. Note that this contour is different from the one that was used for $M0$. As long as the contours are obtained by continuously deforming the original contour, without crossing any non-analyticities, the evaluated integrals are exactly equal. Again, we discretise the contour and evaluate the values of the amplitudes on the complex contour. Then, we use these values, along with our knowledge of the singularities of the integral (4.44), to find out the values on the real axis. To get the semi-connected amplitudes, we need to perform one more integration, which is again carried out by carefully considering the singularities. This is the step where this method differs from our previous method — instead of using continued fractions to extrapolate to the real axis, we use our knowledge of the singularities of the integral to find out the values on the real axis.

Now, we need to understand the singularity structure of the integration kernel. The integration kernel, as mentioned before, consists of the isobar propagator, τ , and the interaction kernel (the exchange term), B . The exchange term has a rather complicated singularity structure, since it depends on both the incoming and the outgoing (spectator) momenta, p and q , along with the total three-body energy of the system, \sqrt{s} . Suppose, we are carrying out an integration over the incoming momentum p . Now, the singularities of the exchange term as an equation in p , depend on the value of q . We recall that the angular integral of the unprojected exchange term leads to a logarithm, see equation (4.45). We can see from this equation that the branch points of the logarithm are exactly the points corresponding to $z = \pm 1$. Physically, this corresponds to the spectators being either parallel or anti-parallel. Then, the zeros of the exchange term as an equation in p , corresponding to $-1 < z < 1$, determine the logarithmic branch cut. Also note that the equation for the zeros is quadratic in p . Therefore, we get two solutions for a given q , and

two corresponding branch points and a cut for each solution. Still, we do not have a problem if our integration contour, the real axis, does not contain the branch point or have the branch cut across it. Whether this is the case, exactly depends on the value of q . For small enough (real positive) values of q , the branch points lie on the real axis, with the branch cuts being line segments of finite length on the positive and negative real axes. A direct evaluation along the deformed contour is possible in this case, when q is held positive. As the value of q is increased, the branch points approach the origin from either side, and beyond a particular value, these points move to the other half of the complex plane, resulting in a circular branch cut. A direct evaluation along the deformed contour is no longer possible in this case. For large enough values of q , the zeros are no longer real, and the branch cuts are away from the real axis. A direct evaluation along the deformed contour is possible again. It is possible to solve for the zeros as an equation in p , and find the values of q corresponding to the three cases, by imposing the conditions — the branch points cross the positive and negative real complex planes, and the branch points acquire an imaginary component. We solve here for sufficiently large \sqrt{s} , as in our system — this affects the possible physical solutions, and we do not get into the details. First, the zeros of the exchange term is given by the solutions to the quadratic equation

$$\begin{aligned} & 4 \left(|\mathbf{q}|^2 z^2 - \left(\sqrt{s} - \sqrt{m_2^2 + |\mathbf{q}|^2} \right)^2 \right) |\mathbf{p}|^2 \\ & - 4|\mathbf{q}|z \left(\left(\sqrt{s} - \sqrt{m_2^2 + |\mathbf{q}|^2} \right)^2 - |\mathbf{q}|^2 + m_1^2 - m_{ex}^2 \right) |\mathbf{p}| \\ & + \left(\left(\sqrt{s} - \sqrt{m_2^2 + |\mathbf{q}|^2} \right)^2 - |\mathbf{q}|^2 + m_1^2 - m_{ex}^2 \right)^2 \\ & - 4 \left(\sqrt{s} - \sqrt{m_2^2 + |\mathbf{q}|^2} \right)^2 m_1^2 = 0. \end{aligned} \quad (4.60)$$

The values of $|\mathbf{q}|$ which correspond to a circular branch cut are then given by

$$\begin{aligned} & \frac{1}{2(\sqrt{s} - m_1)} \left[\left((\sqrt{s} - (m_1 + m_{ex}))^2 - m_2^2 \right) \left((\sqrt{s} - (m_1 - m_{ex}))^2 - m_2^2 \right) \right]^{1/2} \\ & \leq |\mathbf{q}| \leq \frac{\lambda^{1/2}(s, m_2^2, (m_1 + m_{ex})^2)}{2\sqrt{s}}. \end{aligned} \quad (4.61)$$

The right-hand side of the inequation has a direct physical correspondence — this is the value of q corresponding to the two-body $m_1 + m_{ex}$ threshold. For values of q larger than the right-hand side of the inequation, the outgoing spectator carries away too much of the available three-body energy, that the incoming spectator and the exchange particle cannot both go on-shell for the singularity. Therefore, for the on-shell spectator, an integration is not a problem. The left-hand side of the inequation is rather not as conspicuous — this is the value of q for which the spectator has to be at rest for a singularity on the real axis. The singularities on the real axis, in this case, arise when the outgoing spectator is parallel to the incoming spectator. For values of q smaller than the left-hand side of the inequation, the outgoing spectator carries too little of the available three-body energy, that the

singularity is imminent, irrespective of whether the outgoing spectator is parallel or anti-parallel. The values of q which correspond to a circular branch cut, are exactly when the momentum of the outgoing spectator is not large enough, that it has to necessarily be parallel to the incoming spectator. That is, the incoming spectator and the exchange particle are both anti-parallel for the corresponding branch point singularities. We reiterate that this intricacy arises only when one takes the outgoing spectator to be real. An integration by contour deformation is not a problem, when we let the spectator momenta take complex values. This was, exactly, what was exploited in the previous numerical implementation. We exploit the same again, but we make use of the knowledge of the location of the branch cuts to evaluate the values of the amplitudes on the real axis, when the outgoing spectator momenta have to be necessarily real. The singularities of the exchange term discussed so far, are depicted in figure 4.22 for B_{12} . In this case, we expect a circular branch cut for $0.313 \leq |\mathbf{q}|/\text{GeV} \leq 0.348$, for $\sqrt{s} = 1.42 \text{ GeV}$.

Coming to the singularities in the τ -term, by the definition of the isobar propagator, the pole lies at the physical mass of the isobar propagator, shifted by a value equal to its half-width, away from the physical sheet. Therefore, this should not pose any additional problem to our implementation, other than the obvious SEC hitting the new complex integration contour. Therefore, this method is implemented as follows: (1) The semi-connected three-body amplitude is evaluated for the points along the new complex integration contour (see figure 4.23). This gives the amplitude for complex outgoing spectator momenta, $[\tilde{\tau}T](\sqrt{s}, |\mathbf{q}|)$, as a function of \sqrt{s} and $|\mathbf{q}|$. Note, that the integration over the incoming spectator momenta is also carried out at this step. This is not different from the previous method, other than the obvious different integration contour; (2) The values for real external momenta are extracted in two different ways (see figure 4.22). For values of q which do not correspond to the circular branch cuts, the values on the real axis are simply determined by the values on the complex contour, through Cauchy's integral theorem:

$$T(\sqrt{s}, |\mathbf{q}| \in \mathbb{R}) = \sum_{p \in f_{SZ}} \tilde{\tau}(p) B(\sqrt{s}, |\mathbf{q}|; p) + \sum_{l \in f_{SZ}} [\tilde{\tau}T](\sqrt{s}, l) \tilde{\tau}(l) B(\sqrt{s}, |\mathbf{q}|; l), \quad (4.62)$$

where, $\tilde{\tau}$ denotes the modified isobar propagator, which also includes the prefactors of the integral. Note, that the discrete integration momenta are the magnitude of the corresponding 3-momenta. One can see that we use the amplitudes evaluated for complex outgoing spectator momenta, in the second term of the equation above (coloured red). Also, the first term contains an integration over the incoming spectator momentum. This, exactly, is the integral at the triangle level. Therefore, this method splits the contributions from the triangle level, and every subsequent levels, naturally. Again, evaluating the first term is still not a problem at this point. However, things are not as simple, for values of q which correspond to the circular branch cuts. The branch point singularity that is present on the lower half of the physical sheet, prevents a direct evaluation along the deformed contour. The values on the real axis are then given by an integration on the real axis up to the branch point, followed by crossing the branch cut into the second sheet, and integrating back to the origin. From here, we integrate along the chosen complex contour, using the values of the B -term on the second sheet up to the branch cut, and beyond

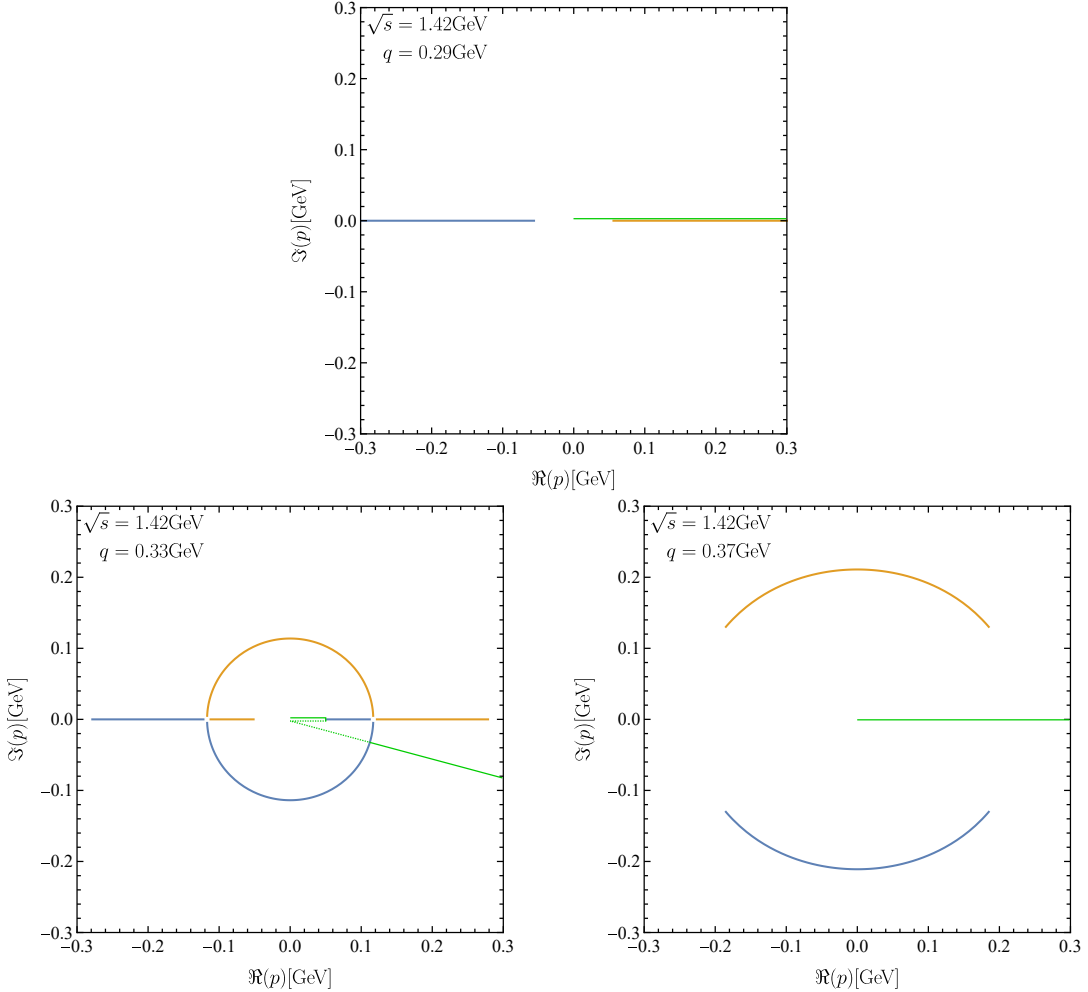


Figure 4.22: The singularity structure of the exchange term, B_{12} , for real outgoing spectator momenta, q . The first plot shows the branch cuts corresponding to small enough values of q . The second plot shows the circular branch cut, that is expected when q takes specific values. The third plot shows the branch cuts corresponding to large enough values of q . These branch cuts are obtained only when the outgoing spectator momentum is taken to be real. The green line shows the integration contour, as discussed in equations (4.62) & (4.63). The integration on the first Riemann sheet is given by the solid green line, and the integration on the second Riemann sheet is given by the dotted green line.

which we can use the values of the B on the first sheet. That is,

$$\begin{aligned}
 T(\sqrt{s}, |\mathbf{q}| \in \mathbb{R}) &= \sum_p \tilde{\tau}(p) B(\sqrt{s}, |\mathbf{q}|; p) - \sum_{l \in \mathbb{R}}^{\tau_1} \textcolor{blue}{T}(\sqrt{s}, l) \tilde{\tau}(l) \frac{2\pi i}{4l|\mathbf{q}|} \\
 &\quad + \sum_{\substack{l < \tau_2 \\ l \in f_{SZ}}} [\tilde{\tau}T](\sqrt{s}, l) \tilde{\tau}(l) \left(B(\sqrt{s}, |\mathbf{q}|; l) + \frac{2\pi i}{4l|\mathbf{q}|} \right) \\
 &\quad + \sum_{f_{SZ} \ni l \geq \tau_2} [\tilde{\tau}T](\sqrt{s}, l) \tilde{\tau}(l) B(\sqrt{s}, |\mathbf{q}|; l).
 \end{aligned} \tag{4.63}$$

Again, the discrete integration momenta are the magnitudes of the corresponding 3-momenta. Here, the first term corresponds to the triangle contribution. This

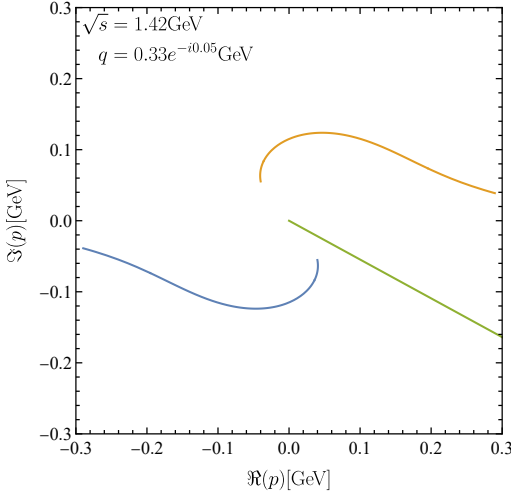


Figure 4.23: Relaxing the requirement that the outgoing spectator momentum is real in figure 4.22, results in branch cuts that are unsophisticated. This plot shows the branch cuts for a complex value of q . The green line shows the contour f_{sz} , discussed in the text. This contour is used for evaluations.

discrete integration is not trivial anymore. One has to carry out the steps discussed before, for this particular term as well. That is, this sum over p implicitly contains the latter three terms from the equation above, but only with τ as the integration kernel. This is necessary because of the same reasons mentioned before. The second term denotes the integration up to the branch point, and then back to the origin on the second Riemann sheet. This has been replaced by the discontinuity, and z_1 is the location of the branch point singularity. It should be noted, that we need here the values of the amplitude on the real axis determined by the previous equation (coloured blue). This is not a problem, since the values of l over which the discrete integral is carried out, lie in the region which does not correspond to the circular branch cuts. The third term corresponds to an integral on the second Riemann sheet, up to the point z_2 , where the complex integration contour meets the branch cut. And finally, the last term corresponds to an integral on the first Riemann sheet, up to the chosen cutoff. One can see that we use the amplitudes evaluated for complex outgoing spectator momenta, in the last two terms of the equation above (coloured red).

As for the specifics of the implementation, we choose an SMC, with a parameter, $\{a\} = \{0.1\}$, and a cutoff of 1.0 GeV. The self-energy integral is carried out along the same SEC, from the previous implementation. At the triangle level, for the values of q not corresponding to the circular branch cuts, we carry out the integral using Gaussian quadrature, with 60 Gaussian quadrature sampling points. For the values of q corresponding to the circular branch cuts, we carry out the integral, again, using Gaussian quadrature. We use 30 Gaussian quadrature sampling points for the second term in equation (4.63), and 60 Gaussian quadrature sampling points for the last two terms. The branch point lies significantly closer to the origin than the cutoff, and the reduced number of Gaussian quadrature points for the second term is justified. We do not need the values of T on the complex contour at this point, since, at the triangle level, the integration kernel is just the isobar propagator, τ . For the full unitarity level, we first evaluate the values of T on the complex contour,

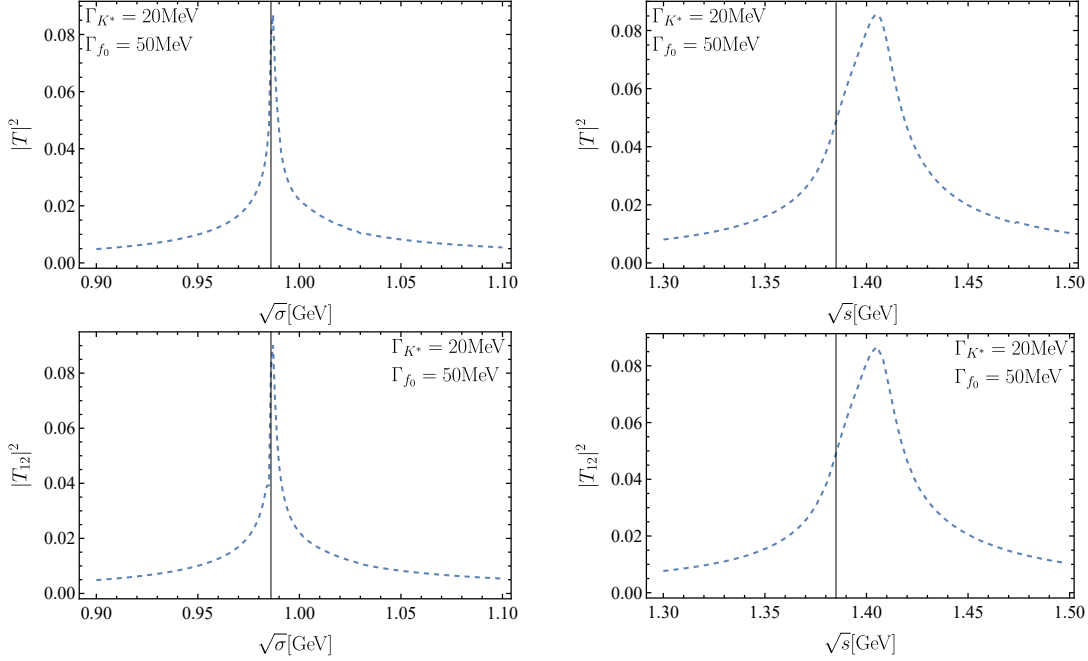


Figure 4.24: The amplitudes for the $1 \rightarrow 2$ channel transitions are given here. The top two plots are the amplitudes at the triangle level, and the bottom two plots are the amplitudes at the full unitarity level. The plots on the left show the amplitudes evaluated as a function of $\sqrt{\sigma}$, for a fixed $\sqrt{s} = 1.42$ GeV. The black line denotes the two-body, $m_K + m_K$ threshold. The plots on the right show the amplitudes evaluated as a function of $sqrts$, for a fixed $\sqrt{\sigma} = 0.99$ GeV. The black line denotes the two-body, $m_{K^*} + m_K$ threshold. The peak in the plots on the right is smoothed out due to the finite width of the K^* propagator, which is taken as 20 MeV. The width of the f_0 propagator is taken as 50 MeV. The real-imaginary parts of the amplitudes are given in figure H.3 in appendix H.

for 150 Gaussian quadrature sampling points. Then, the equations (4.62) and (4.63) are used to determine the values on the real axis. Again, 30 Gaussian quadrature sampling points are used for the integration on the real axis. The results are given in figure 4.24. The first two plots contain the amplitudes evaluated at the triangle level, and the latter two plots contain the amplitudes evaluated at the full unitarity level. In each row, the first plot contains amplitudes evaluated as a function of $\sqrt{\sigma}$ and the second plot contains the amplitudes evaluated as a function of \sqrt{s} . We should also mention that we have plotted only the channel 1 to channel 2 amplitudes, T_{12} , since we know that the contributions from the other channel transitions are insignificant. The real-imaginary parts of the amplitudes are given in figure H.3 in appendix H. An advantage of this particular method is that it separates the contributions from the triangle and the subsequent levels, naturally. With the evaluated amplitudes, one can note that the difference between the full unitarity and the triangle levels is of the order 10^{-4} . It should be noted that the subsequent levels still contain the triangle singularity, albeit not as the leading Landau singularity. We compare the contributions from the triangle level and the full unitarity level in figure 4.25.

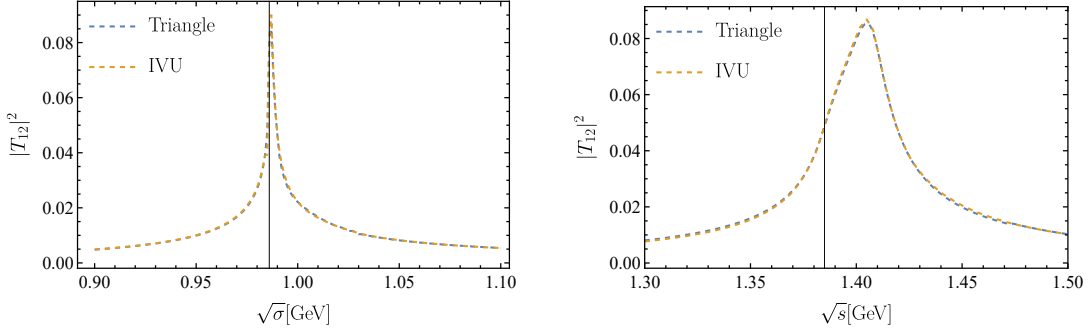


Figure 4.25: Contributions from the triangle and IVU to the triangle singularity. Similar to the previous numerical implementation, we can see that the amplitudes at the triangle level contributes the most to the singularity. The first plot is evaluated at fixed $\sqrt{s} = 1.42$ GeV, and the black line denotes the two-body $m_K + m_K$ threshold. The second plot is evaluated at fixed $\sqrt{\sigma} = 0.99$ GeV, and the black line denotes the two-body $m_{K^*} + m_K$ threshold.

Comparison with Method0

One should expect the same result, irrespective of the numerical implementation of the isobar-spectator model equations. The plots in figure 4.26, show the amplitudes evaluated by using Method0 and Method1, on top of each other. We can see that the evaluated amplitudes are similar, though some features stand out. In the first plot, the amplitude, at its peak, evaluated using Method1 is slightly larger than the amplitude evaluated using Method0. We should recall that the amplitudes in Method0 are interpolations from integration on a complex contour. This depends on how accurate the interpolated continued fraction is, and this can be improved by increasing the number of Gaussian quadrature sampling points. In the second plot, the values of the amplitudes are much more comparable, when accounted for the numerical instability. Method1 is more stable, at the cost of computational intensity. In Method0, the integral is evaluated numerically only once, which is then interpolated using a continued fraction. But in Method1, the integral is evaluated numerically first along a complex contour, and evaluated numerically once again as an application of Cauchy's integral theorem. For the values of q corresponding to the circular branch cuts, the computational overhead is significant, since the entire routine has to be applied to the triangle term, as well. The choice, then, is a matter of the nature of the problem at hand. With either of the methods, one can discernibly see the presence of a kinematical singularity, contributions to it from various levels, and the effect of propagator width on it. As discussed, the evaluated amplitude is only the semi-connected part of the amplitude. One should multiply this with the outgoing propagator, followed by an integration over the phase space of the external particles. The numerical stability, should then be tuned to satisfy that. For our present objective, this is only a minor problem.

Finally, we mention the other numerical implementations considered during the course of this work, along with a summary of the previous two numerical implementations. These were retrospectively named as follows.

- (i) *Method0 (M0)*: This is the original numerical implementation. The integral is solved along a complex contour, and the values on the real axis are given by a continued fraction. There is also the choice of using Padé approximants

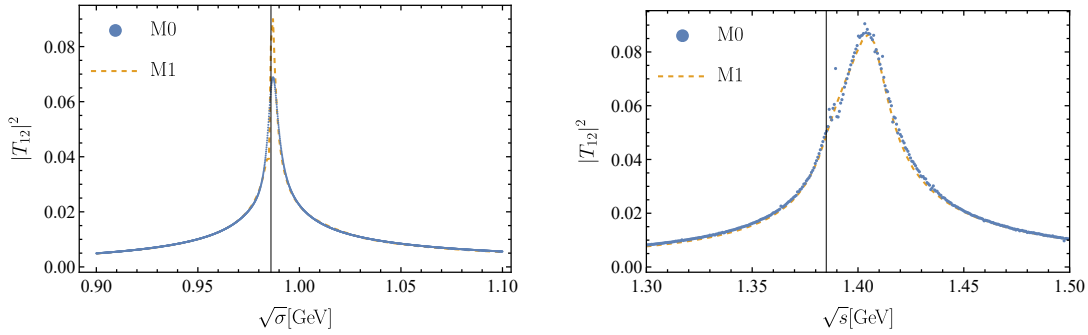


Figure 4.26: Method1 in comparison with Method0. The plots show the amplitudes evaluated by Method0 and Method1, on top of each other. The plot on the left is evaluated at fixed $\sqrt{s} = 1.42$ GeV, and the plot on the right is evaluated at fixed $\sqrt{\sigma} = 0.99$ GeV. The black lines denote the corresponding two-body thresholds. We can see that the amplitudes evaluated by either of the methods are similar.

to extrapolate to the values on the real axis. This was investigated, but later dropped.

- (ii) *Method1 (M1)*: This is the alternate method suggested in the last section of this chapter. The integral, again, is solved along a complex contour. The values on the real axis are obtained by making use of Cauchy's integral theorem.
- (iii) *Method2 (M2)*: In this method, the integral is directly solved for the values on the real axis. To do this, the amplitude T is replaced by an approximation constructed using an interpolation polynomial. This method is advantageous when the singularity structure of the integration kernel is not apparent. This is not the case in our system, and this method was not investigated. For more on this, refer to Sohre & Ziegelmann [70].
- (iv) *Method3 (M3)*: In this method, the integral is directly solved for real outgoing spectator momenta. The singularities are handled by adding a small imaginary part to the total energy of the three-body system, \sqrt{s} . The amplitudes are evaluated for multiple such small imaginary parts, and the final amplitude is evaluated as a limit of the imaginary part tending to zero linearly. This method though not as rigorous, leaves a lot of room for numerical fine tuning. But unfortunately, a full-unitary implementation was not possible. This method is briefly discussed in appendix G.

Certain methods are more advantageous, depending on the problem at hand. M0 and M1 proved to be versatile, in our case. With all the results presented, we summarise our findings in the next chapter.

Chapter 5

Summary and Outlook

“Begin at the beginning,” the King said gravely, “and go on till you come to the end: then stop.”

L. Carroll, ch.XII, *Alice’s Adventures in Wonderland* [71]

In brief: The isobar-spectator model [48] was implemented to the $a_1(1420)$ system by generalising it to the case with coupled channels and unequal masses. This model, being unitary, takes final-state rescattering effects into account, and also accommodates unstable particles. It was showed that the triangle singularity still persists, and the major contribution to the amplitudes is from the 1-loop or the triangle level. For this purpose, two primary numerical methods were used, which were also consistent with each other. Analytically, the Landau equations [19] were studied in the context of the final-state interactions of the $a_1(1420)$ system, and the expectations match the obtained results. Obvious and very relevant extensions to this work would be: (1) Implementing the model to the system with the right quantum numbers; (2) Studying the system on the lattice, using finite volume unitarity [72].

In this chapter, we summarise what was done, including possible shortfalls, and where one could go from here. We set out to understand how three-body unitarity affects the so-called $a_1(1420)$, which is rather explained to be a kinematical singularity, than a genuine resonance [2, 4, 7, 73]. But the studies carried out until this point do not respect unitarity. The main objective of this work was, then, to understand how kinematical singularities emerge in the context of a model that is innately unitary, particularly for the $a_1(1420)$ system. It should be noted that just like how two-body threshold cusps are a consequence of two-body unitarity, a logarithmic singularity is an inconspicuous consequence of three-body unitarity [12]. Therefore, one expects the triangle singularity to be still present. But this is not the complete story, since only the existence of the triangle singularity is ensured this way, and not how rescattering affects the amplitudes. Older results relating to triangle singularities and rescattering, like Schmid theorem [44], do not answer this question, as such theorems pertain to elastic rescattering. One also needs to consider a more formal way of parametrising the unstable propagators. This sets up the stage for the work carried out here.

In chapter 2, we reviewed the analytical aspects of kinematical singularities. The Landau equations, which give the conditions for kinematical singularities in an integral, were reviewed. This was studied in the context of the $a_1(1420)$ system. First, the kinematical singularity for the triangle diagram was reviewed. This mechanism was also reviewed by Guo et al. [40], which our work closely followed. This was extended to the diagram at the next loop order, the triangle+1 graph. We showed that there are no leading kinematical singularities in the particular graph we are interested in. However, there are subleading singularities in this graph, still. Through contractions, one can see that the same triangle singularity is no longer present. We also extended this to multi-loop graphs, and the situation here was slightly different. We do not have a leading singularity, by virtue of not having a leading singularity in the triangle+1 graph. However, the original triangle singularity is present again, and one can see this by carrying out contractions. No effort was made to study the other numerous subleading singularities associated with the triangle+ n graph categorically, since we posited that our work in chapter 4 showed that the contributions from higher orders are insignificant. One obvious extension of this chapter would be to study all the singularities, leading and subleading, arising in the triangle+ n graph. It should be recalled that the conditions for the singularity are still given by the Landau equations. Therefore, this essentially comes to categorising all the possible subleading singularities corresponding to this graph. Further, we recall that the Landau equations correspond to having the internal propagators go on-shell. This cannot happen for an isobar, in the sense of the Landau equations. The way our isobar propagator was parametrised, the imaginary part of its inverse was non-zero, and this corresponds to its width. This affects the amplitudes and the width of the peak at the location of the singularity, as seen. But an interesting task would be to reformulate the system in question, entirely in terms of stable particles. This is the main shortcoming of the analysis carried out in this chapter. All the intermediate particles are taken to be stable, at this point, and this is not in line with the analysis carried out later, in chapter 4. Though, the effect of taking this into consideration can be seen in the obtained results, and does not modify our expectations much. In chapter 3, we reviewed non-unitary models that are used to demonstrate the triangle singularity in the $a_1(1420)$ system. This was along the line of the work by Mikhasenko et al. [4]. This naïve model consists of three internal propagators, and the corresponding loop integral is solved for. To account for the instability of the internal propagator, one adds an arbitrary width to the corresponding propagator. We also explicitly calculated the amplitudes at the triangle+1 level, and showed that there is no triangle singularity, just as expected. We also noted the presence of the two-body thresholds, however, which is again, just as expected. Even discounting the way in which the unstable propagator obtained a width, such a model still does not take unitarity and rescattering into account. This naturally answers the cruciality of the study carried out in chapter 4.

In chapter 4, we first reviewed the isobar-spectator model, which is innately unitary. The particular model used in this work was introduced by Mai et al. [48]. The isobar propagator, which corresponds to the unstable propagator from chapter 3, and the exchange term, which corresponds to the stable particle exchange from chapter 3, are formulated covariantly in this model. The spectators are stable, and hence, taken to be on-shell. These three quantities are the most basic ingredients of this model. We showed that the implementation of three-body unitarity naturally

requires a second channel. This led to a coupled-channel analysis within this model. We, then, calculated the parameters — the bare masses and the couplings — of the respective isobar propagators, and also defined the coupled-channel exchange term. The next step was to numerically solve the integral for the semi-connected isobar-spectator amplitude, \hat{T}_c^1 , and two methods were discussed mainly in this work — *M0* & *M1*. The results obtained through either of the methods were comparable. We showed that the triangle singularity persists, even after taking three-body unitarity into account. The contributions from higher order diagrams, though non-zero, were shown to be insignificant. This supports the assertion that the study of a system, which is explained to be a kinematical singularity, is ample at the first order in which the said singularity appears. This entirely depends on the observation that the higher order contributions in our study were insignificant. However, this no longer holds if higher order contributions are no longer insignificant. As for the methods, *M0* was initially implemented with Padé approximants, which was later replaced with continued fractions. We noticed that the Padé approximants had trouble reproducing sharp features, particularly the logarithmic singularities in our case. We suspect that this is due to Padé approximants being an extrapolation of a fit, rather than interpolation as with the case of continued fractions. Still, the way our integration routine was implemented, *M0* had problems in the regions where two non-analyticities were lying close to each other — a two-body threshold cusp and a logarithmic singularity, in our case. However, this did not muddle the singularity picture. The alternate numerical implementation, *M1*, was far better at handling and reproducing such problematic regions, at the cost of being numerically intensive. Finally, *M3* was shown to work only at the triangle level. This method, however, was a good sanity check of the results obtained from other numerical implementations. A possible shortfall could be that we did not formally analyse the errors in our numerical implementations. It should also be noted that the main source of error would be the integration routine, Gaussian quadrature. Gaussian quadrature converges exponentially faster with increasing quadrature points [74]. We ensured that the integration mesh was dense enough, and the value of the evaluated integral did not differ significantly, with further increasing quadrature points. Also, certain input parameters, like the physical masses and widths, also contribute to errors in the final amplitudes. An exact analysis of errors in this regard was not carried out, since the primary objective was to understand the behaviour of the kinematical singularity in a unitary model, and this goal was achieved. Further, the model considered in question was a bit far from the physical system, so it cannot be matched to experimental results. This brings us to the first possible extension of the study carried out here. From here, one can easily extend this to the real pseudovector system. This will be along the line of the works of Aceti et al. [7] and Sadasivan et al. [51, 52]. In such a study, calculating the full three-body amplitude, \hat{T} , is more meaningful. As mentioned before, \hat{T}_c^1 was supposed to contain the non-trivial part of the three-body amplitude, which was exactly what was calculated. From here, one may calculate the full connected three-body amplitude \hat{T}_c , which corresponds to just multiplying the semi-connected amplitude by the isobar propagator on the right, and integrating over the available phase space. And to this the disconnected amplitude \hat{T}_d is added, giving us the full three-body amplitude. These steps, though trivial, would be more meaningful when carried out for the real system. In regard to the scalar system considered here, one may still ask the question what happens

when the contributions from the higher orders are not insignificant. This amounts to cleverly redefining the parameters in such a way that this produces the amplitudes we are after. However, this will be further from the physical system, since the exact parameters used here directly arose from matching them with the physical parameters. One may also formally compare all the different numerical implementations considered here, their advantages and drawbacks. A bit more interesting extension would be to study this particular system in lattice QCD. To this end, one needs to implement finite volume three-body unitarity to this system, see Mai et al. [72].

Acknowledgements

I extend my most sincere gratitude to my advisers, PD Dr Akaki Rusetsky and Dr Maxim Mai. Maxim's continuous availability and guidance, along with his insightful questions, were pivotal to this project. His willingness to assist with even the simplest problems, and his invaluable insights, helped me learn a lot. I should not forget Akaki's astute comments and suggestions, which were indispensable. He took his time to explain the most basic problems I had during the course of this project, which again, I am very grateful for. Akaki and Maxim also helped me extensively with the final version of this thesis, which was initially rife with typographical errors and slightly confusing statements. I am also thankful for the engaging academic and non-academic discussions we shared outside the scope of this project.

A special thanks to Dr Michael Döring, for his invaluable comments on the three-body unitary formalism, and for generously agreeing to weekly meetings. My gratitude extends to Rishabh Bubna for his crucial support in implementing Method1. Rishabh was very helpful and the implementation of Method1 would not have been possible without his assistance. I would like to thank Helen Meyer for proofreading my thesis, and for the very helpful feedback. Helen also helped me with a lot of administrative processes, which I am also very grateful for.

I express my sincere appreciation to the HISKP and PI institutes at the University of Bonn for providing the necessary resources, both material and non-material. The frequent events organized by HISKP, especially the board game evenings by PD Dr. Kubis's group and social gatherings by the groups of Prof. Meißner, Prof. Urbach and PD Dr. Rusetsky, created a vibrant academic community.

Finally, none of this would have been possible without the support of my *Amma* and *Appa*. Their encouragement has been my pillar of strength. I also thank all my friends for their constant support and motivation. I extend my apologies to anyone inadvertently omitted here; the oversight is entirely mine. *Live Long and Prosper.*

Bibliography

- [1] S. Mizera. “Physics of the analytic S -matrix”. In: *Physics Reports* 1047 (Jan. 2024), pp. 1–92. ISSN: 0370-1573. DOI: [10.1016/j.physrep.2023.10.006](https://doi.org/10.1016/j.physrep.2023.10.006).
- [2] C. Adolph et al. “Observation of a New Narrow Axial-Vector Meson $a_1(1420)$ ”. In: *Physical Review Letters* 115.8 (Aug. 2015), p. 082001. ISSN: 1079-7114. DOI: [10.1103/physrevlett.115.082001](https://doi.org/10.1103/physrevlett.115.082001).
- [3] I. Khokhlov et al. “Partial wave analyses of the $\pi^-\pi^0\pi^0$ and $\pi^-\pi^0$ systems with VES setup”. In: *Proceedings of XV International Conference on Hadron Spectroscopy — PoS(Hadron 2013)*. Hadron 2013. Sissa Medialab, Apr. 2014. DOI: [10.22323/1.205.0088](https://doi.org/10.22323/1.205.0088).
- [4] M. Mikhasenko, B. Ketzer, and A. Sarantsev. “Nature of the $a_1(1420)$ ”. In: *Physical Review D* 91.9 (May 2015), p. 094015. ISSN: 1550-2368. DOI: [10.1103/physrevd.91.094015](https://doi.org/10.1103/physrevd.91.094015).
- [5] H.-X. Chen et al. “ $a_1(1420)$ resonance as a tetraquark state and its isospin partner”. In: *Physical Review D* 91.9 (May 2015), p. 094022. ISSN: 1550-2368. DOI: [10.1103/physrevd.91.094022](https://doi.org/10.1103/physrevd.91.094022).
- [6] T. Gutsche et al. “Test of the multiquark structure of $a_1(1420)$ in strong two-body decays”. In: *Physical Review D* 96.11 (Dec. 2017), p. 114004. ISSN: 2470-0029. DOI: [10.1103/physrevd.96.114004](https://doi.org/10.1103/physrevd.96.114004).
- [7] F. Aceti, L. R. Dai, and E. Oset. “The “ $a_1(1420)$ ” peak as the $\pi f_0(980)$ decay mode of the $a_1(1260)$ ”. In: *Physical Review D* 94.9 (Nov. 2016), p. 096015. ISSN: 2470-0029. DOI: [10.1103/physrevd.94.096015](https://doi.org/10.1103/physrevd.94.096015).
- [8] G. D. Alexeev et al. “Triangle Singularity as the Origin of the $a_1(1420)$ ”. In: *Physical Review Letters* 127.8 (Aug. 2021), p. 082501. ISSN: 1079-7114. DOI: [10.1103/physrevlett.127.082501](https://doi.org/10.1103/physrevlett.127.082501).
- [9] R. Zwicky. *A brief Introduction to Dispersion Relations and Analyticity*. 2016. DOI: [10.48550/ARXIV.1610.06090](https://arxiv.org/abs/1610.06090).
- [10] A. Zhiboedov. *The Analytic S-Matrix*. Lecture Notes. 2021. URL: <https://www.ipht.fr/Docspht/search/article.php?IDA=12792>.
- [11] L. V. Ahlfors. *Complex Analysis. An introduction to the theory on analytic functions of one complex variable*. 3rd ed. International series in pure and applied mathematics. New York [u.a.]: McGraw-Hill, 2007. 331 pp. ISBN: 978-0070006577.
- [12] R. J. Eden, P. V. Landshoff, D. I. Olive, and J. C. Polkinghorne. *The Analytic S-Matrix*. Ed. by R. J. Eden. Cambridge: Cambridge Univ. Press, 1966. 287 pp. ISBN: 0521523362.

- [13] M. E. Peskin and D. V. Schroeder. *An Introduction to Quantum Field Theory*. Ed. by D. V. Schroeder. Student economy edition. The advanced book program. Boulder: Westview Press, a member of the Perseus Books Group, 2016. 842 pp. ISBN: 9780813350196.
- [14] A. Das. *Lectures on Quantum Field Theory*. WORLD SCIENTIFIC, Sept. 2008. ISBN: 9789812832870. DOI: [10.1142/6938](https://doi.org/10.1142/6938).
- [15] G. 't Hooft and M. Veltman. "Scalar one-loop integrals". In: *Nuclear Physics B* 153 (Jan. 1979), pp. 365–401. ISSN: 0550-3213. DOI: [10.1016/0550-3213\(79\)90605-9](https://doi.org/10.1016/0550-3213(79)90605-9).
- [16] R. J. Eden. "Threshold behaviour in quantum field theory". In: *Proceedings of the Royal Society of London. Series A. Mathematical and Physical Sciences* 210.1102 (1102 Jan. 1952), pp. 388–404. ISSN: 2053-9169. DOI: [10.1098/rspa.1952.0008](https://doi.org/10.1098/rspa.1952.0008).
- [17] J. Hadamard. "Théorème sur les séries entières". In: *Acta Mathematica* 22.0 (1899), pp. 55–63. ISSN: 0001-5962. DOI: [10.1007/bf02417870](https://doi.org/10.1007/bf02417870).
- [18] D. Fotiadi, M. Froissart, J. Lascoux, and F. Pham. "Applications of an isotopy theorem". In: *Topology* 4.2 (Oct. 1965), pp. 159–191. ISSN: 0040-9383. DOI: [10.1016/0040-9383\(65\)90063-7](https://doi.org/10.1016/0040-9383(65)90063-7).
- [19] L. D. Landau. "On analytic properties of vertex parts in quantum field theory". In: *Nuclear Physics* 13.1 (Oct. 1959), pp. 181–192. ISSN: 0029-5582. DOI: [10.1016/0029-5582\(59\)90154-3](https://doi.org/10.1016/0029-5582(59)90154-3).
- [20] N. Nakanishi. "On the Validity of Dispersion Relations in Perturbation Theory". In: *Progress of Theoretical Physics* 21.1 (Jan. 1959), pp. 135–150. ISSN: 0033-068X. DOI: [10.1143/ptp.21.135](https://doi.org/10.1143/ptp.21.135).
- [21] J. D. Bjorken. "Experimental tests of Quantum electrodynamics and spectral representations of Green's functions in perturbation theory". PhD thesis. Stanford U., 1959.
- [22] J. C. Polkinghorne and G. R. Screamton. "The analytic properties of perturbation theory — I". In: *Il Nuovo Cimento* 15.2 (Jan. 1960), pp. 289–300. ISSN: 1827-6121. DOI: [10.1007/bf02860252](https://doi.org/10.1007/bf02860252).
- [23] J. C. Polkinghorne and G. R. Screamton. "The analytic properties of perturbation theory — II". In: *Il Nuovo Cimento* 15.6 (Mar. 1960), pp. 925–931. ISSN: 1827-6121. DOI: [10.1007/bf02860197](https://doi.org/10.1007/bf02860197).
- [24] R. E. Cutkosky. "Singularities and Discontinuities of Feynman Amplitudes". In: *Journal of Mathematical Physics* 1.5 (Sept. 1960), pp. 429–433. ISSN: 1089-7658. DOI: [10.1063/1.1703676](https://doi.org/10.1063/1.1703676).
- [25] D. B. Fairlie, P. V. Landshoff, J. Nuttall, and J. C. Polkinghorne. "Singularities of the Second Type". In: *Journal of Mathematical Physics* 3.4 (July 1962), pp. 594–602. ISSN: 1089-7658. DOI: [10.1063/1.1724262](https://doi.org/10.1063/1.1724262).
- [26] D. B. Fairlie, P. V. Landshoff, J. Nuttall, and J. C. Polkinghorne. "Physical sheet properties of second type singularities". In: *Physics Letters* 3.1 (Nov. 1962), pp. 55–56. ISSN: 0031-9163. DOI: [10.1016/0031-9163\(62\)90200-7](https://doi.org/10.1016/0031-9163(62)90200-7).

- [27] J. Mathews. “Application of Linear Network Analysis to Feynman Diagrams”. In: *Physical Review* 113.1 (Jan. 1959), pp. 381–381. ISSN: 0031-899X. DOI: [10.1103/physrev.113.381](https://doi.org/10.1103/physrev.113.381).
- [28] T. T. Wu. “Domains of Definition for Feynman Integrals over Real Feynman Parameters”. In: *Physical Review* 123.2 (July 1961), pp. 678–689. ISSN: 0031-899X. DOI: [10.1103/physrev.123.678](https://doi.org/10.1103/physrev.123.678).
- [29] C. Itzykson and J.-B. Zuber. *Quantum Field Theory*. Dover edition. Dover books on physics. Mineola, New York: Dover Publications, Inc., 2005. 1705 pp. ISBN: 9780486134697.
- [30] Y. Nambu. “Parametric representations of general Green’s functions”. In: *Il Nuovo Cimento* 6.5 (Nov. 1957), pp. 1064–1083. ISSN: 1827-6121. DOI: [10.1007/bf02747390](https://doi.org/10.1007/bf02747390).
- [31] R. Karplus, C. M. Sommerfield, and E. H. Wichmann. “Spectral Representations in Perturbation Theory. I. Vertex Function”. In: *Physical Review* 111.4 (Aug. 1958), pp. 1187–1190. ISSN: 0031-899X. DOI: [10.1103/physrev.111.1187](https://doi.org/10.1103/physrev.111.1187).
- [32] M. Fowler, P. V. Landshoff, and R. W. Lardner. “Some properties of single loop diagrams in perturbation theory”. In: *Il Nuovo Cimento* 17.6 (Sept. 1960), pp. 956–963. ISSN: 1827-6121. DOI: [10.1007/bf02732141](https://doi.org/10.1007/bf02732141).
- [33] T. Sawada. “On the Anomalous Threshold and Composite Particles”. In: *Progress of Theoretical Physics* 27.5 (May 1962), pp. 882–898. ISSN: 0033-068X. DOI: [10.1143/ptp.27.882](https://doi.org/10.1143/ptp.27.882).
- [34] Y.-C. Liu. “Kinematical Interpretation of Anomalous Thresholds”. In: *Physical Review Letters* 30.5 (Jan. 1973), pp. 184–188. ISSN: 0031-9007. DOI: [10.1103/physrevlett.30.184](https://doi.org/10.1103/physrevlett.30.184).
- [35] J. Tarski. “Analyticity of the Fourth Order Scattering Amplitude with Two Complex Invariants”. In: *Journal of Mathematical Physics* 1.2 (Mar. 1960), pp. 149–163. ISSN: 1089-7658. DOI: [10.1063/1.1703645](https://doi.org/10.1063/1.1703645).
- [36] H. S. Hannesdottir and S. Mizera. *What is the $i\varepsilon$ for the S-matrix?* Springer International Publishing, 2022. ISBN: 9783031182587. DOI: [10.1007/978-3-031-18258-7](https://doi.org/10.1007/978-3-031-18258-7).
- [37] S. Coleman and R. E. Norton. “Singularities in the physical region”. In: *Il Nuovo Cimento* 38.1 (July 1965), pp. 438–442. ISSN: 1827-6121. DOI: [10.1007/bf02750472](https://doi.org/10.1007/bf02750472).
- [38] J. C. Taylor. “Analytic Properties of Perturbation Expansions”. In: *Physical Review* 117.1 (Jan. 1960), pp. 261–265. ISSN: 0031-899X. DOI: [10.1103/physrev.117.261](https://doi.org/10.1103/physrev.117.261).
- [39] R. L. Workman et al. “Review of Particle Physics”. In: *Progress of Theoretical and Experimental Physics* 2022.8 (Aug. 2022). ISSN: 2050-3911. DOI: [10.1093/ptep/ptac097](https://doi.org/10.1093/ptep/ptac097).
- [40] F.-K. Guo, X.-H. Liu, and S. Sakai. “Threshold cusps and triangle singularities in hadronic reactions”. In: *Progress in Particle and Nuclear Physics* 112 (May 2020), p. 103757. ISSN: 0146-6410. DOI: [10.1016/j.ppnp.2020.103757](https://doi.org/10.1016/j.ppnp.2020.103757).

BIBLIOGRAPHY

- [41] A. Martin. “Selected topics on analyticity in potential scattering”. In: *Il Nuovo Cimento* 21.S2 (Oct. 1961), pp. 157–196. ISSN: 1827-6121. DOI: [10.1007/bf02747776](https://doi.org/10.1007/bf02747776).
- [42] R. F. Peierls. “Possible Mechanism for the Pion-Nucleon Second Resonance”. In: *Physical Review Letters* 6.11 (June 1961), pp. 641–643. ISSN: 0031-9007. DOI: [10.1103/physrevlett.6.641](https://doi.org/10.1103/physrevlett.6.641).
- [43] C. Goebel. “Comments on Higher Resonance Models”. In: *Physical Review Letters* 13.4 (July 1964), pp. 143–146. ISSN: 0031-9007. DOI: [10.1103/physrevlett.13.143](https://doi.org/10.1103/physrevlett.13.143).
- [44] C. Schmid. “Final-State Interactions and the Simulation of Resonances”. In: *Physical Review* 154.5 (Feb. 1967), pp. 1363–1375. ISSN: 0031-899X. DOI: [10.1103/physrev.154.1363](https://doi.org/10.1103/physrev.154.1363).
- [45] M.-C. Du and Q. Zhao. “Internal particle width effects on the triangle singularity mechanism in the study of the $\eta(1405)$ and $\eta(1475)$ puzzle”. In: *Physical Review D* 100.3 (Aug. 2019), p. 036005. ISSN: 2470-0029. DOI: [10.1103/physrevd.100.036005](https://doi.org/10.1103/physrevd.100.036005).
- [46] M. Bayar, F. Aceti, F.-K. Guo, and E. Oset. “Discussion on triangle singularities in the $\Lambda b \rightarrow J/\Psi K^- p$ reaction”. In: *Physical Review D* 94.7 (Oct. 2016), p. 074039. ISSN: 2470-0029. DOI: [10.1103/physrevd.94.074039](https://doi.org/10.1103/physrevd.94.074039).
- [47] L. D. Faddeev and S. P. Merkuriev. *Quantum Scattering Theory for Several Particle Systems*. Springer Netherlands, 1993. ISBN: 9789401728324. DOI: [10.1007/978-94-017-2832-4](https://doi.org/10.1007/978-94-017-2832-4).
- [48] M. Mai et al. “Three-body unitarity with isobars revisited”. In: *The European Physical Journal A* 53.9 (Sept. 2017). ISSN: 1434-601X. DOI: [10.1140/epja/i2017-12368-4](https://doi.org/10.1140/epja/i2017-12368-4).
- [49] R. Aaron, R. D. Amado, and J. E. Young. “Relativistic Three-Body Theory with Applications to π - N Scattering”. In: *Physical Review* 174.5 (Oct. 1968), pp. 2022–2032. ISSN: 0031-899X. DOI: [10.1103/physrev.174.2022](https://doi.org/10.1103/physrev.174.2022).
- [50] R. Aaron. “A Relativistic Three-Body Theory”. In: *Modern Three-Hadron Physics*. Springer Berlin Heidelberg, 1977, pp. 139–179. ISBN: 9783642810701. DOI: [10.1007/978-3-642-81070-1_5](https://doi.org/10.1007/978-3-642-81070-1_5).
- [51] D. Sadasivan, M. Mai, H. Akdag, and M. Döring. “Dalitz plots and lineshape of $a_1(1260)$ from a relativistic three-body unitary approach”. In: *Physical Review D* 101.9 (May 2020), p. 094018. ISSN: 2470-0029. DOI: [10.1103/physrevd.101.094018](https://doi.org/10.1103/physrevd.101.094018).
- [52] D. Sadasivan et al. “Pole position of the $a_1(1260)$ resonance in a three-body unitary framework”. In: *Physical Review D* 105.5 (Mar. 2022), p. 054020. ISSN: 2470-0029. DOI: [10.1103/physrevd.105.054020](https://doi.org/10.1103/physrevd.105.054020).
- [53] M. Garofalo et al. “Three-body resonances in the Φ^4 theory”. In: *Journal of High Energy Physics* 2023.2 (Feb. 2023). ISSN: 1029-8479. DOI: [10.1007/jhep02\(2023\)252](https://doi.org/10.1007/jhep02(2023)252).
- [54] M. Ablikim et al. “Resonances in $J/\Psi \rightarrow \Phi\pi^+\pi^-$ and ΦK^+K^- ”. In: *Physics Letters B* 607.3-4 (Feb. 2005), pp. 243–253. ISSN: 0370-2693. DOI: [10.1016/j.physletb.2004.12.041](https://doi.org/10.1016/j.physletb.2004.12.041).

- [55] B. Aubert et al. “Dalitz plot analysis of the decay $B^\pm \rightarrow K^\pm K^\pm K^\mp$ ”. In: *Physical Review D* 74.3 (Aug. 2006), p. 032003. ISSN: 1550-2368. DOI: [10.1103/physrevd.74.032003](https://doi.org/10.1103/physrevd.74.032003).
- [56] M. Jacob and G. C. Wick. “On the general theory of collisions for particles with spin”. In: *Annals of Physics* 7.4 (Aug. 1959), pp. 404–428. ISSN: 0003-4916. DOI: [10.1016/0003-4916\(59\)90051-x](https://doi.org/10.1016/0003-4916(59)90051-x).
- [57] J. H. Hetherington and L. H. Schick. “Exact Multiple-Scattering Analysis of Low-Energy Elastic K^- - d Scattering with Separable Potentials”. In: *Physical Review* 137.4B (Feb. 1965), B935–B948. ISSN: 0031-899X. DOI: [10.1103/physrev.137.b935](https://doi.org/10.1103/physrev.137.b935).
- [58] D. Binosi, A. Pilloni, and R.-A. Tripolt. “Study for a model-independent pole determination of overlapping resonances”. In: *Physics Letters B* 839 (Apr. 2023), p. 137809. ISSN: 0370-2693. DOI: [10.1016/j.physletb.2023.137809](https://doi.org/10.1016/j.physletb.2023.137809).
- [59] W. B. Jones and W. J. Thron. *Continued fractions. Analytic theory and applications*. Advanced book program. Literaturverz. S. 404 - 419. Reading, Mass. [u.a.]: Addison-Wesley, 1980, pp. 185–197. 428 pp. ISBN: 0201135108.
- [60] M. Abramowitz and I. A. Stegun. *Handbook of mathematical functions. With formulas, graphs, and mathematical tables*. 9th ed. Dover books on mathematics. New York, NY: Dover Publ., 2013. 1046 pp. ISBN: 9780486612720.
- [61] G. H. Hardy. *An introduction to the theory of numbers*. Ed. by E. M. Wright and D. R. Heath-Brown. Sixth edition. Oxford mathematics. Oxford: Oxford University Press, 2008. 621 pp. ISBN: 0199219850.
- [62] W. Ewald and W. Sieg, eds. *David Hilbert's Lectures on the Foundations of Arithmetic and Logic 1917-1933*. Springer Berlin Heidelberg, 2013. ISBN: 9783540694441. DOI: [10.1007/978-3-540-69444-1](https://doi.org/10.1007/978-3-540-69444-1).
- [63] L. L. Foldy and W. Tobocman. “Application of Formal Scattering Theory to Many-Body Problems”. In: *Physical Review* 105.3 (Feb. 1957), pp. 1099–1100. ISSN: 0031-899X. DOI: [10.1103/physrev.105.1099](https://doi.org/10.1103/physrev.105.1099).
- [64] L. D. Faddeev. “Scattering theory for a three particle system”. In: *Zh. Eksp. Teor. Fiz.* 39 (1960), pp. 1459–1467.
- [65] L. D. Faddeev. *Mathematical Aspects of the Three-body Problem in Quantum Scattering Theory*. Ed. by I. Meroz. Trans. by C. Gutfreund. Israel Program for Scientific Translations, 1965.
- [66] R. P. Kanwal. *Linear Integral Equations*. Birkhäuser Boston, 1997. ISBN: 978-1461207658. DOI: [10.1007/978-1-4612-0765-8](https://doi.org/10.1007/978-1-4612-0765-8).
- [67] E. W. Schmid and H. Ziegelmann. *The Quantum Mechanical Three-Body Problem*. Vieweg Tracts in Pure and Applied Physics 2. Braunschweig: Vieweg, 1974. 217 pp. ISBN: 3528083379.
- [68] R. Aaron and R. D. Amado. “Theory of the Reaction $n + d \rightarrow n + n + p$ ”. In: *Physical Review* 150.3 (Oct. 1966), pp. 857–866. ISSN: 0031-899X. DOI: [10.1103/physrev.150.857](https://doi.org/10.1103/physrev.150.857).
- [69] R. T. Cahill and I. H. Sloan. “Theory of neutron-deuteron break-up at 14.4 MeV”. In: *Nuclear Physics A* 165.1 (Apr. 1971), pp. 161–179. ISSN: 0375-9474. DOI: [10.1016/0375-9474\(71\)90156-4](https://doi.org/10.1016/0375-9474(71)90156-4).

- [70] F. Sohre and H. Ziegelmann. “Numerical solution of the Faddeev-amado-integral equation without deformation of contours”. In: *Physics Letters B* 34.7 (Apr. 1971), pp. 579–580. ISSN: 0370-2693. DOI: [10.1016/0370-2693\(71\)90141-9](https://doi.org/10.1016/0370-2693(71)90141-9).
- [71] L. Carroll and C. Riddell. *Chris Riddell's Alice's Adventures in Wonderland*. Pan Macmillan, 2020. 320 pp. ISBN: 9781529002461.
- [72] M. Mai and M. Döring. “Three-body unitarity in the finite volume”. In: *The European Physical Journal A* 53.12 (Dec. 2017). ISSN: 1434-601X. DOI: [10.1140/epja/i2017-12440-1](https://doi.org/10.1140/epja/i2017-12440-1).
- [73] M. Aghasyan et al. “Light isovector resonances in $\pi^- p \rightarrow \pi^-\pi^-\pi^+ p$ at 190 GeV/c”. In: *Physical Review D* 98.9 (Nov. 2018), p. 092003. ISSN: 2470-0029. DOI: [10.1103/physrevd.98.092003](https://doi.org/10.1103/physrevd.98.092003).
- [74] W. H. Press, S. A. Teukolsky, W. T. Vetterling, and B. P. Flannery. *Numerical recipes. The art of scientific computing*. Ed. by W. H. Press. 3rd ed. Cambridge [u.a.]: Cambridge University Press, 2007. 1235 pp. ISBN: 0521880688.
- [75] L. Okun and A. Rudik. “On a method of finding singularities of Feynman graphs”. In: *Nuclear Physics* 15 (Feb. 1960), pp. 261–288. ISSN: 0029-5582. DOI: [10.1016/0029-5582\(60\)90307-2](https://doi.org/10.1016/0029-5582(60)90307-2).
- [76] P. Landshoff. “A discussion of dual diagrams in perturbation theory”. In: *Nuclear Physics* 20 (Oct. 1960), pp. 129–135. ISSN: 0029-5582. DOI: [10.1016/0029-5582\(60\)90163-2](https://doi.org/10.1016/0029-5582(60)90163-2).
- [77] R. P. Feynman. “Space-Time Approach to Quantum Electrodynamics”. In: *Physical Review* 76.6 (Sept. 1949), pp. 769–789. ISSN: 0031-899X. DOI: [10.1103/physrev.76.769](https://doi.org/10.1103/physrev.76.769).
- [78] U.-R. Kim, S. Cho, and J. Lee. “The art of Schwinger and Feynman parametrizations”. In: *Journal of the Korean Physical Society* 82.11 (Mar. 2023), pp. 1023–1039. ISSN: 1976-8524. DOI: [10.1007/s40042-023-00764-3](https://doi.org/10.1007/s40042-023-00764-3).
- [79] S. U. Chung. *Spin formalisms*. 1971. DOI: [10.5170/CERN-1971-008](https://doi.org/10.5170/CERN-1971-008).
- [80] J. D. Richman. “An Experimenter’s Guide to the Helicity Formalism”. In: (June 1984).
- [81] E. Leader. *Spin in Particle Physics*. Cambridge University Press, July 2001. ISBN: 9780511524455. DOI: [10.1017/cbo9780511524455](https://doi.org/10.1017/cbo9780511524455).
- [82] C. F. Gauss. *Methodus nova integralium valores per approximationem inventandi*. Gottingae, H. Dieterich, 1815, p. 71.
- [83] C. G. J. Jacobi. “Ueber Gauß neue Methode, die Werthe der Integrale näherungsweise zu finden.” In: *Journal für Reine und Angewandte Mathematik* (Jan. 1, 1826). DOI: [10.1515/crll.1826.1.301](https://doi.org/10.1515/crll.1826.1.301). URL: <https://doi.org/10.1515/crll.1826.1.301>.
- [84] P. E. Saylor and D. C. Smolarski. “Why Gaussian quadrature in the complex plane?” In: *Numerical Algorithms* 26.3 (2001), pp. 251–280. ISSN: 1017-1398. DOI: [10.1023/a:1016612909180](https://doi.org/10.1023/a:1016612909180).

Appendix A

Cutkosky Rules

In chapter 2, the Landau equations were reviewed. It was mentioned that the Landau equations tell us only the location of the kinematical singularity, and the discontinuity in the integral is given by Cutkosky rules [24]. Cutkosky rules state that for a given internal propagator that goes on-shell, the corresponding discontinuity in the integral is given by replacing the propagator with $-2\pi i \delta^{(+)}(q_i^2 - m_i^2)$, where $\delta^{(+)}$ is the δ -function multiplied with a Heaviside- Θ . That is, $\delta^{(+)}(q_i^2 - m_i^2) = \delta(q_i^2 - m_i^2)\Theta(q_i^0)$, where the superscript 0, denotes the zeroth component of the 4-momentum. More formally, for a Feynman integral I , with N internal propagators and l loop momenta,

$$\text{disc}(I) = (-2\pi i)^r \int \prod_{i'=1}^l \left(\frac{d^4 k_{i'}}{(2\pi)^4} \right) \frac{\prod_{i=1}^r \delta^{(+)}(q_i^2 - m_i^2)}{\prod_{j=1}^{N-r} (q_{r+j}^2 - m_{r+j}^2)}, \quad (\text{A.1})$$

where ‘‘disc’’ stands for discontinuity, and r labels the ‘‘cut’’ propagators that go on-shell.

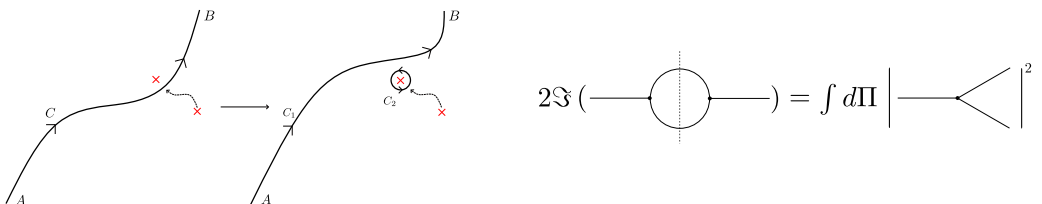


Figure A.1: The first graph shows how one can motivate the Cutkosky rules, by replacing the integration contour with two equivalent integration contours. A and B denote the endpoints of the integration contours C , C_1 and C_2 . The red points denote the poles. The second graph is the diagrammatic representation of the Cutkosky rules, in the context of the generalised optical theorem. The left-hand side is the discontinuity in the particular Feynman integral, and the right-hand side is the integral over the relative phase space over the cut propagators.

We can motivate this result by considering the situation in the first graph of figure A.1. Consider the integral,

$$I(z) = \int d^4 k \frac{F(k^2, z)}{k^2 - m^2}. \quad (\text{A.2})$$

Suppose, a pole of F moves toward the integration contour, resulting in a pinch with the singularity at m . This situation is equivalent to replacing the contour,

with a contour that does not have a pinch, and a circular contour that has a pinch. Using Cauchy's theorem, one can show that the result of the integral, is same as the one obtained by replacing the propagator with the mentioned δ -function. Though this looks very simple, Cutkosky rules are very general, and hence, very useful. In general, for a given Feynman diagram, the discontinuities in the corresponding integral can be obtained by: (1) Considering all possible cuts in a given Feynman diagram; (2) Carrying out the replacement $1/(q^2 - m^2) \rightarrow -2\pi i \delta^{(+)}(q^2 - m^2)$ for every cut configuration in consideration. The overall discontinuity is, then, the sum of discontinuities obtained from every cut configuration. This is inherently related to the optical theorem, as shown in figure [A.1](#).

Appendix B

The Landau Equations: Dual Diagram Solutions

Instead of tackling the problem of finding the solutions to the Landau equation algebraically, one may approach the problem geometrically. This approach was called the method of dual diagrams, and was studied by Taylor [38]. This was also extensively studied by Okun & Rudik [75] and Landshoff [76]. Consider the case of the triangle graph, as given in figure 2.7. The corresponding Landau equations are (see equations (2.34) & (2.35))

$$\begin{aligned} q_1^2 &= m_1^2, \\ q_2^2 &= m_2^2, \\ q_3^2 &= m_3^2. \end{aligned} \tag{B.1}$$

And

$$\alpha_1 q_1^\mu(k) + \alpha_2 q_2^\mu(k) + \alpha_3 q_3^\mu(k) = 0. \tag{B.2}$$

The second equation, geometrically, says that the 4-momentum vectors q are coplanar, and the first equation fixes the length of these 4-momentum vectors. This, taken together with the overall 4-momentum conservation, $p_1 + p_2 + p_3 = 0$, and the 4-momentum conservation at every vertex, ensures that all the 4-momentum vectors are coplanar. This situation is given in figure B.1. Similar to our discussion

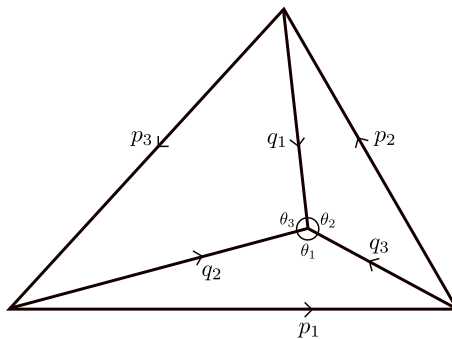


Figure B.1: The dual diagram corresponding to the triangle graph given in figure 2.7. The Landau equations, together with 4-momentum conservation, ensure that all the involved 4-momenta are coplanar.

in chapter 2, the leading singularity condition can be entirely written in terms of the external invariant masses. Geometrically, these are just the length of the sides

of the triangle. And these sides are constrained by the lengths of the 4-momentum vectors q . Therefore, one may write the constraint on the lengths of the sides of the triangle as

$$\theta_1 + \theta_2 + \theta_3 = 2\pi, \quad (\text{B.3})$$

where using the law of cosines, one may write:

$$\begin{aligned} \cos \theta_1 &= \frac{m_2^2 + m_3^2 - p_1^2}{2m_2 m_3}, \\ \cos \theta_2 &= \frac{m_1^2 + m_3^2 - p_2^2}{2m_1 m_3}, \\ \cos \theta_3 &= \frac{m_1^2 + m_2^2 - p_3^2}{2m_1 m_2}. \end{aligned} \quad (\text{B.4})$$

By taking the cosine of equation (B.3), we can see that these are exactly the determinant equations (2.36) & (2.38) from chapter 2. Further, when considering the subleading singularities — in this case, the two-body thresholds — we relax the constraint on one of the 4-momentum vectors q . That is, suppose we are contracting q_1 , then the Landau equations, geometrically, say that q_2 and q_3 must be collinear. Proceeding in a similar fashion, one can show that the kinematical singularities correspond to $p_1 = |m_2 \pm m_3|$, as expected. In terms of the dual diagram, this can be seen as the case when one of the angles, say θ_1 , must be equal to π . One still has the question of how to understand the kinematical singularities that lie on the physical sheet, for the triangle graph, in terms of the dual diagram. We recall from our discussion in chapter 2 that, suppose we fix one of the external invariant masses — in this case, the length of one of the sides of the triangle, then the region corresponding to the singularities on the physical plane, is bounded by the two-body thresholds in the other external invariant masses. In terms of the dual diagram, this translates to the condition $\theta_i \leq \pi$. That is, the point where the three 4-momentum vectors q meet, must lie inside the triangle. A rigorous treatment of dual diagrams can be found in the references mentioned before.

Appendix C

Generalised Feynman Parametrisation

Feynman parametrisation is an extremely useful mathematical trick to solve loop integrals, that arise invariably in quantum field theoretic calculations. This was originally introduced by Feynman [77]. It is discussed as a part of any standard text on quantum field theory, like Peskin & Schroeder [13] or Das [14]. The most general form of the Feynman parametrisation was also discussed by Kim [78] recently. At the most basic level, Feynman parametrisation reduces an inverse of the product of two terms, to an inverse of the sum of two terms, which are integrated over some parameters. That is,

$$\frac{1}{A_1 A_2} = \int_0^1 dx_1 \frac{1}{[x_1 A_1 + (1 - x_1) A_2]^2} = \int_0^1 dx_1 \int_0^1 dx_2 \frac{\delta(1 - x_1 - x_2)}{[x_1 A_1 + x_2 A_2]^2}. \quad (\text{C.1})$$

This lets one carry out the integral over the momentum, and express the loop integral entirely in terms of finite integrals over Feynman parameters. For example,

$$\int dp \frac{1}{A_1(p) A_2(p)} = \int_0^1 dx_1 \int dp \frac{1}{[x_1 A_1(p) + (1 - x_1) A_2(p)]^2} = \int_0^1 dx_1 C(x_1), \quad (\text{C.2})$$

where the integral over the momentum can be carried out by substitution. It is generally the case that such a momentum substitution has a Jacobian determinant of 1. Therefore, the integral measure does not gain any overall factor. In effect, one might consider the parameters to be frozen, and freely carry out any meaningful substitutions involving the loop integral momenta. This was made use of, when the two-loop integral corresponding to the triangle+1 graph was calculated in chapter 3. In the most general form, the Feynman parameter integral is given by

$$\begin{aligned} \frac{1}{A_1^{\alpha_1} \dots A_n^{\alpha_n}} &= \frac{\Gamma(\alpha_1 + \dots + \alpha_n)}{\Gamma(\alpha_1) \dots \Gamma(\alpha_n)} \int_0^1 dx_1 \dots \int_0^1 dx_n \\ &\times \frac{\delta(1 - x_1 - \dots - x_n) x_1^{\alpha_1-1} \dots x_n^{\alpha_n-1}}{[x_1 A_1 + \dots + x_n A_n]^{\alpha_1 + \dots + \alpha_n}}. \end{aligned} \quad (\text{C.3})$$

This can be proved by induction. One may also carry out the integral over the δ -function, which leads to

$$\frac{1}{A_1^{\alpha_1} \dots A_n^{\alpha_n}} = \frac{\Gamma(\alpha_1 + \dots + \alpha_n)}{\Gamma(\alpha_1) \dots \Gamma(\alpha_n)} \int_0^1 dx_2 \int_0^{1-x_2} dx_3 \dots \int_0^{1-x_2-\dots-x_{n-1}} dx_n \times \frac{(1 - x_2 - \dots - x_{n-1})^{\alpha_1-1} x_2^{\alpha_2-1} \dots x_n^{\alpha_n-1}}{[(1 - x_2 - \dots - x_{n-1})A_1 + \dots + x_n A_n]^{\alpha_1+\dots+\alpha_n}}. \quad (\text{C.4})$$

Note that we have, however, spoilt the homogeneity of the integral. To see this, notice that the integral over x_1 does not vanish, only when $0 \leq x_1 \leq 1$. This is equivalent having the integral equation contain two Heaviside- θ functions, $\theta(x_2 + \dots + x_n)$ and $\theta(1 - x_2 - \dots - x_n)$, once the integral over x_1 is carried out. The first θ -function just states that all the parameters must be positive, and this is trivially satisfied by the old limits. But the second θ -function states that the sum of the remaining parameters must always be less than or equal to 1. This amounts to saying that the reduced multi-dimensional integral is carried out in a convex region, unlike the original multi-dimensional integral, which was carried out in a homogenous cubical region. Therefore, we must replace the upper limits of the remaining integration measures, in the way given in the equation above. We may express the above multi-dimensional integral over the same limits, if we consider the following change of variables:

$$\begin{aligned} x'_2 &= x_2 \\ x'_3 &= x_3/(1 - x_2) \\ &\vdots \\ x'_n &= x_n/(1 - x_2 - \dots - x_{n-1}). \end{aligned} \quad (\text{C.5})$$

The Jacobian of this transformation is a triangular matrix, and the determinant is just the product of the diagonal elements, given by

$$|J| = \frac{\partial x_2}{\partial x'_2} \frac{\partial x_3}{\partial x'_3} \dots \frac{\partial x_n}{\partial x'_n} = (1 - x'_2)^{n-2} (1 - x'_3)^{n-3} \dots (1 - x'_{n-1}). \quad (\text{C.6})$$

The reduced multi-dimensional integral is then given by

$$\begin{aligned} \frac{1}{A_1^{\alpha_1} \dots A_n^{\alpha_n}} &= \frac{\Gamma(\sum_{i=1}^n \alpha_i)}{\prod_{i=1}^n \Gamma(\alpha_i)} \int_0^1 \prod_{k=2}^n dx'_k \\ &\times \frac{\prod_{i=2}^n \left((x'_i)^{\alpha_i-1} (1 - x'_i)^{\alpha_1-1 + \sum_{j>i} \alpha_j} \right)}{\left[\prod_{i=2}^n (1 - x'_i) A_1 + \sum_{i=2}^n \left(x'_i A_i \prod_{j=2}^{i-1} (1 - x'_j) \right) \right]^{\sum_{i=1}^n \alpha_i}}. \end{aligned} \quad (\text{C.7})$$

This was, again, the form of the multi-dimensional integral used in the evaluations of the triangle+1 graph in chapter 3.

Appendix D

Partial Wave Analysis

The Bethe-Salpeter ansatz was reduced to a 3-dimensional integral, given by the equations (4.21) and (4.22). These integrals are still too complicated to solve directly. A general solution strategy is to decompose this integral in terms of partial waves. For low enough energies, the higher order partial waves can be ignored, and this decomposition is finite. We still have the freedom to choose the basis, and there are two standard choices — the *JLS* basis and the helicity basis. The *JLS* basis is useful when considering the total angular momentum (\mathbf{J}) of the system of particles, which is arrived at by considering different possible combinations of the relative angular momentum (\mathbf{L}) between the particles and total spin (\mathbf{S}) of the constituent particles of the system. The coefficients corresponding to the basis vectors are determined by Clebsch-Gordan coefficients. This is the standard choice in non-relativistic quantum mechanics. Whereas the helicity basis is useful when not considering the total spin and relative angular momentum separately. The coefficients corresponding to the basis vectors in this case are determined by Wigner-D and Wigner-d functions. The usually preferred basis for such an angular decomposition is the helicity basis, known more commonly as the helicity formalism. The problem with the *JLS* basis is that the frames of references in which L and S are defined, are different. S is defined in the rest frame of the constituent particles, whereas L is defined in the centre of mass frame of the system of particles. Further, helicity is a good quantum number in relativistic quantum mechanics. Hence, the amplitude is decomposed into partial waves in the helicity basis first. But, we are usually interested in a particular relative angular momentum between the isobar and the spectator. Therefore, the decomposed amplitude is then transformed to the *JLS* basis, in which the interested partial waves can be projected out. The following discussion is mostly derived from the works of Jacob & Wick [56], Chung [79] and Richman [80]. A more modern approach can be found in Leader [81].

The Helicity Basis

Helicity is defined as the projection of the spin of a particle on to the direction of the momentum of a particle. That is,

$$\lambda = \mathbf{S} \cdot \hat{\mathbf{p}}. \quad (\text{D.1})$$

The angular momentum of the particle does not contribute to helicity, since by definition, it is perpendicular to the momentum vector. Defining the Euler angles,

α , β and γ , it can be shown that an arbitrary rotation can be expressed as

$$R(\alpha\beta\gamma) = e^{-i\alpha J_z} e^{-i\beta J_y} e^{-i\gamma J_z}, \quad (\text{D.2})$$

where J_i 's are the generators of rotation about the i -th axis. Since $[R, J^2] = 0$, the (total) spin eigenstates transform irreducibly under rotation. That is,

$$R(\alpha\beta\gamma)|jm\rangle = \sum_{m'=-j}^j D_{m'm}^j(\alpha\beta\gamma)|jm'\rangle, \quad (\text{D.3})$$

where, $D_{m'm}^j(\alpha\beta\gamma)$ is the (big) Wigner-D function. Using the orthogonality of the eigenstates, one can show that

$$D_{m'm}^j(\alpha\beta\gamma) = \langle jm'|R(\alpha\beta\gamma)|jm\rangle. \quad (\text{D.4})$$

And, making use of the definition of the rotation, one can show that

$$D_{m'm}^j(\alpha\beta\gamma) = e^{-i\alpha m'} \langle jm'|e^{-i\beta J_y}|jm\rangle e^{-i\gamma m} = e^{-i\alpha m'} d_{m'm}^j(\beta) e^{-i\gamma m}, \quad (\text{D.5})$$

where, $d_{m'm}^j(\beta)$ is the (small) Wigner-d function. The (small) Wigner-d has various constraints, which leads to nice properties. Also, the (big) Wigner-D obeys the following orthogonality relation:

$$\int_0^{2\pi} d\alpha \int_{-1}^1 d(\cos(\beta)) D_{m_1 m_2}^j(\alpha, \beta, -\alpha) D_{m'_1 m'_2}^{j'}(\alpha, \beta, -\alpha) = \frac{4\pi}{2j+1} \delta_{j'j} \delta_{m'_1 m_1} \delta_{m'_2 m_2}. \quad (\text{D.6})$$

The above orthogonality relation is used for inversion between bases. Now, a two-particle system with a fixed total energy in the plane-wave helicity basis, can be written in the spherical-wave helicity basis as

$$|\mathbf{p}|, \theta, \phi; \lambda_1, \lambda_2\rangle = \sum_{j,m} \sqrt{\frac{2j+1}{4\pi}} D_{m\lambda}^j(\phi, \theta, -\phi) |\mathbf{p}|, j, m; \lambda_1, \lambda_2\rangle, \quad (\text{D.7})$$

where, $\lambda \equiv \lambda_1 - \lambda_2$. The choice of $\alpha = -\gamma = \phi$ is conventional, and is due to Jacob & Wick [56]. The inverse relation is given by

$$|\mathbf{p}|, j, m; \lambda_1, \lambda_2\rangle = \int d\Omega \sqrt{\frac{2j+1}{4\pi}} D_{m\lambda}^j(\phi, \theta, -\phi) |\mathbf{p}|, \theta, \phi; \lambda_1, \lambda_2\rangle. \quad (\text{D.8})$$

Now, the matrix element of an operator M is given by

$$\begin{aligned} \langle |\mathbf{q}|, \theta', \phi'; \lambda'_1, \lambda'_2 | M | |\mathbf{p}|, \theta, \phi; \lambda_1, \lambda_2 \rangle = \\ \sum_{j,m} \frac{2j+1}{4\pi} D_{m\lambda'}^j(\phi', \theta', -\phi') D_{m\lambda}^j(\phi, \theta, -\phi) \\ \times \langle |\mathbf{q}|, j, m; \lambda'_1, \lambda'_2 | M | |\mathbf{p}|, j, m; \lambda_1, \lambda_2 \rangle, \end{aligned} \quad (\text{D.9})$$

where, we have made use of conservation of angular momentum. Similarly, the inverse relation is given by

$$\begin{aligned} \langle |\mathbf{q}|, j, m; \lambda'_1, \lambda'_2 | M | |\mathbf{p}|, j, m; \lambda_1, \lambda_2 \rangle = \\ \frac{2j+1}{4\pi} \int d\Omega' \int d\Omega D_{m\lambda'}^j(\phi', \theta', -\phi') D_{m\lambda}^j(\phi, \theta, -\phi) \\ \times \langle |\mathbf{q}|, \theta', \phi'; \lambda'_1, \lambda'_2 | M | |\mathbf{p}|, \theta, \phi; \lambda_1, \lambda_2 \rangle. \end{aligned} \quad (\text{D.10})$$

These relations can now be applied to equation (4.43).

The JLS Basis

Once the quantities in the plane-wave helicity basis are written in the spherical-wave helicity basis, the next step is to write them in spherical-wave spin-orbit basis. This form lets one project out the partial wave with the specific relative angular momentum one is interested in. Using completeness relation, the spherical-wave helicity states can be written as

$$|j, m; \lambda_1, \lambda_2\rangle = \sum_{L,S} |j, m; L, S\rangle \langle j, m; L, S| j, m; \lambda_1, \lambda_2\rangle, \quad (\text{D.11})$$

where the inner product is given by

$$\langle j, m; L, S| j, m; \lambda_1, \lambda_2\rangle = \sqrt{\frac{2L+1}{2j+1}} \langle L, 0; S, \lambda| j, \lambda\rangle \langle S_1, \lambda_1; S_2, -\lambda_2| S, \lambda\rangle \equiv U_{L\lambda}. \quad (\text{D.12})$$

Here, $\langle j_1, m_1; j_2, m_2| jm\rangle$ is the Clebsch-Gordan coefficient. Combining this with the result from the previous section, one gets

$$\langle j, m; L', S'| M| j, m; L, S\rangle = \sum_{\lambda', \lambda} U_{L'\lambda'} \langle j, m; \lambda'_1, \lambda'_2| M| j, m; \lambda_1, \lambda_2\rangle U_{\lambda L}, \quad (\text{D.13})$$

where, $U_{\lambda L}$ is the complex conjugate of the inner product defined before, and $U_{\lambda L} = U_{L\lambda}$, due to the coefficients being real. Similarly, the inverse relation reads:

$$\langle j, m; \lambda'_1, \lambda'_2| M| j, m; \lambda_1, \lambda_2\rangle = \sum_{L', L} U_{\lambda' L'} \langle j, m; L', S'| M| j, m; L, S\rangle U_{L\lambda}. \quad (\text{D.14})$$

In the context of the isobar-spectator model, one first writes down equation (4.43) as helicity projected states. Then, the plane-wave helicity states are transformed to spherical-wave helicity states. This reduces the three-dimensional integral to a one-dimensional integral and a sum over total angular momentum, j . Next, the spherical-wave helicity states are written in the spin-orbit basis, with the help of the linear transformation, $U_{L\lambda}$. Now, the amplitudes corresponding to the relevant partial waves can be calculated. This is followed by using the inverse relations to write the result in helicity basis, which is finally summed over all possible helicities. In our work, the constituent particles are scalars. We considered a scalar source, as well, resulting in no relative angular momentum. Therefore, we are only interested in the $JLS = 000$ state. This reduces the tediousness of this task, since most of the coefficients are now unity. When one extends the analysis carried out in this work to the real system, one needs to carefully consider the allowed states, and go through this procedure. Also, the couplings considered in this work were scalars. In the most general case, one needs to consider possibly derivative couplings, see for example, Sadasivan et al. [51, 52].

Appendix E

Unitarity of the Isobar

Here, we derive the discontinuity of the isobar propagator used in chapter 4. We know that unitarity demands, $SS^\dagger = S^\dagger S = \mathbb{1}$, which implies

$$T - T^\dagger = iT^\dagger T, \quad (\text{E.1})$$

through the definition, $S = \mathbb{1} + iT$. For two-body scattering with incoming 4-momenta p_1, p_2 and outgoing 4-momenta q_1, q_2 , we can write the above equation as

$$\begin{aligned} \langle q_1, q_2 | T - T^\dagger | p_1, p_2 \rangle &= i \int \frac{d^4 k_1}{(2\pi)^4} \int \frac{d^4 k_2}{(2\pi)^4} (2\pi) \delta^{(+)}(k_1^2 - m_1^2) (2\pi) \delta^{(+)}(k_2^2 - m_2^2) \\ &\quad \times (2\pi)^4 \delta^{(4)}(p_1 + p_2 - k_1 - k_2) \langle q_1, q_2 | T^\dagger | k_1, k_2 \rangle \langle k_1, k_2 | T | p_1, p_2 \rangle. \end{aligned} \quad (\text{E.2})$$

Note that for spinless two-body scattering, the T -matrix element can be written as an analytic function of the momentum invariants. That is,

$$\langle q_1, q_2 | T | p_1, p_2 \rangle = T(s, t), \quad (\text{E.3})$$

where, $s = (p_1 + p_2)^2 = P^2$ and $t = (p_1 - q_1)^2$, are Mandelstam variables. $\delta^{(+)}$ denotes the δ -function multiplied with a Heaviside- θ . And for an isobar, T is entirely a function of s , that is, $T(s, t) \equiv T(s)$. In the centre of mass frame of reference, \sqrt{s} is just the incoming energy of the isobar. One may carry out the integral over k_2 , leading to

$$\begin{aligned} T(s) - T^\dagger(s) &= iT^\dagger(s) T(s) (2\pi)^2 \int \frac{d^4 k_1}{(2\pi)^4} \theta(k_1^0) \theta(\sqrt{s} - k_1^0) \\ &\quad \times \delta(k_1^2 - m_1^2) \delta((P - k_1)^2 - m_2^2). \end{aligned} \quad (\text{E.4})$$

Now, the first δ -function can be reduced to

$$\delta(k_1^2 - m_1^2) = \frac{1}{2\sqrt{|\mathbf{k}_1|^2 + m_1^2}} \left[\delta \left(k_1^0 - \sqrt{|\mathbf{k}_1|^2 + m_1^2} \right) + \delta \left(k_1^0 + \sqrt{|\mathbf{k}_1|^2 + m_1^2} \right) \right]. \quad (\text{E.5})$$

The integral measure can be written in spherical co-ordinates, and the integral over the zeroth-component, k_1^0 , can be carried out. The contribution from the second

δ -function in the above equation vanished due to the Heaviside- θ . We therefore get

$$T(s) - T^\dagger(s) = i \frac{T^\dagger(s)T(s)}{4\pi^2} \int d\Omega \int \frac{\mathbf{k}_1^2 d|\mathbf{k}_1|}{2\sqrt{|\mathbf{k}_1|^2 + m_1^2}} \\ \times \theta \left(\sqrt{s} - \sqrt{|\mathbf{k}_1|^2 + m_1^2} \right) \delta \left(\left(\sqrt{s} - \sqrt{|\mathbf{k}_1|^2 + m_1^2} \right)^2 - |\mathbf{k}_1|^2 - m_2^2 \right). \quad (\text{E.6})$$

Now, the δ -function in the above equation can be reduced to

$$\delta \left(\left(\sqrt{s} - \sqrt{|\mathbf{k}_1|^2 + m_1^2} \right)^2 - |\mathbf{k}_1|^2 - m_2^2 \right) = \\ \frac{\sqrt{\frac{\lambda(s, m_1^2, m_2^2)}{4s} + m_1^2}}{\lambda^{(1/2)}(s, m_1^2, m_2^2)} \delta \left(|\mathbf{k}_1| - \frac{\lambda^{1/2}(s, m_1^2, m_2^2)}{2\sqrt{s}} \right). \quad (\text{E.7})$$

Here, λ is the Källén triangle function. We can now carry out the integral over $|\mathbf{k}_1|$. One may, also, readily verify that the zero of the δ -function corresponds to a positive Heaviside- θ argument. With this, we get

$$T(s) - T^\dagger(s) = i \frac{|T|^2}{8\pi s} \lambda^{1/2}(s, m_1^2, m_2^2). \quad (\text{E.8})$$

or equivalently,

$$\Im(T^{-1}) = \frac{-\lambda^{1/2}(s, m_1^2, m_2^2)}{16\pi s}. \quad (\text{E.9})$$

In the case of identical internal propagators, one needs to multiply the above result with a symmetry factor of $1/2$. This is, exactly, the discontinuity in the isobar propagator discussed in chapter 4. This equation was compared with the numerical values of the inverse isobar propagator, which was, through unitarity matching, expected to be,

$$\Im(\tau^{-1}(\sigma)) = \frac{g^2}{16\pi\sigma} \lambda^{1/2}(\sigma, m_1^2, m_2^2). \quad (\text{E.10})$$

Appendix F

Gaussian Quadrature Integration Routine

The integral equations encountered in this work are either too complicated to solve analytically, or definitely require discretisation of the integral equation. The numerical method used to solve the definite integrals is Gaussian quadrature. This method was originally introduced by Gauß [82], and interestingly, he used continued fractions to develop this method. However, the widely used formulation of this method using orthogonal polynomials was introduced by Jacobi [83]. One may refer to standard textbooks on numerical methods, and also Press et al. [74]. Specifically for complex Gaussian quadrature, one may refer to Saylor & Smolarski [84]. The basic principle of Gaussian quadrature is to approximate the definite integral with a finite sum of the function evaluated at specific points, multiplied by appropriate weighting coefficients. That is,

$$\int_a^b f(x) \equiv \int_a^b W(x)g(x)dx \approx \sum_{j=0}^{N-1} w_j g(x_j) = \sum_{j=0}^{N-1} v_j f(x_j), \quad (\text{F.1})$$

where, v_j is defined as $w_j/W(x_j)$. w_j are the weights corresponding to the function W , which are not explicitly evaluated. Also, the integrand is taken to be a product of a polynomial function, g , and a known function, W , which can also absorb remove integrable singularities. The advantage of this method is that one has the freedom to pick the set of points where the function is evaluated. The weights, then, can be determined appropriately. However, this method has the drawback that the integrand must be smooth enough for decent accuracy. This problem is compensated by the fact that for the integrands considered typically, which are the ones that can be approximated by polynomials multiplied by a known function, result in accurate integral evaluations. Given an integration interval, one constructs N polynomial functions, that are orthogonal with respect to the given weighting function. That is,

$$\int_a^b P_m(x)P_n(x)W(x)dx = \delta_{mn}. \quad (\text{F.2})$$

The roots of these orthogonal polynomials in the interval of integration, then correspond to the points in which the integrand is evaluated. The corresponding weights can also be determined. The particular choice of $a = -1$ and $b = 1$, taken together with $W(x) = 1$, corresponds to Legendre polynomials as the orthogonal polynomials. This is aptly called *Gauss-Legendre* quadrature. When the integrand is a

polynomial of order less than or equal to $2n - 1$, the integral approximation is exact for n quadrature points. One can also derive the corresponding quadrature points and the weights associated with the other classical orthogonal polynomials.

The standard Gauss-Legendre quadrature points and the corresponding weights are given in the interval $(-1, 1)$, and they are also not equally spaced. For an integration over a different interval, one can perform a transformation of the integration variable, to match the required integration interval. Suppose, we are interested in the integral,

$$I = \int_0^\Lambda dy f(y). \quad (\text{F.3})$$

For Gaussian quadrature points in the interval, $(-1, \lambda)$, we can consider the following transformation,

$$y(x) = c \tan\left(\frac{\pi}{4}(x + 1)\right), \quad (\text{F.4})$$

such that $y(\lambda) = \Lambda$. Here, c is some real parameter of the transformation and Λ is the integral cutoff. One first needs to determine the value of λ corresponding to the given cutoff, Λ . The standard Gaussian quadrature points and the weights are obtained for the range, $(-1, \lambda)$, which are then transformed according to the transformation above. Note that when the integral in consideration is over the interval, $[0, \infty)$, the Gaussian quadrature interval reduces to the standard interval, $(-1, 1)$, with $\lambda = 1$. The integral in consideration now reduces to,

$$I = \int_{-1}^\lambda dx \frac{\partial y}{\partial x} f(y(x)) \approx \sum_{j=0}^{N-1} w_j \tilde{f}(x_j), \quad (\text{F.5})$$

where, \tilde{f} is the modified function, which includes the Jacobian determinant of the transformation. In our work, we consider an integration over a complex contour, $f_{SMC}(t)$. In this case, there will be another Jacobian determinant that is to be included in the integral. That is,

$$I = \int_0^\Lambda dy f(y) = \int_0^\Lambda dt \frac{\partial f_{SMC}}{\partial t} f(y(t)), \quad (\text{F.6})$$

which then gives,

$$I = \int_{-1}^\lambda dx \frac{\partial t}{\partial x} \frac{\partial f_{SMC}}{\partial t} f(y(t(x))) \approx \sum_{j=0}^{N-1} w_j \tilde{\tilde{f}}(x_j), \quad (\text{F.7})$$

where, $\tilde{\tilde{f}}$ includes both the Jacobian determinants. For our purposes, the integral over SMC is carried out up to a cutoff, and the self-energy integral over SEC is carried out up to ∞ in principle, and the actual value depends on the chosen number of quadrature points, in practice.

Appendix G

A Second Alternate Numerical Implementation (Method3)

Along with the two primary numerical implementations considered in chapter 4, we also investigated a third numerical implementation, which was retrospectively named *Method3*. We recall that in *M0* and *M1*, the integration over the spectator loop momentum was carried out along a deformed contour, which did not have any singularity in its vicinity. To do this, the restriction that the outgoing spectator momentum is real, was relaxed. Then, the amplitudes for real outgoing spectator momentum was evaluated in two different ways. In *M3*, we instead relax the requirement that the total energy of three-body system, \sqrt{s} must be real. To this end, we add a small imaginary part to the incoming energy, while keeping the integration contour and the outgoing spectator momentum real. We evaluate the amplitudes for three different complex, but small, energies. The amplitudes for real energy are then evaluated in the limit of the small imaginary part tending to zero. To do this, we linearly fit the evaluated amplitudes in the small imaginary part, ε , and extrapolate to zero. That is, for an evaluated amplitude, $T(\sqrt{s}, \sqrt{\sigma}; \varepsilon)$, we perform a linear fit over ε , and extrapolate the amplitude $T(\sqrt{s}, \sqrt{\sigma}; 0)$. A couple of thing should be noted here — we should recall that the results are obtained by fixing either \sqrt{s} or $\sqrt{\sigma}$, and varying the other quantity. Therefore, we perform a linear fit in ε , for every amplitude that is obtained by varying the invariant. Further, the amplitudes are assumed to be analytic in the incoming and the outgoing invariant masses. Therefore, it is reasonable to assume the existence of a convergent power series about a given point, and for a small neighbourhood about this point, we can restrict the series to linear order. One pitfall with this line of reasoning is that, this works only for removable singularities, which might not be the case. Still, by the postulate that the physical amplitudes are the boundary points of the principal sheet of the analytic amplitude, considering the limit of ε is well-grounded.

First, figure G.1 shows how the singularities move away from the contour for complex total energy of the three-body system. In this example, we have shifted the value of \sqrt{s} by 100 MeV. However, for accurate results, one needs to consider much smaller shifts. While evaluating the amplitudes, we considered $\varepsilon/\text{MeV} = \{2, 3, 5\}$ for fixed \sqrt{s} plots, and $\varepsilon/\text{MeV} = \{4, 5, 6\}$ for fixed $\sqrt{\sigma}$ plots. The evaluated amplitudes are given in figure G.2. We can see that the evaluated amplitudes are comparable to the amplitudes obtained using *M0* and *M1*. However, there is an inherent difficulty in implementing *M3*. For accurate results, one needs to evaluate the amplitudes for

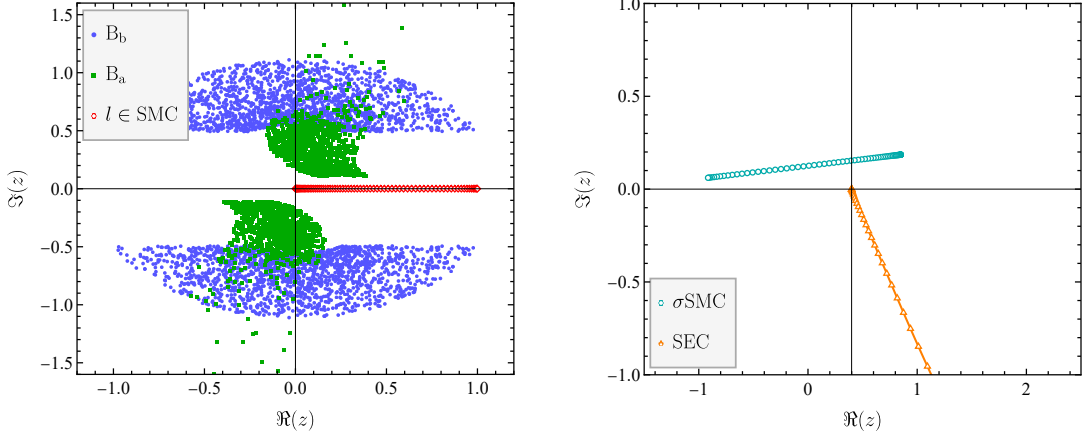


Figure G.1: The first figure shows the singularities of the B term for the spectator momentum contour, and the second figure shows the singularities of the isobar self-energy integral in $M3$. Both the plots are evaluated for $\sqrt{s} = 1.42 + 0.1$ GeV, and the shape parameters of the self-energy integral is given by $\{a, b\} = \{-1, 1.2\}$. We have included only the singularities in the $1 \rightarrow 2$ channel of the B term, and the singularities corresponding to the K^* propagator self-energy integral, since we consider only the triangle system here. The definitions of the terms in the above figures are the same as the definitions from the figures 4.12 & 4.13.

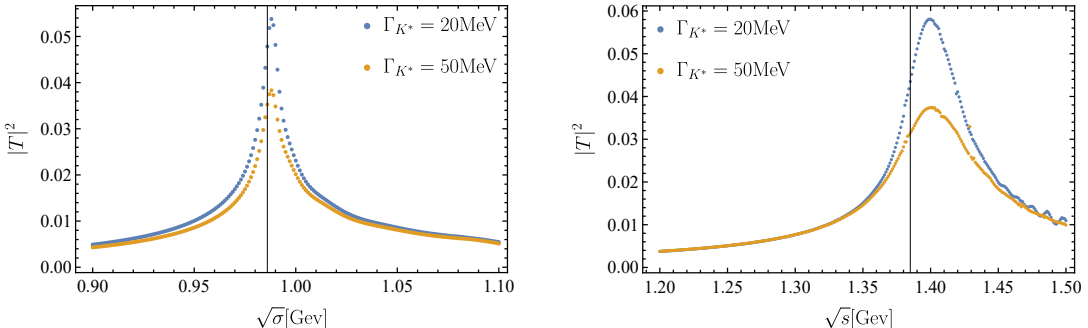


Figure G.2: The amplitudes at the triangle level obtained using $M3$. The plot on the left shows the amplitudes obtained as a function of $\sqrt{\sigma}$, for a fixed $\sqrt{s} = 1.42$ GeV, and the black line denotes the two-body $m_K + m_K$ threshold. The plot on the right shows the amplitudes obtained as a function of \sqrt{s} , for a fixed $\sqrt{\sigma} = 0.99$ GeV, and the black line denotes the two-body $m_{K^*} + m_K$ threshold. The amplitudes are obtained for two different K^* propagator widths, 20 MeV and 50 MeV.

complex \sqrt{s} , with relatively small imaginary part. But, the smaller the imaginary part is, the more oscillatory the amplitude will be, since the integration contour is very close to the singularity. Therefore, one needs to achieve a good balance between picking ε 's that are as small as possible, so that the linear fit still extrapolates to the right limit. But, not too small, so that the oscillations are avoided. This part of the implementation is trial and error. The result given here are for the triangle system. We were unable to implement this to the full unitary system, since we were not able to find ε 's small enough to evaluate the right amplitudes, for that particular case. However, this numerical implementation serves as a good sanity check to the other numerical implementations.

Appendix H

Additional Figures

The Triangle Singularity in the Second Channel

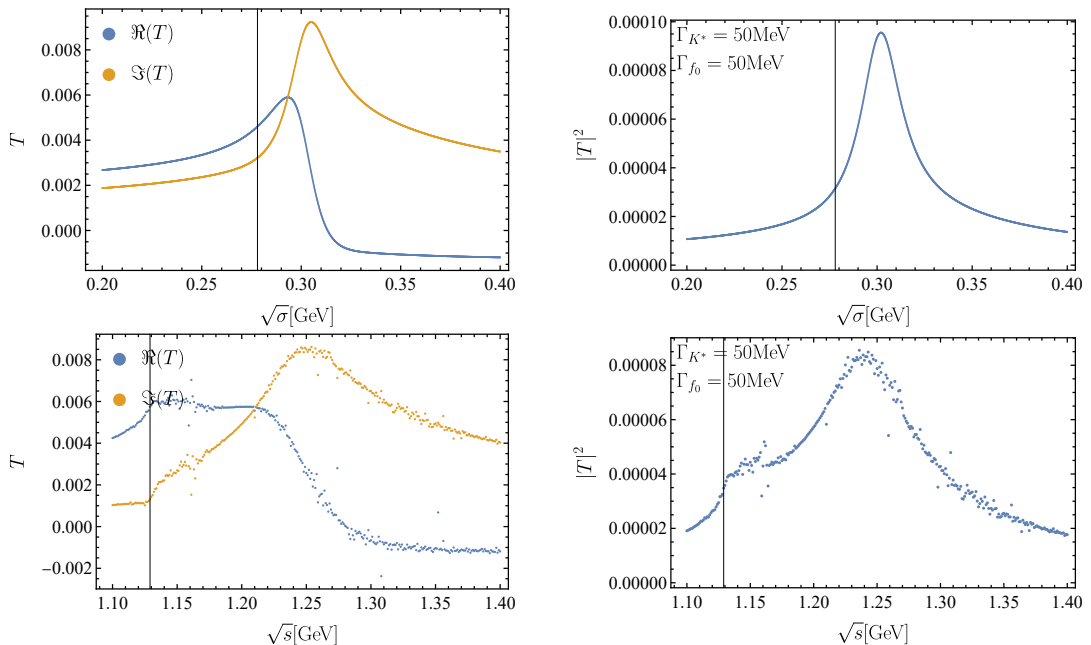
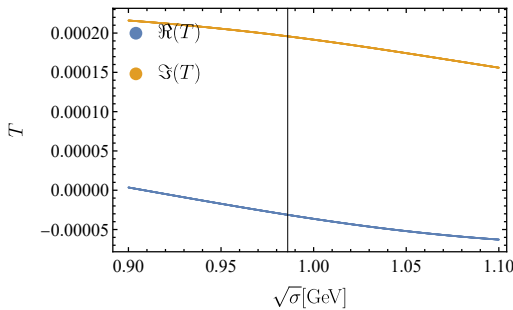
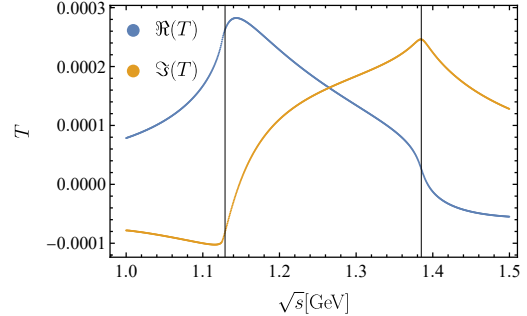


Figure H.1: The amplitudes (channel $2 \rightarrow 2$) evaluated at the triangle level. The top two images show the isobar-spectator amplitudes obtained as a function of $\sqrt{\sigma}$, for fixed $\sqrt{s} = 1.2 \text{ GeV}$. The bottom two images show the amplitudes obtained as a function of \sqrt{s} , for fixed $\sqrt{\sigma} = 0.29 \text{ GeV}$. The first plot of each row shows the real and imaginary parts of the amplitudes, and the second plot shows the absolute squared value of the amplitudes. The black line denotes the two-body threshold — $m_\pi + m_\pi$ for the plots on the top, and $m_{f_0} + m_\pi$ for the plots on the bottom, which is outside the plotted region. The K^* propagator width is set at 5 MeV and the f_0 propagator width is set at 20 MeV. The irregularities are discussed in the main content. Briefly, within this method (M0), one way to overcome the irregularities is to find the right parameters for the integration contour, which doesn't have any singularities in its vicinity. However, we do not modify the chosen contour to accommodate this transition, since the kinematical singularity region is far from the energy range we are interested in.

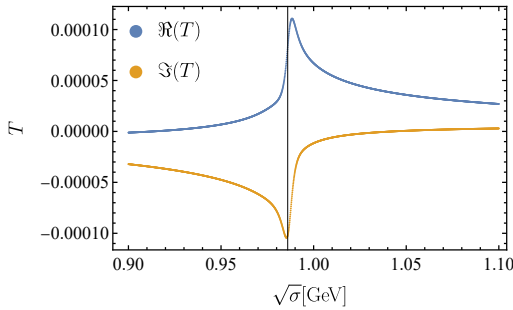
The Isobar-Spectator Model at the Finite House Level



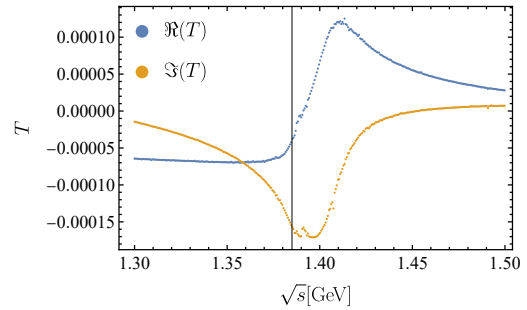
The House: T - $\sqrt{\sigma}$ plot.



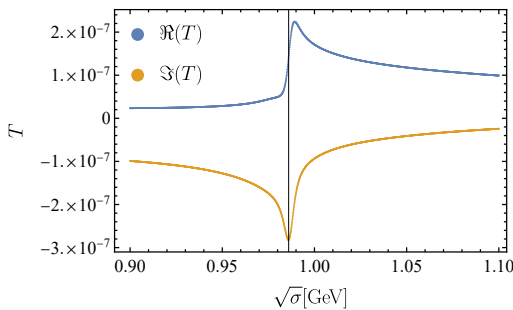
The House: T - \sqrt{s} plot.



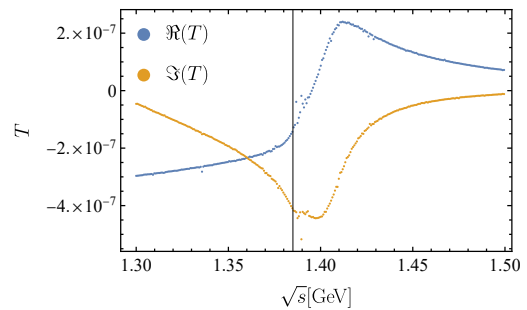
The 2-Storied House: T - $\sqrt{\sigma}$ plot.



The 2-Storied House: T - \sqrt{s} plot.



The 3-Storied House: T - $\sqrt{\sigma}$ plot.



The 3-Storied House: T - \sqrt{s} plot.

Figure H.2: The real-imaginary parts of the amplitudes from figure 4.16. The plots on the left are evaluated at fixed $\sqrt{s} = 1.42$ GeV, and the plots on the right are evaluated at fixed $\sqrt{\sigma} = 0.99$ GeV. The black line denotes the two-body threshold — $m_K + m_K$ for the plots on the left, and $m_{K^*} + m_K$ for the plot on the right. Additionally, the first plot on the right also shows the $m_{f_0} + m_\pi$ two-body threshold. The K^* propagator width is set at 20 Mev, and the f_0 propagator width is set at 50 MeV.

The Isobar-Spectator Model with Method1

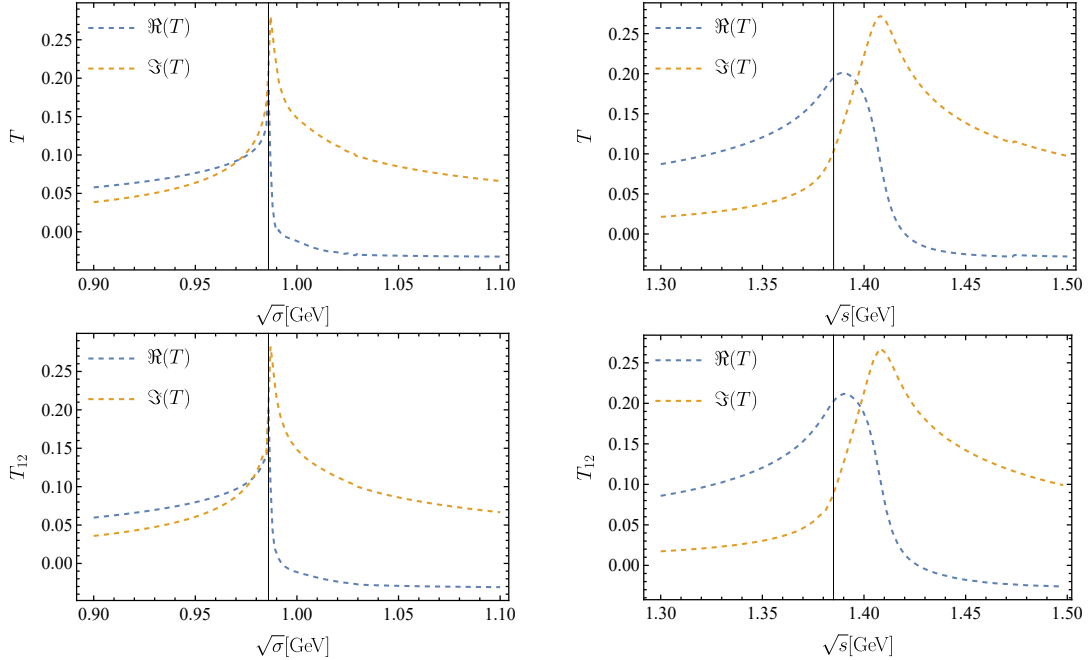


Figure H.3: The real-imaginary parts of the amplitudes from figure 4.24. The plots on the left are evaluated at fixed $\sqrt{s} = 1.42$ GeV, and the black line denotes the two-body, $m_K + m_K$ threshold. The plots on the right are evaluated at fixed $\sqrt{\sigma} = 0.99$ GeV, and the black line denotes the two-body, $m_{K^*} + m_K$ threshold. The width of the K^* propagator is taken as 20 MeV, and the width of the f_0 propagator is taken as 50 MeV.